



AUTARQUIA ASSOCIADA À UNIVERSIDADE DE SÃO PAULO

Evaluation of mechanical stability of nuclear fuel plates under axial flow conditions

JAVIER GONZÁLEZ MANTECÓN

**Tese apresentada como parte dos
requisitos para obtenção do Grau de
Doutor em Ciências na Área
de Tecnologia Nuclear - Reatores**

**Orientador:
Prof. Dr. Miguel Mattar Neto**

**São Paulo
2019**

At the bottom of the page, there are three thick, horizontal purple bars that span the width of the page, mirroring the design at the top.

INSTITUTO DE PESQUISAS ENERGÉTICAS E NUCLEARES
Autarquia associada à Universidade de São Paulo

Evaluation of mechanical stability of nuclear fuel plates under axial flow conditions

JAVIER GONZÁLEZ MANTECÓN

**Tese apresentada como parte dos
requisitos para obtenção do Grau de
Doutor em Ciências na Área
de Tecnologia Nuclear - Reatores**

**Orientador:
Prof. Dr. Miguel Mattar Neto**

Versão Corrigida
Versão Original disponível no IPEN

São Paulo
2019

Fonte de Financiamento: CAPES

Autorizo a reprodução e divulgação total ou parcial deste trabalho,
Para fins de estudo e pesquisa, desde que citada a fonte.

Como citar:

GONZÁLEZ MANTECÓN, J. ***Evaluation of mechanical stability of nuclear fuel plates under axial flow conditions***. 2019. 97 p. Tese (Doutorado em Tecnologia Nuclear), Instituto de Pesquisas Energéticas e Nucleares, IPEN-CNEN/SP, São Paulo. Disponível em: <www.teses.usp.br> (data de consulta no formato: dd/mm/aaaa)

Ficha catalográfica elaborada pelo Sistema de geração automática da Biblioteca IPEN/USP,
com os dados fornecidos pelo(a) autor(o)

González Mantecón, Javier

Evaluation of mechanical stability of nuclear fuel plates
under axial flow conditions / Javier González Mantecón;
orientador Miguel Mattar Neto. -- São Paulo, 2019.
97 p.

Tese (Doutorado) - Programa de Pós-Graduação em Tecnologia
Nuclear (Reatores) -- Instituto de Pesquisas Energéticas e
Nucleares, São Paulo, 2019.

1. Elemento combustível tipo placas. 2. Velocidade
crítica. 3. Interação fluido-estrutura. I. Mattar Neto,
Miguel, orient. II. Título

FOLHA DE APROVAÇÃO

Autor: Javier González Mantecón

Título: Evaluation of mechanical stability of nuclear fuel plates under axial flow conditions.

Tese apresentada ao Programa de Pós-Graduação em Tecnologia Nuclear da Universidade de São Paulo para obtenção do título de Doutor em Ciências.

Data: 26/02/2019

Banca Examinadora

Prof. Dr. Bruno Souza Carmo

Instituição: Universidade de São Paulo Julgamento: Aprovado

Prof. Dr. Renato Pavanello

Instituição: Universidade Estadual de Campinas Julgamento: Aprovado

Prof. Dr. Delvonei Alves de Andrade

Instituição: Instituto de Pesquisas Energéticas e Nucleares Julgamento: Aprovado

ACKNOWLEDGMENTS

My deepest gratitude to my dissertation supervisor Dr. Miguel Mattar Neto, for giving me the opportunity to perform doctoral studies with him and for the many hours spent discussing the work. I have been very fortunate to have a supervisor who allowed me to research on my own and gave me his unconditional help when needed.

I also want to express my appreciation to Professors Bruno Souza Carmo, Renato Pavanello, Delvonei Alves de Andrade, Jorge Luis Baliño, and Carlos A. J. Miranda, whose comments and feedback helped to improve this work.

Thanks to all my colleagues at IPEN for their friendship and aid during my stay in this institution.

My special thanks go to my wife and our families for their continual support.

Finally, this study was financed by the Coordenação de Aperfeiçoamento de Pessoal de Nível Superior – Brasil (CAPES) – Finance Code 001. This assistance is gratefully acknowledged by the author.

ABSTRACT

GONZÁLEZ MANTECÓN, J. *Evaluation of mechanical stability of nuclear fuel plates under axial flow conditions*. 2019. 97 p. Tese (Doutorado em Tecnologia Nuclear) – Instituto de Pesquisas Energéticas e Nucleares – IPEN-CNEN/SP. São Paulo.

Several nuclear research reactors use or are planned with cores containing flat-plate-type fuel elements. The nuclear fuel is contained in parallel plates that are separated by narrow channels through which the fluid flows to remove the heat generated by fission reactions. One of the problems of this fuel element design is the mechanical stability of the fuel plates. High-velocity coolant flowing through the channels can cause large deflections of these plates leading to local overheating, structural failure or plate collapse. As a consequence, the safe operation of the reactor may be affected.

In this work, a numerical fluid-structure interaction study was conducted for evaluating the mechanical stability of nuclear fuel plates under axial flow conditions. Five different cases were analyzed. In all cases, the system consisted of two fuel plates bounded by fluid channels but, in case 5, a support comb at the leading edge of the plates was inserted. The pressure loadings caused by the fluid flow were calculated using a Computational Fluid Dynamics model created with ANSYS CFX. The structural response was determined by means of a Finite Element Analysis model generated with ANSYS Mechanical. Both models were coupled using the two-way fluid-structure interaction approach.

The results from Case 1 allowed proposing a methodology to predict the critical velocity of the assembly without an inlet support comb. The maximum deflection of the plates was detected at their leading edges. It was detected that, for flow rates in the channels less than a certain value, the maximum deflection increased linearly with the square of the coolant velocity. In contrast, for greater flow rates, a nonlinear behavior was observed. Therefore, that fluid velocity was identified as the critical velocity of the

system. Besides, above the critical velocity, an extra deflection peak was observed near the trailing edge of the plates.

In cases 2, 3 and 4, the influence of manufacturing deviations and the change of materials properties due to the increment of temperature on the critical velocity was investigated. With these conditions, the critical velocity of the system was found at lower values.

Lastly, in Case 5, the effectiveness of using a support comb at the leading edge of the plates was investigated. The results showed that the static divergence at the inlet end is effectively eliminated with the installation of the comb. In addition, the flow-induced deflections along the length of the plates were significantly diminished with the comb.

Keywords: flat-plate-type fuel element; critical velocity; fluid-structure interaction; nuclear research reactors.

RESUMO

GONZÁLEZ MANTECÓN, J. *Avaliação de estabilidade mecânica de placas de combustível nuclear sob condições de fluxo axial*. 2019. 97 p. Tese (Doutorado em Tecnologia Nuclear) – Instituto de Pesquisas Energéticas e Nucleares – IPEN-CNEN/SP. São Paulo.

Muitos reatores nucleares de pesquisa usam ou são planejados com elementos combustíveis tipo placas planas. O combustível nuclear está contido em placas paralelas que são separadas por canais estreitos através dos quais o fluido refrigerante passa para remover o calor gerado pelas reações de fissão. Um dos problemas deste tipo de elemento combustível é a estabilidade mecânica das placas de combustível. O líquido refrigerante a alta velocidade pode causar deflexões excessivas dessas placas, bloqueando o canal de escoamento e levar ao superaquecimento nas placas, falha estrutural ou colapso da placa. Como consequência, a operação segura do reator pode ser afetada.

Neste trabalho, foi realizado um estudo numérico de interação fluido-estrutura para avaliar a estabilidade mecânica de placas de combustível nuclear sob condições de fluxo axial. Cinco diferentes casos foram analisados. Em todos os casos, o sistema consistiu em duas placas de combustível delimitadas por canais de fluido, mas, no caso 5, um pente de suporte na borda de ataque das placas foi inserido. As cargas de pressão causadas pela vazão foram calculadas usando um modelo de Dinâmica dos Fluidos Computacional, criado com ANSYS CFX. A resposta estrutural foi determinada por meio de um modelo de elementos finitos, gerado com ANSYS Mechanical. Os modelos foram acoplados usando a abordagem de interação fluido-estrutura bidirecional.

Os resultados do Caso 1 permitiram propor uma metodologia para prever a velocidade crítica do sistema sem o pente de suporte. A deflexão máxima das placas foi observada em suas bordas de ataque. Foi detectado que, para velocidades nos canais inferiores a um determinado valor, a deflexão máxima aumentava linearmente com o quadrado da velocidade do líquido refrigerante. Em contraste, para maiores vazões, um

comportamento não linear foi observado. Portanto, essa velocidade do fluido foi identificada como a velocidade crítica. Além disso, acima da velocidade crítica, um pico extra de deflexão foi observado próximo à borda de saída das placas.

Nos casos 2, 3 e 4, a influência dos desvios de fabricação e da alteração das propriedades dos materiais devido ao incremento de temperatura na velocidade crítica foi investigada. Sob essas condições, a velocidade crítica foi encontrada a valores mais baixos.

Por fim, no Caso 5, a eficácia do uso do pente de suporte na borda de entrada das placas foi estudada. Os resultados mostraram que a divergência estática na extremidade de entrada foi efetivamente eliminada com a instalação do pente. Além disso, as deflexões induzidas pelo fluido ao longo do comprimento das placas foram significativamente diminuídas com o pente.

Palavras-chave: elemento combustível tipo placas; velocidade crítica; interação fluido-estrutura; reatores de pesquisa.

TABLE OF CONTENTS

1. INTRODUCTION.....	12
1.1. Survey of Literature.....	13
1.1.1. Effects of Support Comb.....	22
1.2. Motivation.....	23
1.3. Goals of the Study	23
1.4. Importance of the Study	24
1.5. Document Organization	24
2. FUNDAMENTALS.....	25
2.1. Governing Equations of Fluid.....	25
2.1.1. Turbulence Models.....	27
2.1.1.1. The k- ϵ Model.....	29
2.1.1.2. The SST k- ω Model	30
2.1.2. Near-Wall Modeling.....	31
2.1.3. Boundary Conditions.....	33
2.2. Governing Equations of Solid	35
2.2.1. Overview of the Finite Element Method	35
2.3. Coupling Conditions	39
3. NUMERICAL METHODOLOGY	41
3.1. Multiphysics Analysis with ANSYS.....	43
3.2. Verification and Validation.....	44
3.2.1. Grid Convergence Index.....	45
3.2.2. Turbulence Model Study.....	46
3.2.3. Fluid Model Verification.....	52

3.2.4. Solid Model Verification	55
3.2.5. Validation Study	58
3.3. Multiphysics Models.....	60
3.3.1. Temporal Discretization	63
4. RESULTS AND DISCUSSION.....	66
4.1. Results from Case 1.....	67
4.2. Results from Case 2.....	71
4.3. Results from Case 3.....	71
4.4. Results from Case 4.....	72
4.5. Results from Case 5.....	75
4.6. Comparison with Miller’s Velocity	79
5. CONCLUSIONS AND FUTURE WORKS.....	81
5.1. Conclusions	81
5.2. Recommendation for Future Works.....	82
REFERENCES.....	84
APPENDIX A. APPARENT ORDER CALCULATION	90
APPENDIX B. PRESSURE DROP ANALYTICAL MODEL	91
APPENDIX C. SETTINGS OF THE FSI ANALYSIS.....	93
C.1. Excerpts from the CFX Output File.....	93
C.2. Excerpts from the ANSYS Mechanical Output File	95
APPENDIX D. EXAMPLES OF CONVERGENCE HISTORY.....	97

LIST OF TABLES

Table 3.1. Geometric specifications for each case.....	42
Table 3.2. Results of the pressure drop and wall shear stress.	49
Table 3.3. Results from the simplified CFD model and comparison with the analytical solutions.....	51
Table 3.4. Water properties for given temperatures.....	52
Table 3.5. Volumetric flow rates, velocities, and Reynolds numbers.....	53
Table 3.6. Characteristics of the meshes used in the verification of the fluid models and values of the key parameters.	54
Table 3.7. Uncertainty quantification of the CFD model.	55
Table 3.8. Aluminum alloy 6061-T6 properties for given temperatures.....	55
Table 3.9. Characteristics of the meshes used in the verification of the solid models and values of the key parameter.	58
Table 3.10. Uncertainty quantification of the solid model.	58
Table 3.11. Settings of the fluid-structure interaction analyses.....	62
Table 3.12. Uncertainty quantification of the temporal discretization.	65
Table 4.1. Volume flow rates and velocities used in the simulations.....	66
Table 4.2. Comparison between the critical velocity predicted with the multiphysics model and Miller’s velocity for cases 1 to 4.....	80

LIST OF FIGURES

Figure 1.1. Example of a plate-type fuel assembly.	13
Figure 1.2. Outlines of plate assembly [taken from (Miller, 1958)].....	14
Figure 1.3. Diagram of a support comb.	22
Figure 2.1. Control volume of fluid.....	26
Figure 2.2. Typical velocity distribution in the turbulent flow near a solid boundary [adapted from (White, 2011)].....	32
Figure 2.3. Example of elements employed in one, two and three dimensions [modified from (Chapra and Canale, 2015)].....	36
Figure 3.1. (a) Generic diagrams of the computational domain without and (b) with the support comb.....	41
Figure 3.2. Flowchart of a two-way FSI analysis [modified from (ANSYS Inc., 2017a)]..	44
Figure 3.3. The domain used in the selection of the turbulence model.....	47
Figure 3.4. Illustration of a sudden contraction (left) and a sudden expansion (right)....	48
Figure 3.5. Simplified domain created in ANSYS CFX.....	50
Figure 3.6. Mesh of the simplified CFD model.	50
Figure 3.7. Deviation of the numerical solution from the analytical results.	51
Figure 3.8. Examples of the mesh utilized in the verification of the fluid model: (a) model without and (b) with support comb.....	53
Figure 3.9. Example of the mesh utilized in the verification of the solid model without the support comb. The red surfaces are the regions used to fix the plates. The arrow indicates the direction of application of the pressure load.	56
Figure 3.10. Example of the mesh utilized in the verification of the solid model with the support comb. The red surfaces are the regions used to fix the plates and the comb. The arrow indicates the direction of application of the pressure load.	57

Figure 3.11. (a) Schematic representation of Kennedy’s one-plate experiment and (b) FSI model..... 59

Figure 3.12. Comparison of the numerical result with the experimental data. 60

Figure 3.13. Fluid-solid model without the inlet comb (cases 1 to 4)..... 61

Figure 3.14. Fluid-solid model with the inlet comb (Case 5). 61

Figure 3.15. Location of Points A and B to observe the evolution of deflection of the plates. 63

Figure 3.16. Convergence history of Point A displacement for a fluid velocity in the channels of 8.2 m/s and different time steps..... 64

Figure 4.1. Deflection profile of Plate 1 for different fluid velocities in the channels..... 67

Figure 4.2. Maximum deflection of Plate 1 or 2 as a function of the square of the fluid velocity in the channels in Case 1. The arrow points out the critical fluid velocity. 68

Figure 4.3. Deflection contours of the plates for different fluid velocities in the channels. Fluid flow is downward. The deflection scale factor is 0.5x..... 69

Figure 4.4. Leading edge deflection into the channel for two-different fluid velocities in the channels..... 70

Figure 4.5. Ratio of area change at the leading edge for different fluid velocities in the channels. 70

Figure 4.6. Maximum deflection of Plate 1 or 2 as a function of the square of the fluid velocity in the channels in Case 2. The arrow points out the critical fluid velocity..... 71

Figure 4.7. Deflection profile of each plate for a fluid velocity in the channels of 17.07 m/s. 72

Figure 4.8. Velocity contours along the midplane of the channels and close to the leading edge of the plates for inlet fluid velocities of (a) 6.08 m/s and (b) 12.49 m/s. Fluid flow is downward and the plates are presented undeformed. 73

Figure 4.9. Pressure contours along the midplane of the channels and close to the leading edge of the plates for inlet fluid velocities of (a) 6.08 m/s and (b) 12.49 m/s. Fluid flow is downward and the plates are presented undeformed..... 73

Figure 4.10. Maximum deflection of the plates as a function of the square of the fluid velocity in the channels in Case 3. The arrows point out the critical fluid velocity 74

Figure 4.11. Maximum deflection of Plate 1 or 2 as a function of the square of the fluid velocity in the channels in Case 4. The arrow points out the critical fluid velocity 74

Figure 4.12. Maximum deflection of Plate 1 or 2 as a function of the square of the fluid velocity in the channels: comparison between cases 1 and 4. 75

Figure 4.13. Pressure difference along the length of Plate 1 for different fluid velocities in the channels, with the support comb at the inlet end of the plates. 76

Figure 4.14. Deflection profile of Plate 1 for different fluid velocities in the channels, with the support comb at the inlet end of the plates. 76

Figure 4.15. Deflection profile of Plate 1 for different fluid velocities in the channels, with and without the support comb at the inlet end of the plates. 77

Figure 4.16. Deflection of the plate at two different points. Point 1 is located at 100 mm from the leading edge and Point 2 at 550 mm. 78

Figure 4.17. Maximum deflection of Plate 1 or 2 as a function of the square of the fluid velocity in the channels in Case 5. 78

Figure 4.18. Maximum deflection of Plate 1 or 2 as a function of the square of the fluid velocity in the channels: comparison between cases 1 and 5. 79

Figure D.1. Convergence history of Point A displacement for different fluid velocities in the channels in Case 1. 97

Figure D. 2. Convergence history of Point A displacement for different fluid velocities in the channels in Case 4. 97

1. INTRODUCTION

According to the International Atomic Energy Agency (IAEA), there are 226 operating research reactors and 9 under construction in the world (IAEA, 2019). These research facilities are utilized in countless ways to provide technical assistance in all engineering disciplines: medical and industrial isotope production, neutron beam based research, advanced materials research, and technology development for existing and advanced nuclear power capabilities. One aspect of their individuality may be seen in the fuel geometry each reactor employs. The use of plate-type fuel assemblies is common in nuclear research reactors (more frequently in Material Testing Reactors – MTRs). Plate-type fuel is potentially advantageous for numerous reasons including:

- An increase in thermal neutron flux,
- An increase in power density.

There are also some disadvantages to this type of fuel:

- It requires high precision and a significant increase in fabrication resources,
- It has a faster burn-up rate resulting in shorter core lifetimes,
- Its plates are prone to deflection when the fluid velocity is incremented.

This fuel element is an array of plates containing the nuclear fuel and separated by narrow channels through which the coolant flows to remove the heat generated by fission reactions. These plates have to be thin enough to prevent excessive internal temperature generation and yet strong enough to maintain stable configuration in permitting flow of coolant through the channels and insertion of control and shutdown elements. In most of the research reactor cores, a uniform distribution of coolant flow through each channel of the fuel element cannot be assumed due to factors such as plate roughness, manufacturing tolerances, turbulence and fluctuations produced by process equipment.

In parallel plate assemblies, there has been identified a phenomenon often referred to as *hydroelastic instability* of the plates. Its fundamental nature is that the fluid-dynamic forces acting on the structure are altered by the motion of the plates. As a result, it is possible for the structure to extract energy from the flow in such a way that

excessive deflections, eventually permanent deformation, or collapse of the fuel plates may occur. This behavior of the plates may cause local overheating and possibly a complete blockage of the coolant channels. The velocity at which that phenomenon occurs is called the critical fluid velocity. Thus, the estimation of this velocity is indispensable to establish the safety limitations and operating conditions of the reactors. These aspects are more important given the trend of utilization of nuclear fuel with higher uranium density and, therefore, reactor cores with higher power densities requiring higher coolant velocities. A flat-plate-type fuel element typical of a research reactor is shown in Figure 1.1.



Figure 1.1. Example of a plate-type fuel assembly.

1.1. Survey of Literature

For more than half a century, scientists have studied various aspects of plate stability under high-velocity fluid flow. Since the earliest research reactor designs, it was qualitatively postulated that there was a direct relation between flow and fuel plate deflection. Flat-plate fuel element has been studied more than any other geometric shape due to its vulnerability to failure caused by hydraulic forces, and its relatively weak structural capabilities with respect to other geometric forms including that of a cylindrical plate (Marcum, 2014).

One of the first published reports regarding flow-induced deflections in a plate-type assembly was written by Stromquist and Sisman (1948). The study was performed in a mockup and it was found that when the fluid velocity was raised to sufficiently high values, fuel plates deformed plastically. In 1958, the same problem was detected by Ronald Doan during the fuel element design, development and construction for

incorporation into the Engineering Test Reactor (ETR). Doan qualitatively discussed a critical flow field related to the onset of plastic plate deflection (Doan, 1958).

Daniel Miller used Doan's hypothesis and gave the first analysis of this phenomenon (Miller, 1958). In that work, Miller predicted that there is a velocity at which initially parallel plates become unstable and "collapse" toward each other. He based his original analysis on wide-beam and potential flow theories, thereby neglecting the three-dimensional nature of plate deflections.

According to Miller's model, plate deflection at coolant velocities lower than the collapse velocity causes a change in static pressure that is smaller than the elastic force in the plate; as a consequence, the deflection will disappear. For flow rates above this velocity, however, an initial deflection will grow until the plate either collapses by excessive deformation or touches an adjacent plate. A schematic representation of the shape of the original cross section of such assembly and the nature of the distortion that is postulated by Miller at the lowest critical flow velocity is shown in Figure 1.2.

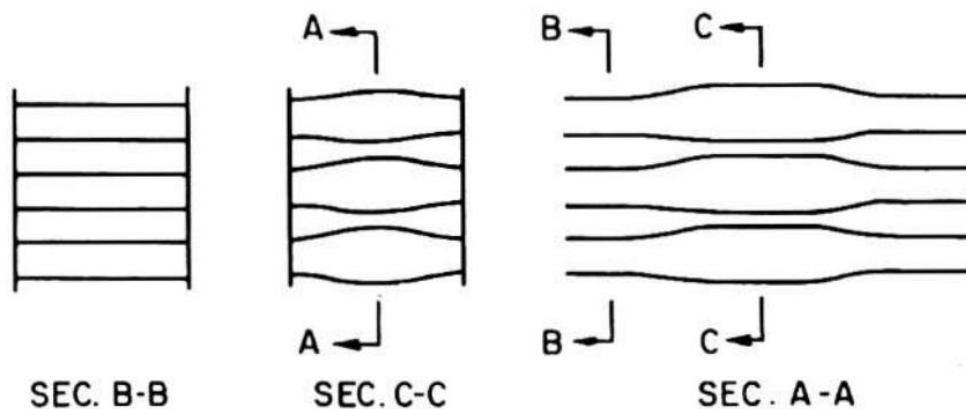


Figure 1.2. Outlines of plate assembly [taken from (Miller, 1958)].

For flat plate assemblies, Miller assumed:

- The plates are homogeneous, isotropic, elastic, initially flat, uniform in spacing and dimensions.
- The coolant is incompressible and all the coolant channels have the same mass flow.
- The plates are broad enough so that shear deformation is negligible, and are long enough so that they can deflect locally without significant redistribution of flow among the coolant channels.

- The plate edge supports are represented by ideal edge boundary conditions.

Considering a plate centered around two adjacent flow channels, the net pressure applied to the plate for a small differential change in the cross-sectional flow area is

$$p = \frac{\rho}{2} \left[\left(\frac{v_0}{1 - \frac{\Delta A}{A}} \right)^2 - \left(\frac{v_0}{1 + \frac{\Delta A}{A}} \right)^2 \right] \quad (1.1)$$

where A is the flow channel original, undeflected, cross-sectional area, ΔA is the total change in the cross-sectional area, ρ is the fluid density and v_0 the linear velocity of coolant in the undeformed channel. The pressure differential developed across the plate is derived from Bernoulli's theorem and can be simplified assuming that the plate undergoes very small deformation, for $\Delta A/A < 0.2$, equation (1.1) may be linearized to

$$p = \frac{2\rho v_0^2 \Delta A}{A} \quad (1.2)$$

The per-unit change in the channel cross section is,

$$\frac{\Delta A}{A} = \frac{(1 - \nu^2)pb^4}{30Ea^3h} \quad (1.3)$$

being E the Young's modulus of elasticity, ν the Poisson's ratio, h is the flow channel thickness, a and b are the plate thickness and width (wetted width), correspondingly. Substitution of (1.3) in (1.2) determines the critical velocity for stacks on the order of ten plates, each plate with two edges clamped and the other two considered free, and it is given by:

$$v_M = \sqrt{\frac{15Ea^3h}{\rho b^4(1 - \nu^2)}} \quad (1.4)$$

This velocity will herein be termed as the "Miller's velocity". In the case of a single plate bisecting a rigid duct, the critical velocity is higher by a factor of $\sqrt{2}$.

The main limitation of Miller's model is that the three-dimensional effects of the system are neglected. By assuming the plate to be a wide beam and considering a central portion of the plate, his equation neglects any local effects occurring in the vicinity of the

upstream or downstream edges. To date, Miller's theory is applied during the design of new fuel elements. For this purpose, reference (IAEA, 1980) recommends that the fluid velocity should be limited to two-thirds of the critical velocity given by Miller.

After Miller published his results, several attempts have been made to describe flow-induced deflections and to predict the occurrence of fuel plate collapse in plate-type assemblies, using analytical and experimental techniques. Zabriskie undertook a series of tests with mock fuel assemblies to experimentally verify Miller's critical velocity theory (Zabriskie, 1959, 1958). Zabriskie's work addressed both measurements of critical flow velocity and the effects of varying length and width on this velocity. A number of assemblies with single and multiple plates, different widths, different lengths, and different channel dimensions were tested. Most notably Zabriskie acknowledged that the critical flow velocity predicted by Miller's method does not cause a "collapse" of the flow channel, rather a point of maximum plate deflection is reached. He also noted the effects at the leading edges were very pronounced. Zabriskie concluded that due to the number of variables in Miller's critical velocity formula any small deviation from ideal conditions would have a large effect on the experimental results. One of the most universal trends started by Zabriskie was in comparing the measured critical velocity as a ratio to that predicted by Miller's method.

Johansson (1959) considered the effect of frictional pressure drop through the channel as well as the flow redistribution between constricted and expanded channels. He noted that the frictional pressure drop is larger through a constricted channel than it is through an expanded channel. It was also observed that these effects cause the deflected region to move downstream as the plate continues to deform. The most significant result of Johansson's work is that he showed that collapse occurs most readily near the inlet to the channels. Besides, he also highlighted that channel area change of 30% would be excessive.

In 1963, Kane analyzed an assembly containing an array of plates. In that study, Kane manufactured deviations or imperfections at the inlet of the channels between the fuel plates (Kane, 1963). It was detected that the calculated velocity using Miller's equation was the velocity at which significant deflections were initially perceived. Besides, Kane determined that these slight deviations at the inlet of the channel had a significant effect on the deflection through the channel especially at velocities greater

than Miller's approximation. In the same year, Groninger and Kane conducted a study, which focused on flow-induced deflections of different parallel plate assemblies (Groninger and Kane, 1963). The experimental setup showed that adjacent plates consistently deformed in opposite directions, with similar magnitudes, causing alternate closing and opening of the channel. Moreover, they noted a violent flutter of the plates at a velocity corresponding to 1.9 times the theoretical collapse velocity of the assembly.

In 1965, Scavuzzo coupled the hydraulic equations to the plate equations (Scavuzzo, 1965). The solution of these coupled equations was accomplished by changing the differential equation developed from plate theory into a nonlinear integral equation. To evaluate this integral equation numerically, the method of successive approximations was employed. Scavuzzo's principal conclusion was that deflections take place along the entire length of the plates.

Wambsganss (1967) made further improvements to Miller's model by considering the nonlinearity caused by large deflections. He did this by retaining the second-order bending terms for a wide beam in an attempt to assess their influence on stability. The second-order terms generate an additional stability criterion in the form of an upper bound on the amplitude of quasi-static deflections for stable oscillations. A new expression for critical velocity was derived:

$$v_w = \sqrt{\frac{15Ea^3h}{\rho b^4(1-v^2)}} \sqrt{\left[1 + \left(\frac{\delta_c}{\theta h}\right)^2\right] \left(\frac{15}{\phi}\right)} \quad (1.5)$$

Where θ and ϕ are the mode dependent constants, and δ_c is the critical plate deflection. It can be seen that the first term of the equation is the same as Miller's model, while the other term captures the second-order accurate physics of the model.

A study led by Roger Smith expanded on Miller's model once again (Smith, 1968). His model is also a semi-empirical model, which is based on a series of tests performed with gaseous fluid flows and several homogenous plate materials. Smith considered factors that quantified the increased deflection at the edges and the angle of attack produced at the edge. The resulting equation is shown below.

$$v_s = \sqrt{\frac{15Ea^3h}{\rho b^4(1-v^2)}} \sqrt{\frac{1}{\frac{1}{2}\left(1 + \frac{4\pi vlh}{b^2}\right)\left(1 + \frac{4vl^2}{3b^2}\right)}} \quad (1.6)$$

Notice that the first term in the above equation is the same as Miller's model, while the second term incorporates dynamic pressure drop variations along the axial length (l) of the plate. Although Smith's correlation includes more physics, it has not been employed in application because it produces a similar value to the velocity predicted by Miller, and Miller's formula had been used in industry for many years prior to the release of that new correlation.

Smissaert performed analytical and experimental investigations in an MTR fuel element (Smissaert, 1969, 1968). It was found that plates begin to experience static deflection at low velocities, as a result of static pressure differences in the coolant channels; at approximately twice that of Miller's velocity the plates experience a high amplitude flutter vibration. This velocity is known as the *flutter velocity*. The deflection that occurs at the leading edge was defined as *static divergence*. It physically means "that the plate will statically deflect until the elastic restoring force cancels the hydrodynamic pressure perturbation". Furthermore, Smissaert concluded that the deformation of fuel plates is a result of pressure differences in the channels between these plates. These pressure differences are originated from the static divergence of the leading edges and from the plate deflections beyond the leading edge. According to Smissaert, the presence of neighboring plates affects the lift force acting on the inlet edge of a plate.

The hydroelastic stability of a flat plate was examined by Weaver and Unny (1970). For this purpose, the classical linearized potential theory to describe the fluid-dynamic forces on the plate was used while the behavior of the plate was described with a modal approach in conjunction with small deflection theory. Their key finding was that the plate was found to become unstable statistically at first, but flutter was predicted for higher velocities.

Next Kim and Scarton presented an analysis of flow-induced bending of rectangular plates, with viscous entry flow differing in flow rate on top and bottom (Kim and Scarton, 1977). The classical theory of thin plate along with the boundary layer theory (Schlichting, 1968) was utilized. They concluded that, in order to have a

minimum deflection of the plates, it should be necessary to keep as small as possible the aspect ratio of the plates.

Cekirge and Ural (1978) used small deflection plate theory to update the critical flow velocity. They gained only a 4% margin over Miller's model. As a result of the analysis, they concluded that "*...Miller's velocity for the reactor design is quite a safe factor*", but it should be used with a safety factor.

A different analytical approach to predicting flow-induced deflections of stacked fuel plates was proposed by Pavone and Scarton (1983). A model of a single ETR plate based on classical thin plate theory was coupled with a laminar channel flow theory to determine flow-induced deflections. The model assumed the plate edges along the channel length were simply supported by the assembly walls and the plate edges at the channel inlet and exit were structurally free.

Davis and Kim found through numerical analysis that flat plates were expected to begin to deflect at velocities that were about 1.1 times Miller's critical velocity for both clamped and simply supported edges (Davis and Kim, 1991; Kim and Davis, 1995). The results showed that the plates would experience minor deflections and not a sudden collapse as Miller expected. They also detected that plates would begin to vibrate or experience dynamic divergence, at about two times Miller's approximation.

Guo and Paidoussis (2000) theoretically studied the stability of rectangular plates with free side-edges in inviscid channel flow. They treated the plate as one dimensional and the channel flow as two-dimensional. The Galerkin method was utilized to solve the plate equation, while the Fourier transform technique was employed to obtain the perturbation pressure from the potential flow equations. They investigated seven combinations of classical supports at the leading and trailing edges of the plates. It was concluded that divergence and coupled mode flutter may occur for plates with any type of end supports, while single-mode flutter only arises for non-symmetrically supported plates.

Another study conducted by Ho *et al.* (2004) gave evidence that Miller's critical velocity may not be as conservative as Smissaert suggested. That experimental study examined a system containing two fuel plates and used water at room temperature. They found that the plates collapsed at about 78% of Miller's approximation. One

method implemented in that study for the determination of plate collapse was the measurement of the pressure drop through the channels. Pressure drop through a channel can vary as a result of different channel cross-sectional areas leading to different velocities.

In 2004, the U.S. Department of Energy and the National Nuclear Security Administration established the Global Threat Reduction Initiative (GTRI) to reduce and secure nuclear material at civilian sites around the world (NTI, 2010). Through the Reduced Enrichment for Research and Test Reactors (RERTR) program, one of the goals of the GTRI is to minimize and eliminate the use of highly enriched uranium (HEU) in civilian applications by working to convert research and test reactors to the use of low enriched uranium (LEU). In the last decade, as a result of this program, there has been an increase of interest in the performance of parallel-plate fuel assemblies because new design of LEU plates is being projected, which are somewhat thinner plates.

Jensen and Marcum (2014) developed an analytical model to estimate the critical flow velocity of a laminate plate. They incorporated a flexural rigidity term into the formulation of the critical flow velocity derived by Miller, and the sandwich structure theory was employed to determine the rigidity term. As a result, a single equation for each of three different edge boundary conditions was proposed, which reliably and comprehensively predicts the onset of plate collapse.

Howard *et al.* (2015) provided an alternative approach to solving FSI problems using a 1-D, a semi-analytical model derived from first principles. The method was compared to an analytical solution, a numerical model, and experimental results. Although the solutions yielded from the study do not produce a “perfectly aligned” set of results as compared to the computational and experimental counterparts, representative solution forms were produced by the model.

Some researchers have also studied flow-induced deflections in fuel elements by coupling Computational Fluid Dynamics (CFD) and Finite Element Analysis (FEA) commercial codes. Kennedy simulated FSI in a plate-type element using two different codes, Star-CCM+ for solving the fluid domain, and Abaqus for solving the solid domain (Kennedy, 2012). His approach used a time-dependent solver to complete the runs. The decoupling of the physics necessary to run two different codes resulted in an unstable solution process. Curtis *et al.* (2013) developed a numerical model of two coolant

channels and one fuel plate. For the study, they chose the COMSOL software due to its ability to solve multiphysics problems using a fully-coupled and implicit solution algorithm. The solution matched with available experimental data. Moreover, it was demonstrated the COMSOL's potential to solve transient fully-coupled multiphysics problems.

Jesse developed a numerical model to assess the flow-induced deformation of the proposed low enriched uranium fuel plates for the University of Missouri Research Reactor by coupling Star-CCM+ with Abaqus (Jesse, 2015). The results of the FSI models were benchmarked against experiments conducted using a hydro-mechanical flow loop. Unfortunately, the models largely failed to predict the data collected during the experiments.

Again Kennedy, but during his doctorate, developed an FSI model by coupling the same codes used previously (Kennedy, 2015). Also, a flow loop and a test section were constructed for studying plate deflection and channel pressure drop for different fluid flow conditions. Experiments were completed on a single, flat 1.016 mm thick plate. The results showed that a flat plate is highly sensitive to small perturbations in the coolant channel geometry. The maximum deflection was noticed at the leading edge of the plate.

At the Instituto de Pesquisas Energéticas e Nucleares, with the construction of the new Brazilian Multipurpose Reactor (RMB by its acronym in Portuguese) and in order to understand the FSI phenomenon in plate-type assemblies, there has been a growing interest in the topic being discussed. Recently, an investigation was carried out by Alfredo J. Alvim de Castro (Castro, 2017) in an experimental setup. A test section that simulates a flat-plate fuel element with two plates and three-equal coolant channels was used. It was constructed with aluminum and lateral acrylic plates and was instrumented with strain gauge sensors, pressure sensors, accelerometer, and a pitot tube. Its proportions were based on the dimensions of an RMB's fuel element. The experiments performed accomplished the objective of reaching the collapse of the plates. The critical velocity detected was 14.5 m/s and the consequent permanent deformation of the plates was observed. The central channel had a 3 mm aperture in its center, causing a large blockage of the flow in the lateral channels. Comparatively, the value that was obtained for critical velocity was of the order of 85% of Miller's value.

1.1.1. Effects of Support Comb

As mentioned before, in nearly all prior research studies it has been found that the largest deflection occurs at the leading edge of the fuel plates. Frequently, in an attempt to stiffen that region, a support comb is inserted into each channel at the center of the width of the plates and these are supported between its “teeth”. A diagram of a comb is shown in Figure 1.3.

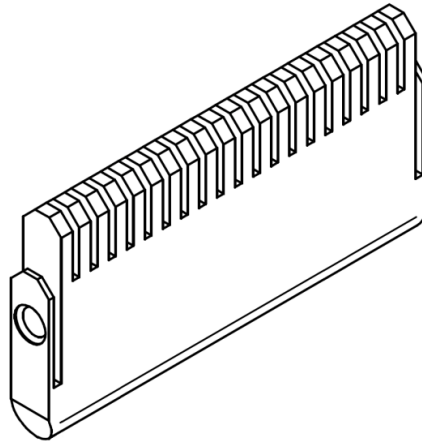


Figure 1.3. Diagram of a support comb.

Some authors have indicated that the static divergence at the inlet end of the plates could be easily mitigated with the addition of the comb (Groninger and Kane, 1963; Johansson, 1959; Smissaert, 1969, 1968; Zabriskie, 1958). Nevertheless, according to Groninger and Kane, even with a comb, “...*there are significant deflections two or three plate spans away from the inlet to the subassembly*”. These authors also noticed that channels with a larger thickness benefited more from the support combs.

Since Smissaert, almost no investigations have been concerned with the analysis of nuclear fuel plates with the inlet comb. After a deep search, the author can only list the technical report written by Tentner *et al.* (2017). In that effort, a numerical analysis of a single plate with a rigid mechanical stop that prevented the deflection of the plate at its leading edge was completed using the Abaqus software. It was observed that the maximum deflection occurred near the trailing edge. It was also recommended to perform additional studies to comprehend how the maximum deflection and its location change when the comb is installed.

1.2. Motivation

To date, even though a continued development and cost-effectiveness of computational techniques have happened, there are few works of fluid-structure interaction analyses of plate-type fuel elements by coupling CFD and FEA codes. In earlier numerical studies, a single-plate model has been assumed. Hence, taking into account Smissaert's conclusion that the inlet end of one plate is affected by the other plates, a study that models the fluid-structure interaction phenomenon between contiguous plates and proposes a numerical methodology to predict the critical velocity of parallel plate assemblies is desired.

Previous investigations have shown that plate collapse can occur at fluid velocities lower than Miller's velocity and that, even with a support comb, large deflections along the length of the plates are probable, thus producing unfamiliar regions in the structural stability of plate type assemblies that are of importance to the safety of future reactors. Besides, there is little information on the effect of manufacturing deviations and the change of materials properties due to the increment of temperature on the critical flow velocity and deflections of the plates.

1.3. Goals of the Study

The general aim of this work is to evaluate the mechanical stability of fuel plates under axial flow conditions by means of numerical FSI simulations. It consists of three main goals:

1. Develop a numerical methodology for predicting the onset of hydroelastic instability of nuclear fuel plates based on the RMB's fuel element geometry.
2. Use the numerical methodology and investigate the influence of manufacturing deviations and the change of materials properties due to the increment of temperature on the critical velocity and plate deflection. By manufacturing deviations, we mean plates and/or coolant channels with thicknesses different from the nominal condition.
3. Assess the effectiveness of using an inlet support comb on the mechanical stability of the fuel plates.

1.4. Importance of the Study

Numerical modeling and simulation assist greatly in gaining insights into fluid and structure problems in complex systems of nuclear reactors, allowing the analysis of these systems in dissimilar conditions that would be costly to investigate experimentally. The methodology presented here is important for updating the current techniques applied to the design of reactor fuel-plate assemblies. Besides, as far as this author knows, this is the first numerical analysis reported in the literature that models FSI phenomenon of neighboring plates with a support comb located at the midpoint of their inlet ends.

1.5. Document Organization

This document is organized as follows:

Chapter 1: Introduction – Introduction to the topic, a survey of available literature and the goals of this research.

Chapter 2: Fundamentals – This chapter introduces the fundamentals of fluid-structure interaction analysis, flow analysis using Computational Fluid Dynamics and structural analysis using the Finite Element Method.

Chapter 3: Numerical Methodology – Comprehensive description of the main features of the fluid and structural models, and the steps followed in the development of the fluid-solid model.

Chapter 4: Results and Discussion – Presentation of the results and discussion of the phenomena that are captured as part of this study.

Chapter 5: Conclusions and Future Works – Concluding remarks, observations relative to this work, and suggestions for future studies.

This manuscript closes with the list of referenced publications and appendices with additional details not contained within the chapters.

2. FUNDAMENTALS

This chapter briefly reviews the fundamentals of Computational Fluid Dynamics, Computational Solid Mechanics and fluid-structure interaction with emphasis on the current work.

2.1. Governing Equations of Fluid

Computational Fluid Dynamics is the analysis of systems involving fluid flow, heat transfer, and associated phenomena such as chemical reactions by means of computer-based simulation (Versteeg and Malalasekera, 2007). It works by solving the equations of fluid flow (in a special form) over a region of interest, with specified conditions on the boundary of that region. In general, all CFD codes are structured in four main stages:

Creating the geometry/mesh: In this stage, the geometry of the region of interest and its simplifications for the simulation are defined. In addition, the domain is divided into a number of smaller, non-overlapping sub-domains: a grid/mesh of cells (elements or control volumes).

Defining the physical model: In this step, the physical conditions of the problem are defined, such as the selection of the physical and/or chemical phenomena to be modeled, fluid properties, initial conditions of fluid flow, boundary conditions, and definition of numerical parameters and source terms.

Solution of the CFD problem: During this stage, a numerical algorithm for the conversion of the resulting integral equation into a system of algebraic equations, and its solution is used. The finite volume method is essential to the most-well established codes such as ANSYS CFX.

Analysis of results: In this phase, qualitative and quantitative results are extracted from the simulation through graphs, data, tables, visualization functions, etc.

CFD is fundamentally based on the governing equations of fluid dynamics. The governing equations represent mathematical statements of three fundamental physical principles (Tu et al., 2013):

- The mass of fluid is conserved;

- Newton's Second Law: The rate of change of momentum equals the sum of forces acting on the fluid;
- First Law of Thermodynamics: The rate of change of energy equals the sum of the rate of heat addition to and the rate of work done on the fluid.

The set of partial differential equations that describe the processes of momentum, energy and mass transfer are known as the Navier-Stokes equations. They were derived in the early nineteenth century and have no known general analytical solution but can be discretized and solved numerically. There are different solution methods that are used in CFD codes. The most universal, and the one on which ANSYS CFX is based, is the finite volume method (ANSYS Inc., 2017a).

In the finite volume technique, the geometry is divided into small sub-regions or control volumes (see Figure 2.1). With a systematic account of changes in the mass, momentum, and energy of the fluid element due to fluid flow across its boundaries, and where appropriate, due to the action of sources inside the volume, the fluid flow equations are obtained. These equations are discretized and solved iteratively for each control volume. As a result, an approximation of the value of each variable at specific points throughout the domain can be obtained. Thus, one derives a complete picture of the behavior of the fluid flow.

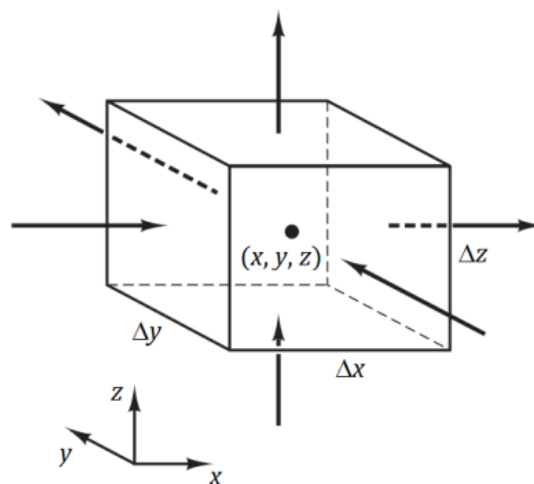


Figure 2.1. Control volume of fluid.

In a Cartesian system (x_j) , the instantaneous equations of mass and momentum conservation in an infinitesimally small control volume $\Delta x \Delta y \Delta z$, fixed in space, can be written as follows:

The Continuity Equation

$$\frac{\partial \rho}{\partial t} + \frac{\partial}{\partial x_j} (\rho U_j) = 0 \quad (2.1)$$

The Momentum Equation

$$\frac{\partial}{\partial t} (\rho U_i) + \frac{\partial}{\partial x_j} (\rho U_i U_j) = - \frac{\partial p}{\partial x_i} + \frac{\partial}{\partial x_j} \left[\mu \left(\frac{\partial U_i}{\partial x_j} + \frac{\partial U_j}{\partial x_i} \right) \right] + S_M \quad (2.2)$$

In these equations $i, j = 1, 2, 3$; U is the velocity, ρ the fluid density, μ the dynamic viscosity and S_M is the momentum source. The energy equation is not presented here because we are not considering heat transfer phenomena in the fuel assembly and the fluid is incompressible.

Many flows encountered in engineering problems become unstable above a certain Reynolds number (uL/ν where u and L are the characteristic velocity and length scales of the mean flow and ν is the kinematic viscosity, respectively). At low Reynolds numbers, flows are laminar. At greater Reynolds numbers, the inertia forces are sufficiently large to amplify the naturally occurring disturbances, and a transition to turbulence occurs. Here, an unstable state of motion develops in which the velocity and all other flow properties change continuously in a random and chaotic way (Tu et al., 2013). Turbulent flows are a complex process, mainly because they are three-dimensional, unsteady and consist of many scales.

2.1.1. Turbulence Models

Both laminar and turbulent flows satisfy equations (2.1) and (2.2). For laminar flow, where there are no random fluctuations, we go right to the attack and solve them for a variety of geometries. However, turbulent flows at realistic Reynolds numbers span a large range of turbulent length and time scales, and would generally involve length scales much smaller than the smallest finite volume mesh. The Direct Numerical Simulation (DNS) of these flows would require computing power that is many orders of magnitude higher than available in the foreseeable future.

To enable the effects of turbulence to be predicted, a large amount of CFD research has concentrated on methods that make use of *turbulence models*. These models have

been specifically developed to account for the effects of turbulence without recourse to a prohibitively fine mesh and direct numerical simulation (ANSYS Inc., 2017a).

As a general rule, turbulence models seek to modify the original Navier-Stokes equations by the introduction of averaged and fluctuating quantities, producing the Reynolds Averaged Navier-Stokes (RANS) equations. Because of the statistical averaging procedure used to obtain the equations, turbulence models based on RANS equations are identified as Statistical Turbulence Models (ANSYS Inc., 2017a). For instance, a velocity can be decomposed into a steady mean value \bar{U}_i with a fluctuating component u'_i superimposed on it: $U_i = \bar{U}_i + u'_i$. This is called the *Reynolds decomposition*. The time-averaged component is given by:

$$\bar{U}_i = \frac{1}{\Delta t} \int_t^{t+\Delta t} U_i dt \quad (2.3)$$

In the equation, Δt is a time scale that is large relative to the turbulent fluctuations. This process is the same for other flow properties. The mean quantities are substituted into the original continuity and momentum equations, resulting in the RANS equations given below.

$$\frac{\partial \rho}{\partial t} + \frac{\partial}{\partial x_j} (\rho \bar{U}_j) = 0 \quad (2.4)$$

$$\frac{\partial}{\partial t} (\rho \bar{U}_i) + \frac{\partial}{\partial x_j} (\rho \bar{U}_i \bar{U}_j) = - \frac{\partial \bar{p}}{\partial x_i} + \frac{\partial}{\partial x_j} \left[\mu \left(\frac{\partial \bar{U}_i}{\partial x_j} + \frac{\partial \bar{U}_j}{\partial x_i} \right) - \rho \overline{u'_i u'_j} \right] + S_M \quad (2.5)$$

The equations above are similar to those formulated in the preceding subsection, except for the presence of the additional terms $\rho \overline{u'_i u'_j}$, known as the Reynolds stresses, in the time-averaged momentum equation. These terms need to be modeled by extra equations of known variables in order to have a sufficient number of equations for all unknowns.

The time-averaged equations can be solved if Reynolds stresses are related to the mean flow. Boussinesq proposed in 1877 that the Reynolds stresses could be proportional to mean rates of deformation (Versteeg and Malalasekera, 2007):

$$-\rho \overline{u'_i u'_j} = \mu_t \left(\frac{\partial \bar{U}_i}{\partial x_j} + \frac{\partial \bar{U}_j}{\partial x_i} \right) - \frac{2}{3} \rho k \delta_{ij} \quad (2.6)$$

where $k = \frac{1}{2}(\overline{u'^2} + \overline{v'^2} + \overline{w'^2})$ is the turbulent kinetic energy per unit mass and μ_t is the turbulent or eddy viscosity. There is also a kinematic turbulent or eddy viscosity denoted by $\nu_t = \mu_t/\rho$. On the right hand side, the second term involves δ_{ij} , the Kronecker delta function ($\delta_{ij} = 1$ if $i = j$ and $\delta_{ij} = 0$ if $i \neq j$). During the last decades, different turbulence models to describe the turbulent viscosity have been developed. Eddy viscosity models represent several methods with different levels of complexity and accuracy such as algebraic (zero equation) models, one equation models, and two equation models, for instance, the k - ε and SST k - ω models. These two latter turbulence models are here indicated because are widely used in handling many turbulent fluid-engineering problems. Moreover, they have proven to be numerically robust, stable and with well-established predictive capabilities. In particular, satisfactory results with these models are reported in the literature for problems that involve narrow channels of research reactors (Andrade et al., 2015; Davari et al., 2015; Fan et al., 2015; Gong et al., 2015; Salama, 2011).

2.1.1.1. The k - ε Model

The k - ε model includes two extra transport equations to represent the turbulent properties of the flow. This model assumes that the turbulence viscosity is linked to the turbulence kinetic energy and dissipation via the following relation:

$$\mu_t = \rho C_\mu \frac{k^2}{\varepsilon} \quad (2.7)$$

The equations for the turbulent kinetic energy and turbulence dissipation rate are:

$$\frac{\partial}{\partial t}(\rho k) + \frac{\partial}{\partial x_j}(\rho U_j k) = \frac{\partial}{\partial x_j} \left[\left(\mu + \frac{\mu_t}{\sigma_k} \right) \frac{\partial k}{\partial x_j} \right] + P_k + P_{kb} - \rho \varepsilon \quad (2.8)$$

$$\frac{\partial}{\partial t}(\rho \varepsilon) + \frac{\partial}{\partial x_j}(\rho U_j \varepsilon) = \frac{\partial}{\partial x_j} \left[\left(\mu + \frac{\mu_t}{\sigma_\varepsilon} \right) \frac{\partial \varepsilon}{\partial x_j} \right] + \frac{\varepsilon}{k} (C_{\varepsilon 1} P_k + C_{\varepsilon 1} P_{\varepsilon b} - C_{\varepsilon 2} \rho \varepsilon) \quad (2.9)$$

The physical significance of the above equations is that the rate of change and the advection transport of k or ε equals the diffusion transport combined with the rate of

production and destruction of k or ε . These equations contain five constants: $C_\mu = 0.09$, $C_{\varepsilon_1} = 1.44$, $C_{\varepsilon_2} = 1.92$, $\sigma_k = 1.0$ and $\sigma_\varepsilon = 1.3$. These constants have been arrived at by comprehensive data fitting for a wide range of turbulent flows (Launder and Spalding, 1974). P_k is the turbulence production due to viscous forces, P_{kb} and $P_{\varepsilon b}$ represent the influence of the buoyancy forces, which are modeled using:

$$P_k = \mu_t \left(\frac{\partial U_i}{\partial x_j} + \frac{\partial U_j}{\partial x_i} \right) \frac{\partial U_i}{\partial x_j} - \frac{2}{3} \frac{\partial U_k}{\partial x_k} \left(3\mu_t \frac{\partial U_k}{\partial x_k} + \rho k \right) \quad (2.10)$$

If a full buoyancy model is used, the term P_{kb} is then:

$$P_{kb} = -g_i \frac{\mu_t}{\rho \sigma_\rho} \frac{\partial \rho}{\partial x_i} \quad (2.11)$$

while, if the Boussinesq model is utilized, it is:

$$P_{kb} = g_i \beta \frac{\mu_t}{\rho \sigma_\rho} \frac{\partial T}{\partial x_i} \quad (2.12)$$

The term $P_{\varepsilon b}$ is proportional to P_{kb} and it is defined as:

$$P_{\varepsilon b} = \max(0, P_{kb}) \quad (2.13)$$

But, if the directional option is considered, this term is modified by a factor accounting for the angle ϕ between gravity and velocity vectors,

$$P_{\varepsilon b} = \max(0, P_{kb}) \sin \phi \quad (2.14)$$

The constant σ_ρ is 0.9 for Boussinesq buoyancy and it is 1 for the full model buoyancy.

2.1.1.2. The SST k - ω Model

The Shear Stress Transport model (SST) combines the best properties of the k - ε and k - ω models (Menter, 1994). It is a model that gives accurate predictions of the onset and the amount of flow separation under adverse pressure gradients (ANSYS Inc., 2017a).

In the k - ω based SST model, the transport equations for the turbulent kinetic energy (k) and the turbulent frequency (ω) are:

$$\frac{\partial}{\partial t}(\rho k) + \frac{\partial}{\partial x_j}(\rho U_j k) = \frac{\partial}{\partial x_j} \left[\left(\mu + \frac{\mu_t}{\sigma_{k3}} \right) \frac{\partial k}{\partial x_j} \right] + P_k + P_{kb} - \beta' \rho k \omega \quad (2.15)$$

$$\begin{aligned} \frac{\partial}{\partial t}(\rho \omega) + \frac{\partial}{\partial x_j}(\rho U_j \omega) &= \frac{\partial}{\partial x_j} \left[\left(\mu + \frac{\mu_t}{\sigma_{\omega 3}} \right) \frac{\partial \omega}{\partial x_j} \right] + 2\rho(1 - F_1) \frac{1}{\sigma_{\omega 2} \omega} \frac{\partial k}{\partial x_j} \frac{\partial \omega}{\partial x_j} + \\ &+ \alpha_3 \frac{\omega}{k} P_k + P_{\omega b} - \beta_3 \rho \omega^2 \end{aligned} \quad (2.16)$$

For this model, the blending functions are critical. They are based on the distance to the nearest wall (y) on the flow variables.

$$F_1 = \tanh \left\{ \left\{ \min \left[\max \left(\frac{\sqrt{k}}{\beta' \omega y}, \frac{500\nu}{y^2 \omega} \right), \frac{4\rho k}{CD_{k\omega} \sigma_{\omega 2} y^2} \right] \right\}^4 \right\} \quad (2.17)$$

$$F_2 = \tanh \left\{ \left[\max \left(\frac{2\sqrt{k}}{\beta' \omega y}, \frac{500\nu}{y^2 \omega} \right) \right]^2 \right\} \quad (2.18)$$

$$CD_{k\omega} = \max \left(2\rho \frac{1}{\sigma_{\omega 2} \omega} \frac{\partial k}{\partial x_j} \frac{\partial \omega}{\partial x_j}, 1.0 \times 10^{-10} \right) \quad (2.19)$$

$$P_k = \min(2\mu_t S_{ij} S_{ij}, 10\rho\beta' k \omega) \quad (2.20)$$

$$\mu_t = \frac{\rho \alpha_1 k}{\max(\alpha_1 \omega, F_2 \sqrt{S_{ij} S_{ij}})} \quad (2.21)$$

$$\Phi_3 = F_1 \Phi_1 + (1 - F_1) \Phi_2 \quad (2.22)$$

The coefficients for this model are: $\alpha_1 = 5/9$, $\alpha_2 = 0.44$, $\beta' = 0.09$, $\beta_1 = 0.075$, $\beta_2 = 0.0828$, $\sigma_{k1} = 2$, $\sigma_{k1} = 1$, $\sigma_{\omega 1} = 2$ and $\sigma_{\omega 2} = 1/0.856$. The values of the new constants are a linear combination for any constant (Φ), as indicated in equation (2.22).

2.1.2. Near-Wall Modeling

Close to no-slip solid walls, the flow is influenced by viscous effects and does not depend on free stream parameters. The representation of these processes within a numerical simulation raises the following problems:

- How to account for viscous effects at the wall.

- How to resolve the rapid variation of flow variables that occurs within the boundary layer region.

In turbulent flows, the flow gradient normal to the wall tends to develop on small scales. Near-wall regions, the viscosity-affected region is made up of three zones: *viscous sublayer*, *buffer layer* and *log-law layer*. The figure below illustrates these subdivisions.

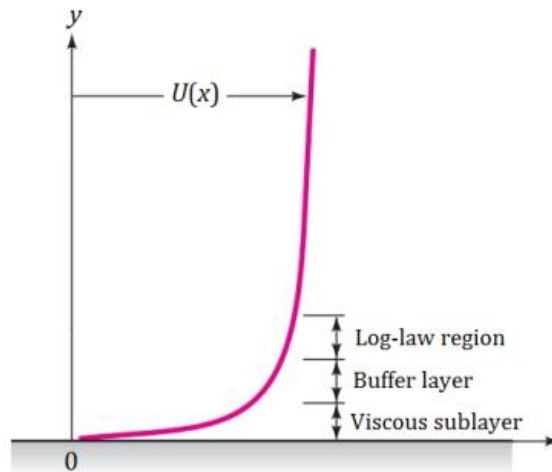


Figure 2.2. Typical velocity distribution in the turbulent flow near a solid boundary [adapted from (White, 2011)].

Close to the wall the flow is influenced by viscous effects and does not depend on free stream parameters. The mean flow velocity only depends on the distance from the wall (y), fluid density and viscosity and the wall shear stress (τ_w). Then, an expression for the velocity takes the form (Versteeg and Malalasekera, 2007):

$$u^+ = \frac{U}{u_\tau} = f\left(\frac{\rho u_\tau y}{\mu}\right) = f(y^+) \quad (2.23)$$

The above formula is called the *law of the wall*. u^+ and y^+ are dimensionless variables of the near wall velocity and distance, respectively. The quantity $u_\tau = \sqrt{\tau_w/\rho}$ is termed the *friction velocity*, although it is not actually a flow velocity.

The viscous sublayer is in practice extremely thin ($y^+ \leq 5$) and we may adopt that the shear stress is approximately constant and equal to the wall shear stress throughout the layer (Versteeg and Malalasekera, 2007). Thus

$$\tau(y) = \mu \frac{\partial U}{\partial y} \cong \tau_w \quad (2.24)$$

Integrating with respect to y and applying the boundary condition $U = 0$ when $y = 0$, a linear relationship between the mean velocity and the distance from the wall is obtained,

$$U = \frac{y\tau_w}{\mu} \quad (2.25)$$

After some simple algebra, this leads to $u^+ = y^+$. Because of the linear relationship between velocity and distance from the wall, the fluid layer adjacent to the wall is also known as the *linear sublayer*. While directly solving the viscous sublayer may provide a more precise solution, it also requires very fine mesh in the near-wall zone and, correspondingly, higher computer-storage requirements and longer runtimes.

The flow at a distance of $30 \leq y^+ < 500$ from the wall exhibits a logarithmic behavior. Viscous and turbulent effects are both important in this region, and the relationship between the velocity and the wall distance is expressed as:

$$u^+ = \frac{1}{\kappa} \ln(y^+) + B \quad (2.26)$$

Over the full range of turbulent smooth wall flows, the von Karman's constant $\kappa \approx 0.41$ and the additive constant $B \approx 5.5$; wall roughness causes a decrease in the value of B (Versteeg and Malalasekera, 2007). Because of the logarithmic relationship between u^+ and y^+ , equation (2.26) is called the *log-law*, and the layer where y^+ takes values between 30 and 500 the *log-law layer* (see Figure 2.2). When the first node of the grid is located in the log-law layer, it is possible to use coarse meshes in the CFD model.

Wall functions, which originate from the log-law, are the most popular way to account for near-wall effects. When these functions are considered, typically y^+ values close to the lower bound 30 are recommended (ANSYS Inc., 2017a; Salim and Cheah, 2009). In this work, taking into account the software capabilities and the good balance between robustness, computational cost, and accuracy, wall functions to approximate the behavior of the flow near the solid wall are used.

2.1.3. Boundary Conditions

The governing equations of CFD have been presented in the previous subsections. However, the actual driver for any particular solution is the *boundary conditions* (Tu et al., 2013). These conditions must be applied to all bounding regions of the domain.

Boundary conditions include inlets, outlets, openings, walls and symmetry planes (ANSYS Inc., 2017a).

The boundary condition on a solid surface assumes zero relative velocity between surface and fluid immediately at the surface. This is the so-called *no-slip* condition. If the surface is stationary, with the flow moving past it, then all the velocity components can be taken to be zero,

$$u = v = w = 0 \text{ at the surface} \quad (2.27)$$

The solution of the governing equations for the transport property requires at least one velocity component to be given at the inflow boundary. This is provided by the *Dirichlet* boundary condition on the velocity in a specific direction $U_j = f$. At the surface, f can be specified as a constant value or a velocity profile. Dirichlet conditions can be applied accurately as long as f is continuous. At locations where the fluid flow is roughly unidirectional and where surface stresses take known values, the outflow boundary condition is used, i.e.:

$$\frac{\partial u}{\partial n} = \frac{\partial v}{\partial n} = \frac{\partial w}{\partial n} = 0 \quad (2.28)$$

being n the normal direction to the surface. This condition is commonly known as the *Neumann boundary condition*.

Other frequently used boundary conditions included the open, symmetric, average static pressure and cyclic boundary conditions. The open condition simply states that the normal gradient of the transport property ϕ is zero, i.e. $\partial\phi/\partial n = 0$. On the other hand, symmetric and cyclic boundary conditions can be employed to take advantage of special geometrical features of the region of interest. For the symmetry boundary condition, the normal velocity at the surface is zero while the normal gradients of the other velocity components are zero, where the latter condition also applies for any scalar quantity. For the cyclic boundary condition, the transport property of the one surface ϕ_1 is equivalent to the transport property of the second surface ϕ_2 (i.e. $\phi_1 = \phi_2$). This depends on which two surfaces of the domain experience periodicity (Tu et al., 2013).

The average static pressure allows the pressure profile at the outlet to vary based on upstream influences while constraining the average pressure to a specified value p_{spec} , where:

$$p_{spec} = \frac{1}{A} \int_S p_{ip} dA \quad (2.29)$$

where p_{ip} is the imposed pressure at each integration point. The integral is evaluated over the entire outlet boundary surface.

2.2. Governing Equations of Solid

Transient dynamic analysis is a technique to find out the dynamic response of a structure under the action of any time-dependent load. The time-history analysis, as it is also known, can be used to find the time-varying displacements, strains, stresses and forces in a structure corresponding to any combination of static, transient and harmonic loads (ANSYS Inc., 2017b).

The dynamic response of the structure herein studied is described by the following basic equation of motion:

$$[M]\ddot{\vec{Q}} + [C]\dot{\vec{Q}} + [K]\vec{Q} = \vec{P}(t) \quad (2.30)$$

in which $[M]$ is the mass matrix of the structure, $\ddot{\vec{Q}}$ the vector of nodal acceleration in the global system, $[C]$ the damping matrix of the structure, $\dot{\vec{Q}}$ the global nodal velocity vector, $[K]$ the stiffness matrix, \vec{Q} the global nodal displacement vector, and $\vec{P}(t)$ the total load vector changing with time. Equation (2.30) is solved using the finite element method (FEM) (Rao, 2011; Zienkiewicz et al., 2013).

2.2.1. Overview of the Finite Element Method

The finite element method originated as a method of stress analysis but, today, it is also used to analyze problems of heat transfer, fluid flow, electric, and many others (Zienkiewicz et al., 2013). In this method, the actual continuum or body of matter is represented as an assemblage of subdivisions called “finite elements”. Figure 2.3 provides examples of elements employed in different dimensions. These elements are considered to be interconnected at specified joints called nodal points or nodes. By

solving the finite element equations, the nodal values of the field variable will be known. Once these are determined, approximating functions define the field variable throughout the assemblage of elements (Rao, 2011).

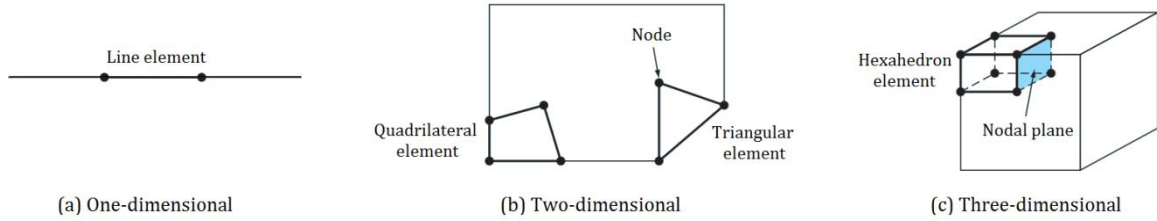


Figure 2.3. Example of elements employed in one, two and three dimensions [modified from (Chapra and Canale, 2015)].

In dynamic problems, the displacements, velocities, strains, stresses, and loads are all time dependent. After idealizing the body into finite elements, the displacement model of element e can be supposed as:

$$\vec{U}(x, y, z, t) = \begin{Bmatrix} u(x, y, z, t) \\ v(x, y, z, t) \\ w(x, y, z, t) \end{Bmatrix} = [N(x, y, z)]\vec{Q}^{(e)}(t) \quad (2.31)$$

where \vec{U} is the vector of displacement, $[N]$ is the matrix of shape functions, and $\vec{Q}^{(e)}$ is the vector of nodal displacements that is assumed to be a function of time t .

The next step in a finite element analysis is to derive the element stiffness and mass matrices and characteristic load vector. From equation (2.31), we can express the strains and the stresses as:

$$\vec{\epsilon} = [B]\vec{Q}^{(e)} \quad (2.32)$$

$$\vec{\sigma} = [D]\vec{\epsilon} = [D][B]\vec{Q}^{(e)} \quad (2.33)$$

By differentiating equation (2.31) with respect to time, the velocity field can be calculated as

$$\dot{\vec{U}}(x, y, z, t) = [N(x, y, z)]\dot{\vec{Q}}^{(e)}(t) \quad (2.34)$$

where $\dot{\vec{Q}}^{(e)}$ is the vector of nodal velocities. To derive the dynamic equations of motion of a structure, the Lagrange equations can be used (Rao, 2011). These are given by:

$$\frac{d}{dt} \left\{ \frac{\partial L}{\partial \dot{Q}} \right\} - \left\{ \frac{\partial L}{\partial Q} \right\} + \left\{ \frac{\partial R}{\partial \dot{Q}} \right\} = \{0\} \quad (2.35)$$

$$L = T - \pi_p \quad (2.36)$$

being L the Lagrangian function, T the kinetic energy, π_p the potential energy, R the dissipation function, Q the nodal displacement, and \dot{Q} is the nodal velocity. The kinetic and potential energies of an element e can be defined as follows:

$$T^{(e)} = \frac{1}{2} \iiint_{V^{(e)}} \rho \dot{\vec{U}}^T \dot{\vec{U}} dV \quad (2.37)$$

$$\pi_p^{(e)} = \frac{1}{2} \iiint_{V^{(e)}} \vec{\epsilon}^T \vec{\sigma} dV - \iint_{S^{(e)}} \vec{U}^T \vec{\Phi} dS - \iiint_{V^{(e)}} \vec{U}^T \vec{\phi} dV \quad (2.38)$$

where $V^{(e)}$ is the volume, ρ is the density, and $\dot{\vec{U}}$ is the vector of velocities of element e . If we suppose the existence of dissipative forces proportional to the relative velocities, the dissipation function of the element e is

$$R^{(e)} = \frac{1}{2} \iiint_{V^{(e)}} \lambda \dot{\vec{U}}^T \dot{\vec{U}} dV \quad (2.39)$$

where λ is called the damping coefficient. In equations (2.37) to (2.39), the volume integral has to be taken over the volume of the element, and in equation (2.38) the surface integral has to be taken over that portion of the surface of the element on which distributed forces are prescribed. By using equations (2.31) to (2.33), the expression for T , π_p and R can be written as:

$$T = \sum_{e=1}^n T^{(e)} = \frac{1}{2} \dot{\vec{Q}}^T \left[\sum_{e=1}^n \iiint_{V^{(e)}} \rho [N]^T [N] dV \right] \dot{\vec{Q}} \quad (2.40)$$

$$\begin{aligned} \pi_p &= \sum_{e=1}^n \pi_p^{(e)} = \frac{1}{2} \vec{Q}^T \left[\sum_{e=1}^n \iiint_{V^{(e)}} [B]^T [D] [B] dV \right] \vec{Q} \\ &- \vec{Q}^T \left(\sum_{e=1}^n \iint_{S^{(e)}} [N]^T \vec{\Phi}(t) dS + \iiint_{V^{(e)}} [N]^T \vec{\varphi}(t) dV \right) - \vec{Q}^T \vec{P}_c(t) \end{aligned} \quad (2.41)$$

$$R = \sum_{e=1}^n R^{(e)} = \frac{1}{2} \dot{\vec{Q}}^T \left[\sum_{e=1}^n \iiint_{V^{(e)}} \mu [N]^T [N] dV \right] \dot{\vec{Q}} \quad (2.42)$$

where \vec{P}_c is the vector of concentrated nodal forces of the body or structure. \vec{Q} and $\dot{\vec{Q}}$ have been named earlier for equation (2.30). The matrices involving the integrals are

$$[M^{(e)}] = \text{element mass matrix} = \iiint_{V^{(e)}} \rho [N]^T [N] dV \quad (2.43)$$

$$[K^{(e)}] = \text{element stiffness matrix} = \iiint_{V^{(e)}} [B]^T [D] [B] dV \quad (2.44)$$

$$[C^{(e)}] = \text{element damping matrix} = \iiint_{V^{(e)}} \mu [N]^T [N] dV \quad (2.45)$$

$\vec{P}_s^{(e)}$ = vector of element nodal forces produced by surface forces

$$= \iint_{S^{(e)}} [N]^T \vec{\Phi} \cdot dS \quad (2.46)$$

$\vec{P}_b^{(e)}$ = vector of element nodal forces produced by body forces

$$= \iiint_{V^{(e)}} [N]^T \vec{\varphi} \cdot dV \quad (2.47)$$

In order to assemble the element matrices and vectors and derive the overall system equations of motion, we can rewrite equations (2.40) to (2.42):

$$T = \frac{1}{2} \dot{\vec{Q}}^T [M] \dot{\vec{Q}} \quad (2.48)$$

$$\pi_p = \frac{1}{2} \vec{Q}^T [K] \vec{Q} - \vec{Q}^T \vec{P} \quad (2.49)$$

$$R = \frac{1}{2} \dot{\vec{Q}}^T [C] \dot{\vec{Q}} \quad (2.50)$$

where

$$[M] = \sum_{e=1}^n [M^{(e)}] \quad (2.51)$$

$$[K] = \sum_{e=1}^n [K^{(e)}] \quad (2.52)$$

$$[C] = \sum_{e=1}^n [C^{(e)}] \quad (2.53)$$

$$\vec{P}(t) = \sum_{e=1}^n \left(P_s^{(e)}(t) + P_b^{(e)}(t) \right) + \vec{P}_c(t) \quad (2.54)$$

By substituting equations (2.48) to (2.50) into (2.35), the dynamic equation (2.30) is obtained. That equation is then solved by applying the initial and boundary conditions of the system. Once the time history of nodal displacements, \vec{Q} , is known, the time histories of strains and stresses can be found. More details about the finite element method applied to dynamic problems can be consulted in reference (Rao, 2011).

2.3. Coupling Conditions

In fluid-structure coupling problems, the mechanical quantities of the two fields are exchanged at the interface. In particular, the fluid passes forces to the solid, while the solid sends displacements back to the fluid. At the interface between the solid and the fluid, the kinematic condition requires the velocity of the fluid (U_f) to be equal to the time derivative of the displacement of the solid interface or velocity (U_s):

$$U_s = U_f \quad (2.55)$$

The dynamic condition ensures the compatibility of traction across the FSI interface and gives rise to

$$n \cdot \sigma_s = -n \cdot \sigma_f \quad (2.56)$$

where n is the unit normal vector of the interface, and σ_s and σ_f denotes the solid and fluid stress, respectively. By implementation of the kinematic condition, fluid nodes on the interface are updated according to their corresponding solid nodes. By doing the same for the dynamic condition, the equilibrium of stress on the FSI interface is ensured. Then, the fluid pressure is integrated into a fluid force, which is used in applying to the solid nodes along the interface.

3. NUMERICAL METHODOLOGY

The geometry modeled was based on the geometric and hydraulic characteristics of a typical fuel element of the future Brazilian Multipurpose Reactor (Perrotta and Soares, 2015). Each RMB's fuel element will contain 21 fuel plates and its dimensions are $80.5 \text{ mm} \times 80.5 \text{ mm} \times 1045 \text{ mm}$. Each fuel plate consists of a meat of low enriched uranium-silicide (U_3Si_2) powder dispersed in an aluminum matrix. The fuel meat is hermetically sealed between aluminum-alloy covers (the cladding).

Generic diagrams of the domains are shown in Figure 3.1. In the figure, the dark blue arrows indicate the fluid flow direction. The geometric specifications for the different cases are detailed in Table 3.1.

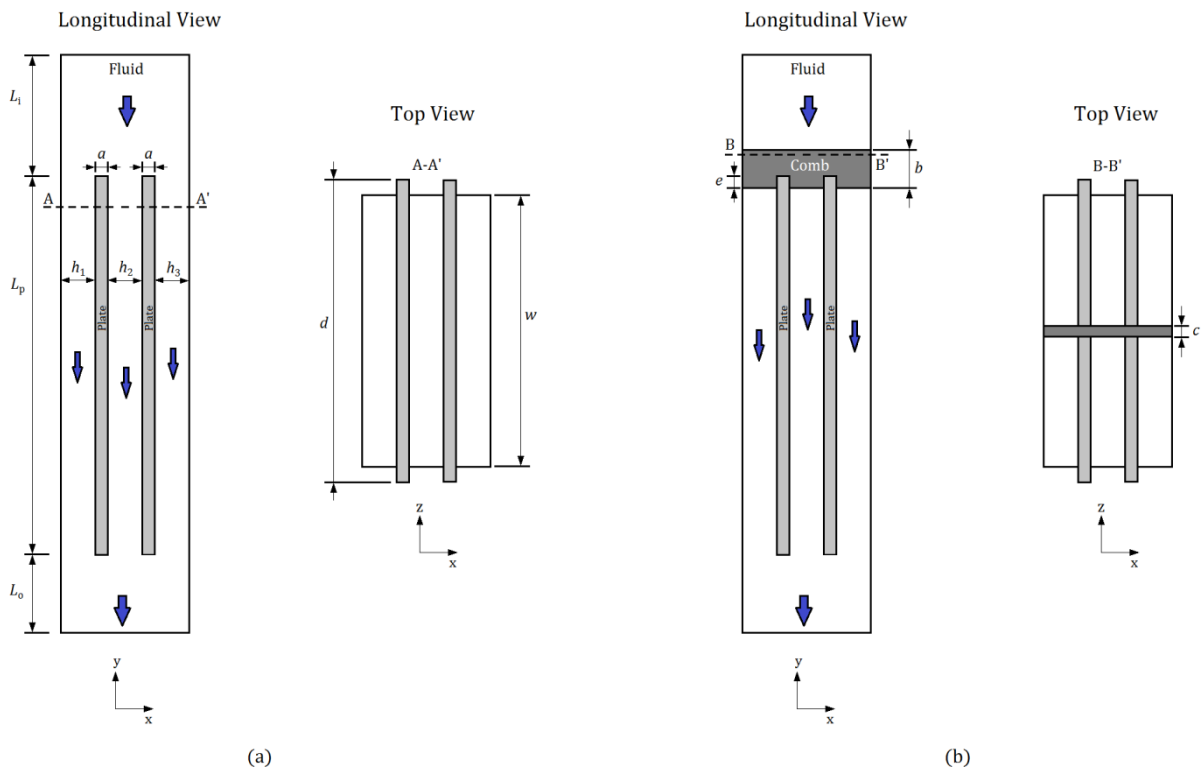


Figure 3.1. (a) Generic diagrams of the computational domain without and (b) with the support comb.

The present study consists of five different cases:

- Case 1: Considers an array of two-equal plates and three-equal flow channels, all with nominal dimensions. Materials properties at room temperature ($24 \text{ }^\circ\text{C}$).

- Case 2: Considers an array of two-equal plates and three-equal flow channels, all with thicknesses smaller than the nominal dimensions. Materials properties at room temperature.
- Case 3: Considers the same plates of Case 2 but two coolant channels with equal dimensions and the other one with a different thickness. Materials properties at room temperature.
- Case 4: Considers the plates and coolant channels with nominal dimensions but materials properties at operating temperatures, i.e. an average temperature of 50 °C and 120 °C for the fluid flow and the plates was set, respectively. The latter is approximately the maximum temperature that can be reached in a fuel plate during normal operation.
- Case 5: The configuration considered here is the same as for Case 1 but including a support comb at the leading edge of the plates.

Table 3.1. Geometric specifications for each case.

Parameter	Case			
	1 & 4	2	3	5
Channel 1- thickness, h_1 (mm)	2.45	2.35	2.35	2.45
Channel 2 - thickness, h_2 (mm)	2.45	2.35	2.35	2.45
Channel 3 - thickness, h_3 (mm)	2.45	2.35	2.55	2.45
Channels - width, w (mm)	70.5	70.5	70.5	70.5
Channels (plates) - length, L_p (mm)	655	655	655	655
Plates - thickness, a (mm)	1.35	1.33	1.33	1.35
Plates - width, d (mm)	75	75	75	75
Inlet plenum - length, L_i (mm)	190	190	190	190
Outlet plenum - length, L_o (mm)	70	70	70	70
Support comb - height, b (mm)	-	-	-	40
Support comb - thickness, c (mm)	-	-	-	8
Support comb - finger, e (mm)	-	-	-	11.5

3.1. Multiphysics Analysis with ANSYS

In fluid-structure interaction simulations, the fields are interfaced via the so-called wet surface where the pressure and friction forces produced by the fluid are acting on the structure. Because of the pressure loads caused by the flow, the body becomes deformed changing the boundaries of the fluid domain and, as a result, the flow pattern has to adapt to the modified boundary (Rao, 2003).

Solution strategies for FSI simulations are divided into monolithic and partitioned methods; this work focuses only on partitioned methods where the fluid and structure subproblems are solved iteratively. This requires two codes: one for solving the fluid-dynamics equations and the other for the solid part. This technique is divided into two categories: one-way and two-way coupling. The technique used here is the two-way coupling between ANSYS CFX and ANSYS Mechanical (Transient Structural module) (ANSYS Inc., 2017a, 2017b).

Fluid and solid domain/physical models are created in the ANSYS CFX-Pre and ANSYS Mechanical user interfaces, respectively. Coupling data transfers and controls are specified in the ANSYS CFX-Pre. Both have unlike meshing requirements and different meshes can be generated for the fluid field and the solid field. The meshes might not be equal at the interface but must consist of the identical geometric surface. During two-way coupling calculations, both solvers execute the simulation throughout a sequence of multi-field time steps, each of which consists of one (*explicit*) or more (*implicit*) coupling iterations. The FEA solver acts as a coupling master process to which the CFD solver connects. Once the connection is established, the solvers advance through a sequence of pre-defined synchronization points (SPs). At each of these SPs, information is exchanged between the solvers (ANSYS Inc., 2017a). This process of data sharing between structure and fluid field continues until the required conditions are satisfied.

In an implicit two-way coupling simulation, data between the solvers are exchanged many times in a time step and until the convergence is reached. Afterward, a new time step begins. The drawback of this technique is that there is a substantial increment of computational cost. In contrast, in explicit two-way coupling simulations, smaller time steps are required; the convergence at the fluid-solid interface during a time step may be not reached and a new time step is launched directly. However, at the end of the simulation time, the convergence is necessary.

Given that this work is concerned with the steady-state and static deformation of the plates and the available computational resources, the explicit coupling scheme was chosen. Figure 3.2 shows the process flowchart for the two-way coupling algorithm.

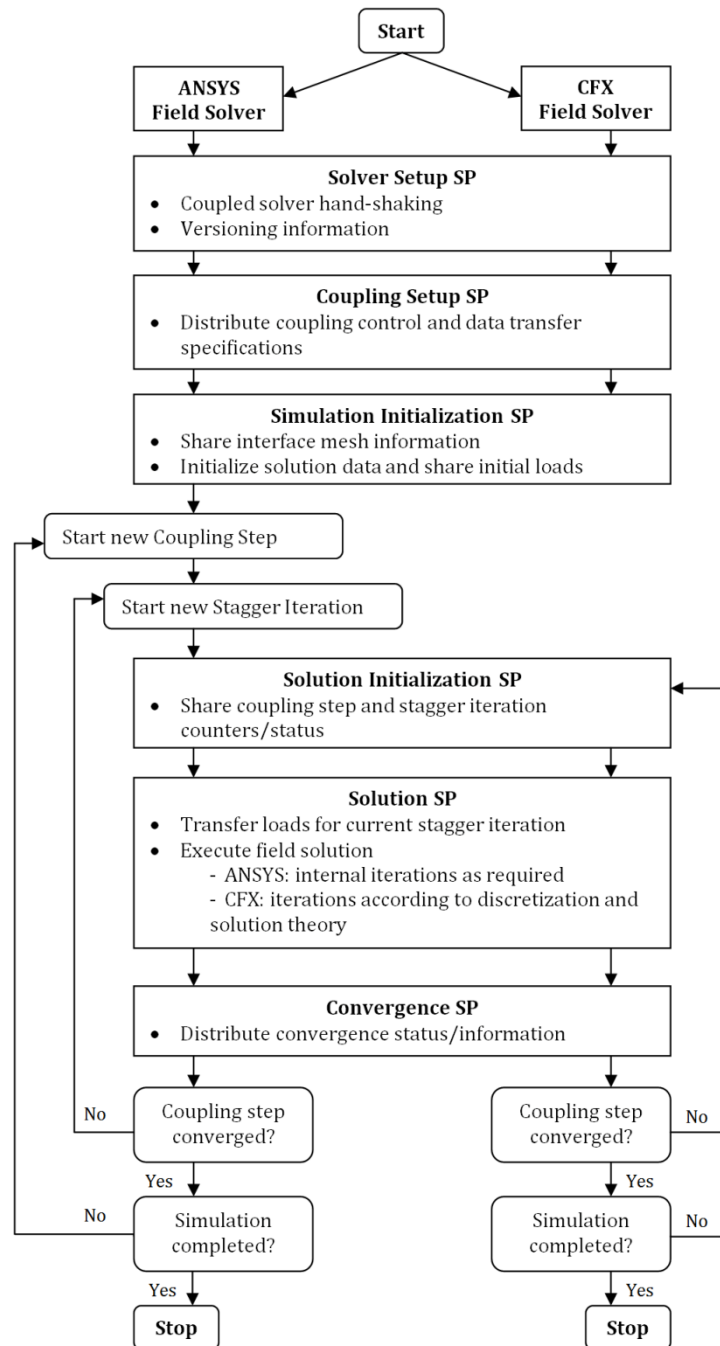


Figure 3.2. Flowchart of a two-way FSI analysis [modified from (ANSYS Inc., 2017a)].

3.2. Verification and Validation

Solution verification is an important aspect of ensuring that a given simulation of a mathematical model is sufficiently accurate for the intended use. According to

Oberkampf and Roy (2010), during solution verification, the main focus is the estimation of the numerical errors that occur when a mathematical model is discretized and solved on a digital computer. On the other hand, in the validation process, the result of a simulation is compared with experimental data for specific conditions.

In this study, in order to create an adequate mesh for the multiphysics analysis, the fluid and structural models were verified independently. In addition, a validation study was performed.

3.2.1. Grid Convergence Index

Numerical errors can arise in scientific computing due to computer round-off, statistical sampling, iteration, and discretization. Discretization error is frequently the largest numerical error source and not easy to estimate. Therefore, a vital study during a numerical analysis is to investigate the influence of the domain discretization in the solution. It is important to mention that discretization errors are associated with the mesh resolution and quality as well as the time step chosen for unsteady problems (Oberkampf and Roy, 2010).

In 2009, the “Standard for Verification and Validation in Computational Fluid Dynamics and Heat Transfer” was published by The American Society of Mechanical Engineers (ASME, 2009). In that best practice guideline, the Grid Convergence Index (GCI) was recommended for estimation and reporting of uncertainty due to discretization. The method was developed by Roache (1998) and is based on the Richardson Extrapolation involving comparison of solutions at different grid spacing (Richardson, 1911). The theoretical basis of the method is to assume that solutions converge asymptotically towards the exact solution as the number of elements is incremented with an apparent order of convergence that is theoretically proportional to the order of discretization scheme. The aim of the method is to estimate a 95% confidence interval that contains the exact solution. A small value of the GCI is preferred.

For three-dimensional calculations, a representative grid size h is calculated using the following expression:

$$h = \left[\frac{1}{N} \sum_{i=1}^N \Delta V_i \right]^{\frac{1}{3}} \quad (3.1)$$

where ΔV_i is the volume of the i th cell and N is the total number of cells in the simulation. The grid refinement factor is $r = h_{coarse}/h_{fine}$. Considering three different meshes (coarse - 3, medium - 2, fine - 1), the GCI for the finest mesh is calculated by using equations (3.2)-(3.7).

$$p = \left[\frac{1}{\ln(r_{21})} \right] \left[\ln \left| \frac{\varphi_3 - \varphi_2}{\varphi_2 - \varphi_1} \right| + q(p) \right] \quad (3.2)$$

$$q(p) = \ln \left(\frac{r_{21}^p - s}{r_{32}^p - s} \right) \quad (3.3)$$

$$s = 1 \cdot \text{sign} \left(\frac{\varphi_3 - \varphi_2}{\varphi_2 - \varphi_1} \right) \quad (3.4)$$

$$\varphi_{\text{ext}}^{21} = \frac{r_{21}^p \varphi_1 - \varphi_2}{r_{21}^p - 1} \quad (3.5)$$

$$e_a^{21} = \left| \frac{\varphi_1 - \varphi_2}{\varphi_1} \right| \quad (3.6)$$

$$\text{GCI}_{21} = \frac{1.25 e_a^{21}}{r_{21}^p - 1} \quad (3.7)$$

In the above equations, p is the apparent order of convergence and it is calculated with an iterative procedure (see APPENDIX A. APPARENT ORDER CALCULATION), φ is a variable of interest found with gradually refined mesh, $\varphi_{\text{ext}}^{21}$ is the extrapolated value of the variable of interest and e_a^{21} is the approximate relative error.

Although the GCI method is more popular in CFD, it has been suggested for finite element applications in solid mechanics (Kwaśniewski, 2013; Schwer, 2008). For unsteady problems, where the temporal domain must also be discretized, the GCI method can be utilized for selecting an appropriate time step Δt (Roache, 1998).

3.2.2. Turbulence Model Study

The capability of the CFD software to accurately predict the pressure drop in narrow ducts is fundamental for this study. Thus, to select a turbulence model for the multiphysics analysis, a reduced computational domain was created considering two-equal coolant channels and one plate centered (Figure 3.3). In the figure, the “gray area”

is the position where the fuel plate is located but in the fluid model, it is an empty region. The geometric parameters of this domain are equal to those listed in Table 3.1 for Case 1. The fluid was water at room temperature and its properties are given in Table 3.4.

In order to determine the most suitable turbulence model for this type of problem, the following criteria were used:

- 1- The precision of the CFD model pressure drop solution when compared with an analytical solution.
- 2- The precision of the CFD model wall shear stress solution in the region of the channels when compared with an analytical solution.

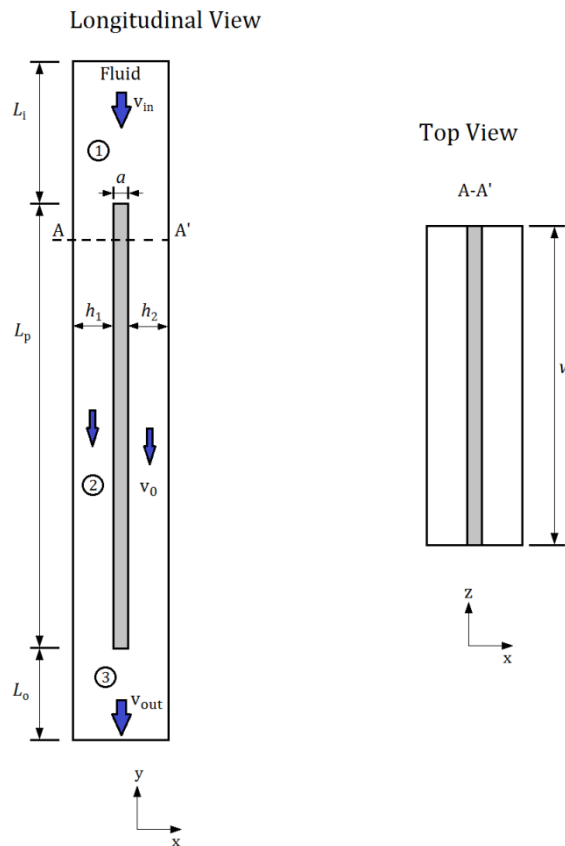


Figure 3.3. The domain used in the selection of the turbulence model.

To analytically estimate the pressure drop along the simplified domain, it can be divided into three regions: inlet plenum (1), coolant channels (2), and outlet plenum (3). It is possible to calculate the pressure drop by accounting the pressure drop from flow contraction into the channels and flow expansion from the channels (minor losses), and due to frictional losses (major losses):

$$\Delta P = P_{\text{in}} - P_{\text{out}} = \sum \Delta P_{\text{minor}} + \sum \Delta P_{\text{major}} \quad (3.8)$$

Assuming that the gravitational effects are insignificant, the pressure loss from inlet plenum to exit plenum through the coolant channel can be calculated by the expression:

$$\Delta P = f_i \frac{\rho v_{\text{in}}^2}{2} \left(\frac{L_i}{D_i} \right) + \frac{\rho v_0^2}{2} \left(K_C + K_E + f_{\text{ch}} \frac{L_p}{D_{\text{ch}}} \right) + f_o \frac{\rho v_{\text{out}}^2}{2} \left(\frac{L_o}{D_o} \right) \quad (3.9)$$

$$v_{\text{in}} = v_{\text{out}} = \frac{h_1 + h_2}{h_1 + h_2 + a} v_0 \quad (3.10)$$

The minor loss coefficients due to the abrupt contraction (K_C) and the abrupt expansion (K_E) are (White, 2011):

$$K_C = 0.42 \left(1 - \frac{D_{h,o}^2}{D_{h,i}^2} \right) \quad (3.11)$$

$$K_E = \left(1 - \frac{D_{h,i}^2}{D_{h,o}^2} \right)^2 \quad (3.12)$$

An image of a sudden contraction and expansion is shown in Figure 3.4. In the above equations, v_{in} is the inlet fluid velocity, v_{out} the outlet velocity, v_0 the average fluid velocity in the channels; f_i , f_{ch} and f_{out} are the Darcy friction factors in the inlet plenum, channels and outlet plenum, correspondingly; D_i , D_o and D_{ch} are the hydraulic diameters of the inlet plenum, outlet plenum and channels, respectively; $D_{h,i}$ and $D_{h,o}$ are the hydraulic diameters at inlet and outlet of the form loss junction.

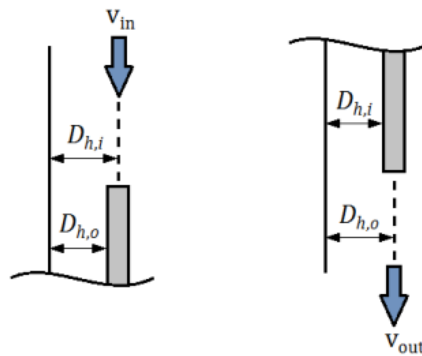


Figure 3.4. Illustration of a sudden contraction (left) and a sudden expansion (right).

To estimate the friction factor for turbulent flow ($3000 < Re$), the Colebrook formula was employed (White, 2011):

$$\frac{1}{\sqrt{f}} = -2.0 \log \left(\frac{\epsilon/D_h}{3.7} + \frac{2.51}{Re\sqrt{f}} \right) \quad (3.13)$$

where ϵ is the wall roughness and Re the Reynolds number of the region of interest.

In addition to pressure drop, an analytical solution for the wall shear stress (τ_w) is practical information for benchmarking. The next equation was used to calculate it:

$$\tau_w = \frac{1}{8} \rho f_{ch} V_0^2 \quad (3.14)$$

To solve equations (3.9)-(3.14), a simple code with Python programming language was implemented (see APPENDIX B. PRESSURE DROP ANALYTICAL MODEL). Assuming smooth walls, Table 3.2 shows the obtained values of the pressure drop and wall shear stress for two velocities of interest. These velocities were determined using equation (3.10) and considering a fluid velocity in the channels of 8 and 10 m/s, respectively.

Table 3.2. Results of the pressure drop and wall shear stress.

v_{in} (m/s)	$D_i=D_o$ (m)	D_{ch} (m)	$Re_i=Re_o$	Re_{ch}	ΔP (Pa)	τ_w (Pa)
6.27	0.01148	0.00474	80992	42605	113457	172.83
7.84			101240	53257	169386	256.88

Figure 3.5 shows the fluid geometry created for the validation case. In CFX different turbulence models are available and all are suitable for a wall function method. This study focuses primarily on two turbulence models: $k-\epsilon$ and $SST k-\omega$.

For the resolution of this particular case, steady-state calculations were conducted. The boundary conditions included a uniform inlet velocity and zero-pressure condition at the outlet. All the other surfaces were prescribed as no-slip smooth walls. Furthermore, the mesh was designed for a near wall y^+ value of approximately 60 with a fluid velocity in the channels of 8 m/s. This should yield higher y^+ values at 10 m/s. Figure 3.6 shows a view of the fluid mesh near the leading edge of the plate region. The total number of elements was 382284 with an element size of 0.1225 mm along the thickness of the channels.

Table 3.3 shows the pressure drop, the wall shear stress for each turbulence model and their percent difference from the analytical solution. Within the table, the wall y^+ value is provided, too.

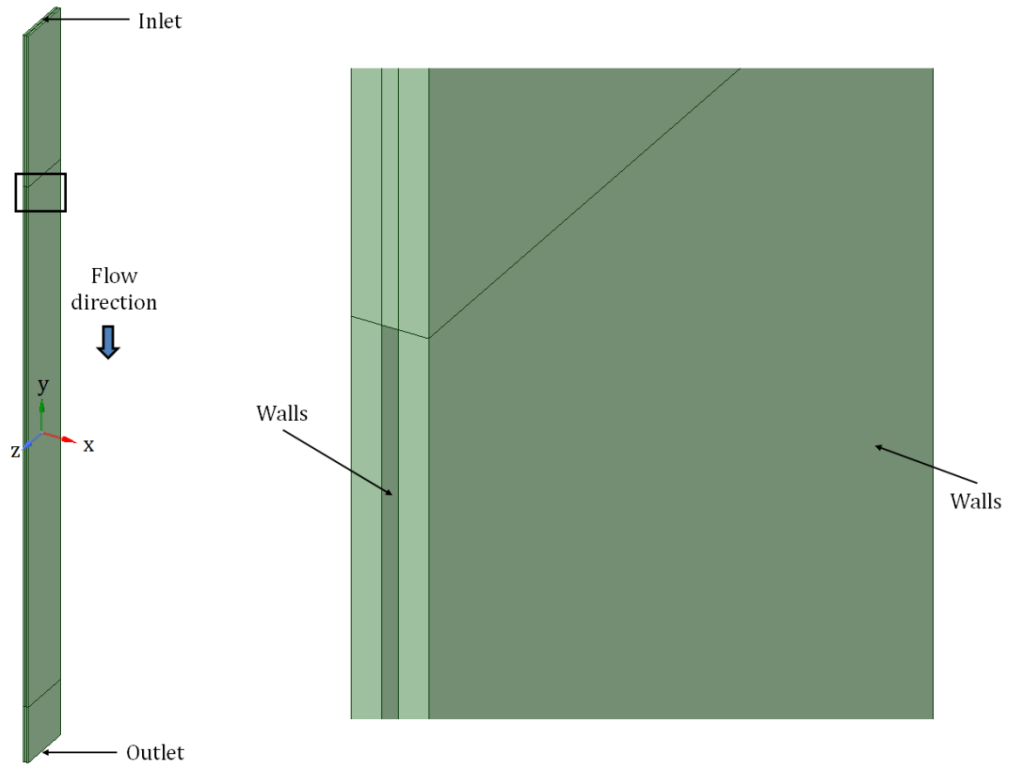


Figure 3.5. Simplified domain created in ANSYS CFX.

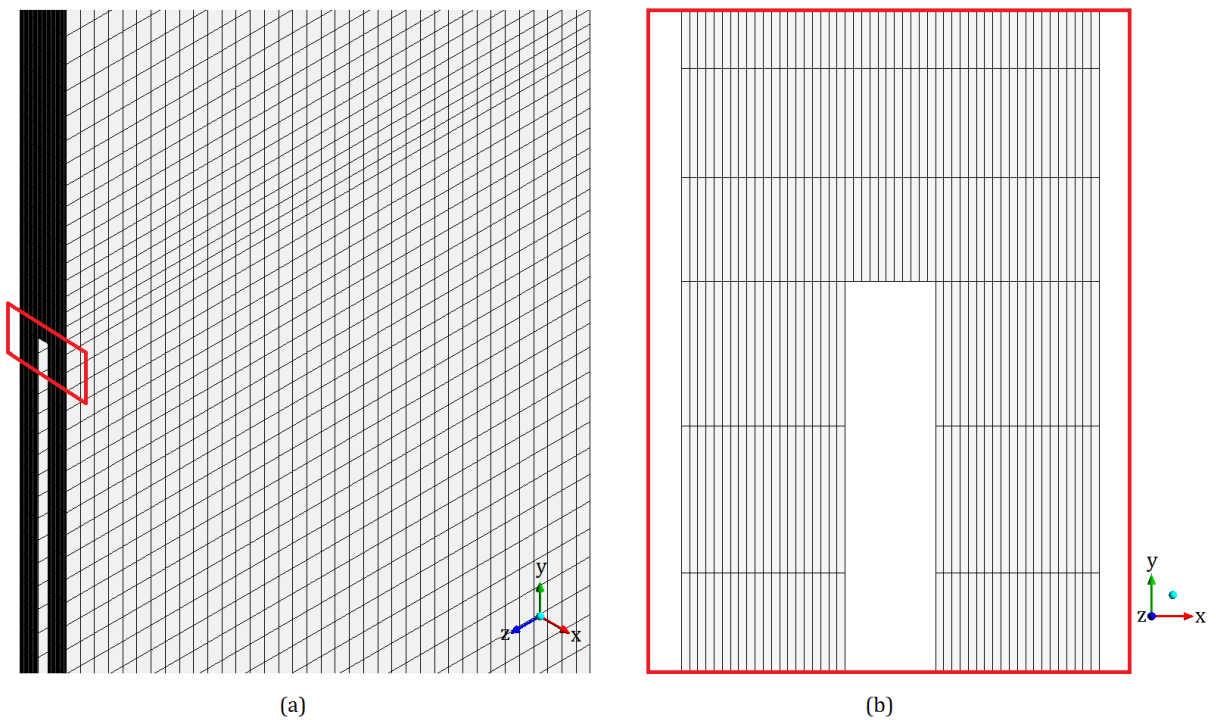


Figure 3.6. Mesh of the simplified CFD model.

Table 3.3. Results from the simplified CFD model and comparison with the analytical solutions.

Model	v_{in} (m/s)	y^+	ΔP (Pa)	Difference (%)	τ_w (Pa)	Difference (%)
$k-\varepsilon$	6.27	57	110603	2.52	173.34	0.30
	7.84	70	165055	2.56	257.9	0.40
$SST k-\omega$	6.27	57	109289	3.67	170.63	1.27
	7.84	69	162333	4.16	252.5	1.71

With the results from Table 3.3, column graphs were created. As can be observed from Figure 3.7, both turbulence models provided results close to the analytical result. However, the $k-\varepsilon$ model gave better predictions than the $SST k-\omega$ model. This result can be explained in terms of the turbulence model itself and the near-wall treatment approach it is coupled with. Generally, the $k-\varepsilon$ model works better when the wall-adjacent cells are in the log-law region and the $k-\omega$ models perform better when the cells are resolved in the viscous sublayer. In view of the results of the turbulence model study, the $k-\varepsilon$ model was selected for the successive analyses.

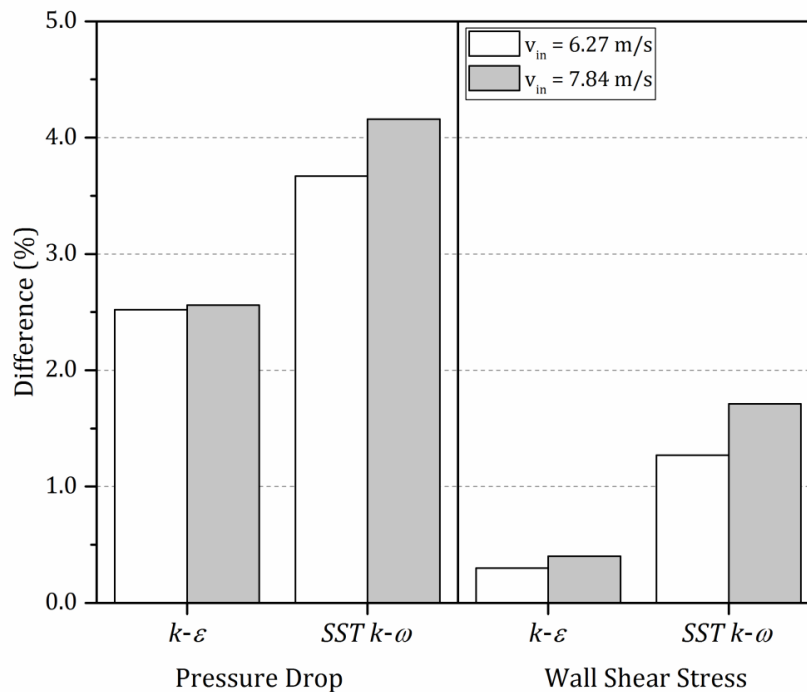


Figure 3.7. Deviation of the numerical solution from the analytical results.

3.2.3. Fluid Model Verification

In all five cases of interest, the fluid around the plates was water with constant physical properties (see Table 3.4). The fluid domain was partitioned into different volumes allowing the creation of hexahedral mesh with finer grid near-wall regions. In an effort to capture the contraction/expansion effects at the leading/trailing edges of the plates, a bias factor 4:1 was set up for spacing the cells along the inlet, outlet, and channel lengths. The same bias factor¹ was adopted for the elements along the thickness of the channels. For the grid verification study, steady-state analyses with three progressively refined structured hexahedral meshes were carried out.

Table 3.4. Water properties for given temperatures.

Property	Value	
	24 °C	50 °C
Dynamic viscosity, μ (Pa·s)	8.87×10^{-4}	5.47×10^{-4}
Density, ρ (kg/m ³)	997.56	988

The fluid surfaces in contact with the plates were assumed no-slip rigid walls, with a roughness height (arithmetic average) of 0.1 μm and equivalent sand-grain roughness height of 0.5863 μm (Adams et al., 2012). The same condition was considered at the walls parallel to the plates and in the flow direction; this condition is used to simulate the surfaces of adjacent plates enclosing the lateral coolant channels. The no-slip rigid wall boundary condition was imposed at the outer surfaces of the domain and they were treated as smooth surfaces, except those modeling neighboring plates. In the case with the support comb, the surfaces of the comb in contact with the fluid were set as no-slip smooth walls. To numerically solve the unsteady turbulent flow, the standard $k-\epsilon$ turbulence model with scalable wall functions was adopted. At the entrance, 5% of turbulence intensity was assumed.

For this analysis, at the inlet of the fluid domain, a uniform fluid velocity was assumed and was calculated by considering an inlet volumetric flow rate (Q_{in}) of 15.3 m³/h. This rate of fluid flow was determined with a fluid velocity of 8.2 m/s in the channels, which is the minimum coolant velocity required in an RMB’s fuel assembly

¹ Bias factor: ratio of the longest division and the shortest division in the mesh.

(INVAP, 2013). At the outlet, a zero-gauge pressure condition was set. The volumetric flow rates, velocities and Reynolds numbers for all cases are listed in the following table.

Table 3.5. Volumetric flow rates, velocities, and Reynolds numbers.

Case	Q_{in} (m ³ /h)	v_{in} (m/s)	Re_{in}
1		6	118696
2		6.21	119198
3	15.3	6.08	118810
4		6	190826
5		6	118696

In each case, a mesh sensitivity study according to ASME CFD best practice guidelines was performed to assess the numerical uncertainty (ASME, 2009). This mesh study was completed by varying the number of elements in the three directions. The maximum pressure (P_{max}) and wall shear stress on the surfaces of one plate, and the pressure drop (ΔP_{cch}) through the central channel were elected as the key parameters. In the case with different channels, the maximum pressure and the wall shear stress were obtained from the plate located between different channels.

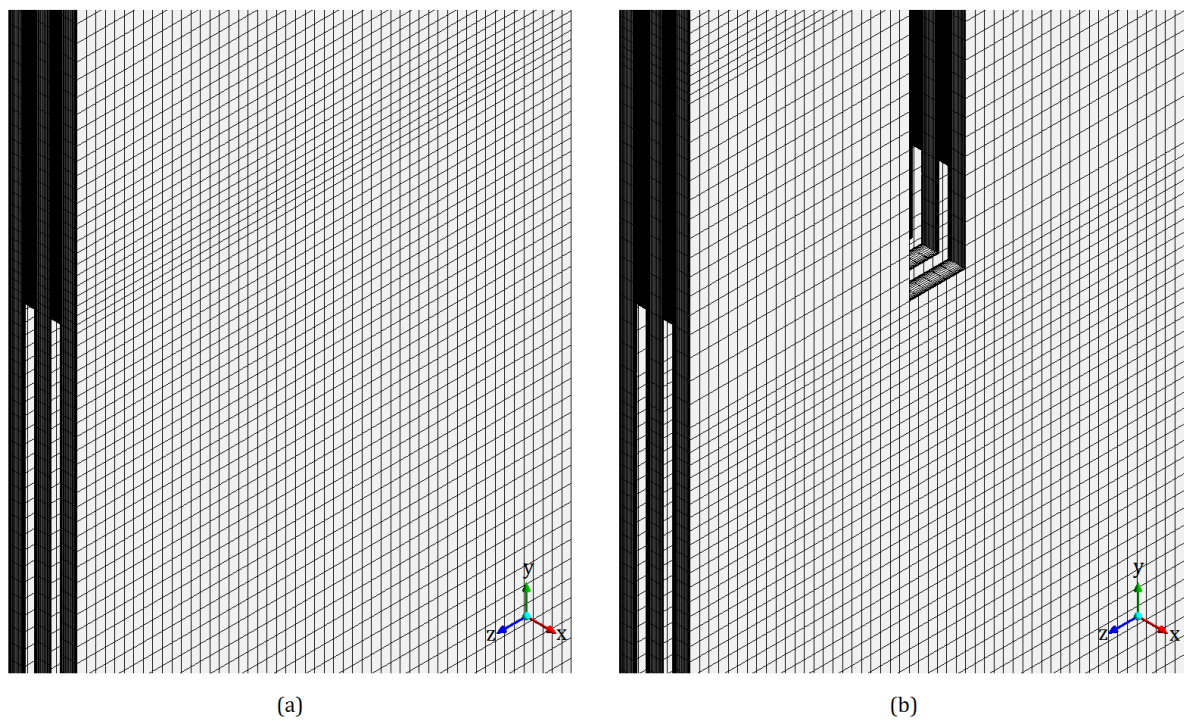


Figure 3.8. Examples of the mesh utilized in the verification of the fluid model: (a) model without and (b) with support comb.

Figure 3.8 shows examples of the mesh utilized in the verification of the fluid model. Details of the three meshes for each case are presented in Table 3.6, where the finest mesh is identified as Mesh 1. Table 3.7 shows the results obtained by applying the ASME guidelines. In all cases, all three meshes presented a well-behaved convergence. The predicted uncertainty of the three metrics studied can be considered a reliable approximation of the correct solution.

Based on the results presented in Table 3.6 and Table 3.7, it can be concluded that, in each case, Mesh 1 is sufficient for the multiphysics simulations as the numerical uncertainties of the key parameters were lower than 2%.

Table 3.6. Characteristics of the meshes used in the verification of the fluid models and values of the key parameters.

Case	Mesh	Elements	h (mm)	r	ΔP_{cch} (Pa)	P_{max} (Pa)	τ_w (Pa)
1	1	1040000	0.7955	1.1436	121194	125272	182.58
	2	695600	0.9097	1.2462	119961	124987	182.28
	3	359381	1.1337	-	115803	120572	183.27
2	1	1040000	0.7852	1.1435	132156	140550	198.44
	2	695600	0.8979	1.2462	133196	140206	198.08
	3	359381	1.1190	-	137697	135429	199.16
3	1	1057160	0.7876	1.1173	123073	130014	184.21
	2	757796	0.8800	1.2723	123668	129725	183.90
	3	368002	1.1196	-	128292	125062	184.88
4	1	1040000	0.7955	1.1436	110097	113869	163.03
	2	695600	0.9097	1.2462	108908	113574	162.66
	3	359381	1.1337	-	104897	109245	163.61
5	1	1035584	0.7952	1.1239	120358	117543	184.91
	2	729312	0.8937	1.2431	121630	117287	184.61
	3	379269	1.1110	-	127042	113062	185.83

Table 3.7. Uncertainty quantification of the CFD model.

Case	Parameter	$\varphi_{\text{ext}}^{21}$ (Pa)	e_a^{21} (%)	GCI_{21} (%)
1	ΔP_{cch}	122955	1.02	1.82
	P_{max}	125346	0.23	0.07
	τ_w	182.82	0.16	0.17
2	ΔP_{cch}	131145	0.79	0.96
	P_{max}	140648	0.24	0.09
	τ_w	198.76	0.18	0.20
3	ΔP_{cch}	122541	0.48	0.54
	P_{max}	130148	0.22	0.13
	τ_w	184.57	0.17	0.24
4	ΔP_{cch}	111794	1.08	1.93
	P_{max}	113949	0.26	0.09
	τ_w	163.43	0.23	0.31
5	ΔP_{cch}	118642	1.06	1.78
	P_{max}	117627	0.22	0.09
	τ_w	185.14	0.16	0.15

3.2.4. Solid Model Verification

The fuel meat of the plates studied here consists of a fuel powder dispersed in an aluminum matrix and clad with this same material. Hence, the plate material considered is aluminum alloy 6061-T6. The material of the comb was assumed to be the same. The Al-6061-T6 properties for different temperatures are reported in Table 3.8.

Table 3.8. Aluminum alloy 6061-T6 properties for given temperatures (ASM International, 1990).

Property	Value	
	24 °C	120 °C
Density, ρ_m (kg/m ³)	2700	
Poisson's ratio, ν	0.33	
Young's modulus, E (GPa)	68.9	64.9
Yield strength, σ_y (MPa)	276	246.5

For the verification of the solid model, three different meshes were generated and static analyses were performed using the Static Structural module of ANSYS Mechanical. The plates and the inlet support comb were discretized using a structured mesh with hexahedral elements SOLID186. This is a higher-order 3-D solid element that exhibits a quadratic displacement behavior. It is defined by 20 nodes having three degrees of freedom per node and it supports plasticity, large deflection, and large strain capabilities (ANSYS Inc., 2017b). Along the surfaces parallel to flow, a 2.25 mm region of the width of each plate was used to clamp them. The applied boundary condition on front and back regions were displacements in $x = y = z = 0$. The trailing edge of each plate was free. The plasticity material model (Bilinear Isotropic Hardening) with zero Tangent Modulus was considered.

In the cases without support comb, one plate was examined and a uniform pressure load (P) was applied over one of its long surfaces. This pressure loading is equal to the maximum pressure found in subsection 3.2.3 for each case with Mesh 1. It was imposed to simulate the hydraulically induced load that the plates are exposed to when coupled with the fluid domain. The plate model is depicted in Figure 3.9.

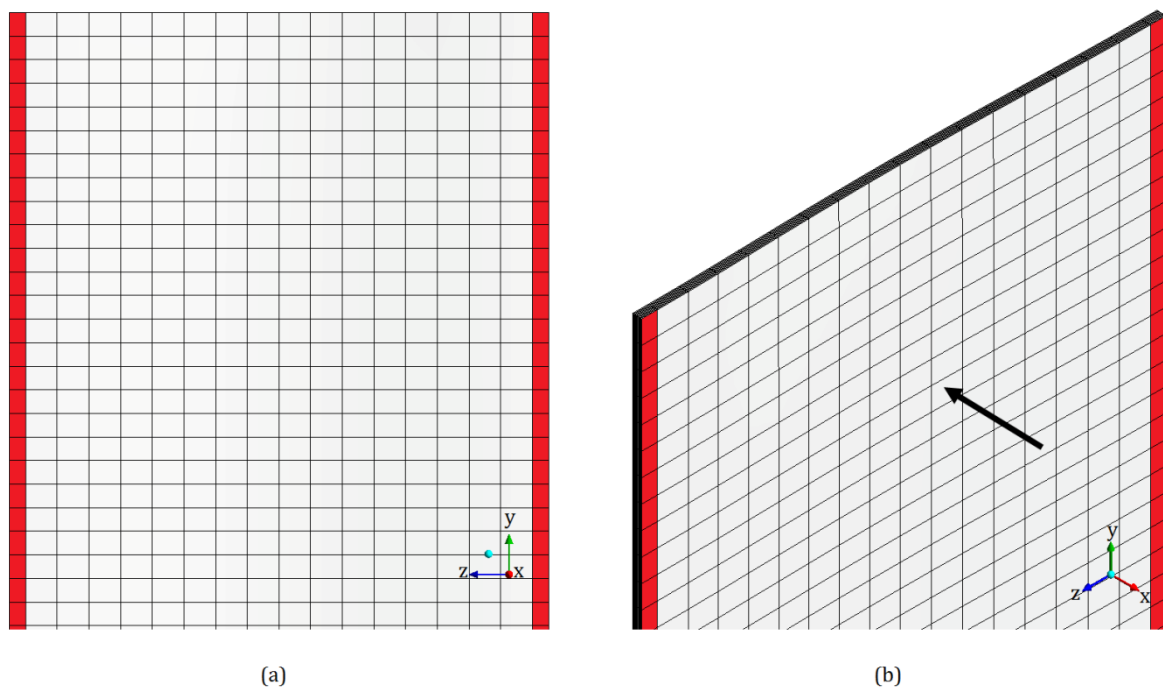


Figure 3.9. Example of the mesh utilized in the verification of the solid model without the support comb. The red surfaces are the regions used to fix the plates. The arrow indicates the direction of application of the pressure load.

In the domain with the support comb, the aforementioned process was also followed, but both plates were tested. In addition, the surfaces of the comb and plates that are in contact were modeled as Frictionless Contacts; the CONTA174 elements were utilized. This element type represents contact and sliding between 3-D target surfaces and a deformable surface (ANSYS Inc., 2017b). The solid model including the support comb is shown in Figure 3.10. Twenty-two elements along the thickness of each plate were set to capture their flexural behavior with a high degree of accuracy.

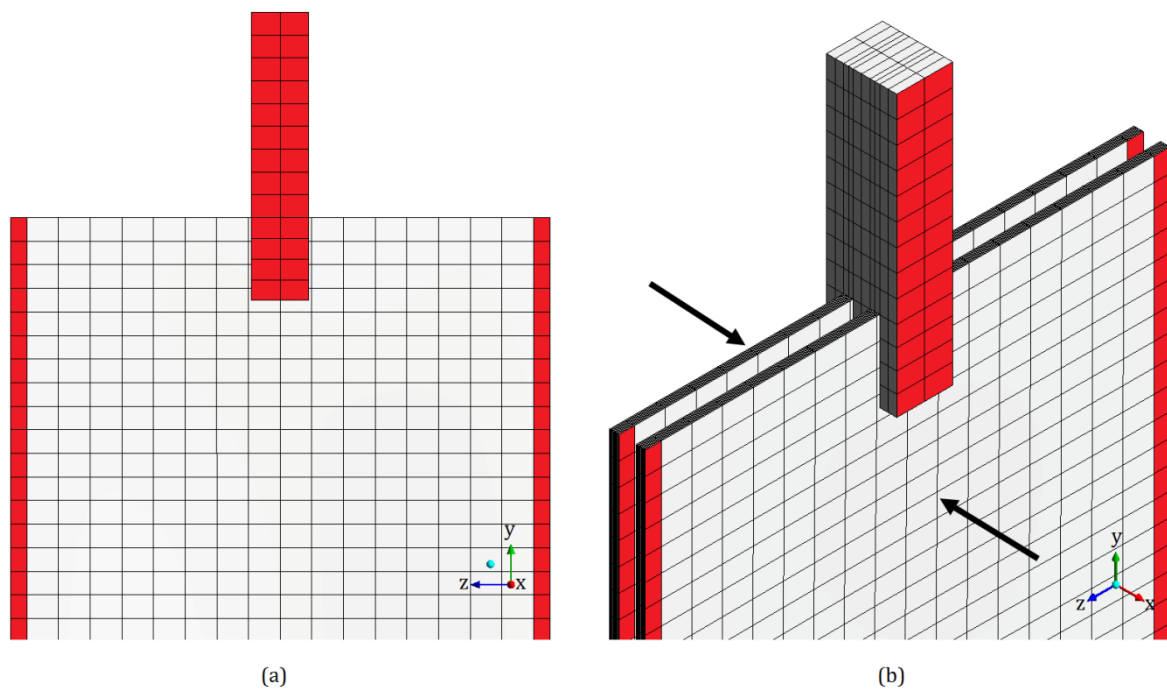


Figure 3.10. Example of the mesh utilized in the verification of the solid model with the support comb. The red surfaces are the regions used to fix the plates and the comb. The arrow indicates the direction of application of the pressure load.

Although the GCI method was initially proposed for CFD and heat transfer calculations, it has also been recommended for finite element applications in structural and solid mechanics (Kwaśniewski, 2013). The deflection at the midpoint (δ_m) of the plates was chosen as the main parameter for the GCI calculation. Table 3.9 shows the characteristic of the studied meshes and the values of this key variable. Again, Mesh 1 identified the finest mesh.

Table 3.10 presents the uncertainty quantification of the structural model. It can be observed that, in all cases, the uncertainty from the most refined mesh was lower than 0.5%. Therefore, in each case, Mesh 1 is chosen to be employed in the FSI calculations.

Table 3.9. Characteristics of the meshes used in the verification of the solid models and values of the key parameter.

Case	P (Pa)	Mesh	Elements	h (mm)	r	δ_m (mm)
1	125272	1	149600	0.7625	1.2489	0.4783
		2	76800	0.9523	1.2470	0.4776
		3	39600	1.1875	-	0.4768
2	140550	1	149600	0.7587	1.2488	0.5454
		2	76800	0.9475	1.2470	0.5449
		3	39600	1.1816	-	0.5439
3	130014	1	149600	0.7625	1.2489	0.5113
		2	76800	0.9523	1.2470	0.5107
		3	39600	1.1875	-	0.5098
4	113869	1	149600	0.7625	1.2489	0.4638
		2	76800	0.9523	1.2470	0.4633
		3	39600	1.1875	-	0.4624
5	117543	1	299656	0.7677	1.2487	0.4526
		2	153942	0.9586	1.2468	0.4521
		3	79428	1.1952	-	0.4513

Table 3.10. Uncertainty quantification of the solid model.

Case	Parameter	ϕ_{ext}^{21} (mm)	e_a^{21} (%)	GCI_{21} (%)
1	δ_m	0.4829	0.15	0.30
2		0.5459	0.09	0.11
3		0.5125	0.12	0.29
4		0.4644	0.11	0.16
5		0.4534	0.11	0.23

3.2.5. Validation Study

In order to validate the FSI simulations for use in the analysis of fuel assemblies, a single plate test section designed by Kennedy (2015) was modeled. Kennedy conducted a

set of experiments utilizing a flat plate, made from Aluminum Alloy 6061-T6, and located between two fluid channels with unequal thicknesses, 2.5420 mm and 2.032 mm. The wetted plate width is 110.287 mm, thickness (a) is 1.016 mm, plate length (L_p) is 647.7 mm, inlet plenum length (L_i) is 190.5 mm and outlet plenum length (L_o) is 76.2 mm. Along either long surface of the plate, a width of 12.7 mm was used for clamping it. The outer walls of the test section were constructed of Plexiglas panels. Figure 3.11(a) illustrates a drawing of the experiment test section and Figure 3.11(b) shows a transparent view of the fluid-solid model. The materials properties are given in prior subsections.

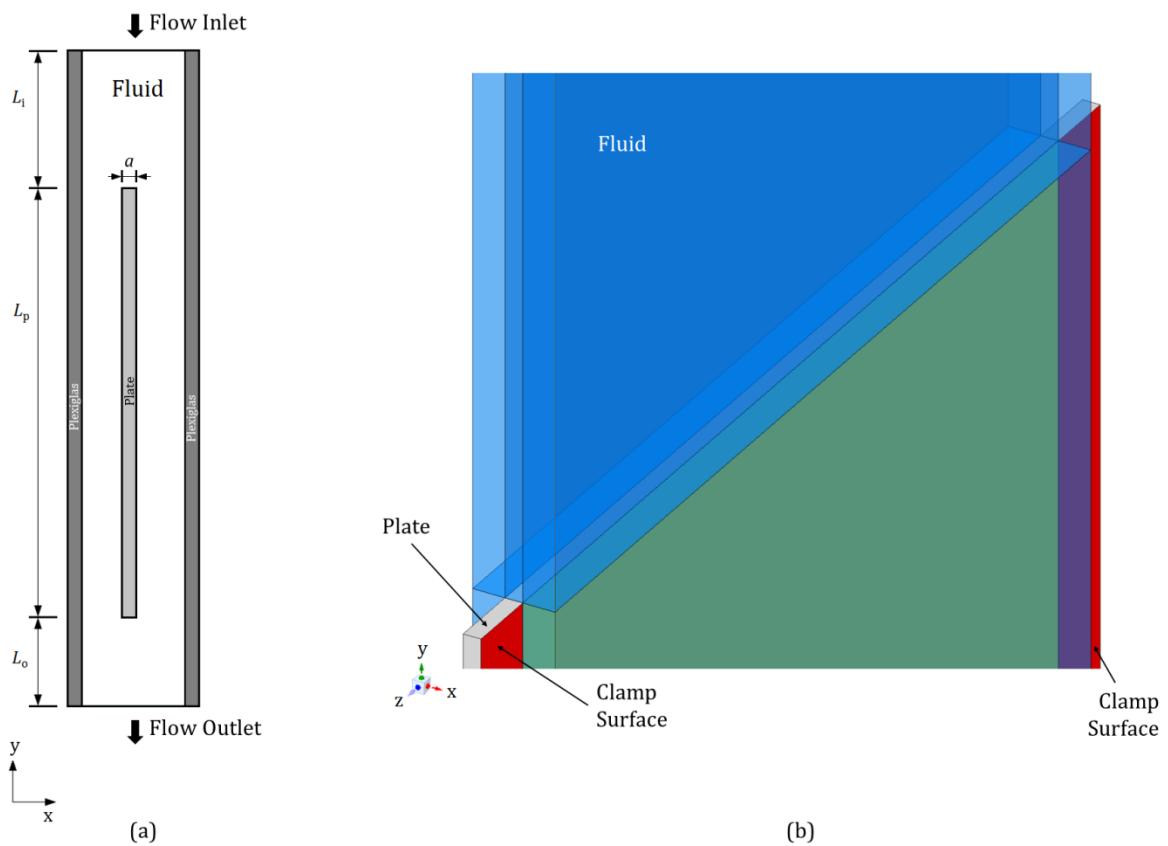


Figure 3.11. (a) Schematic representation of Kennedy's one-plate experiment and (b) FSI model.

To make the comparison, one case with an inlet flow rate of 2.6 kg/s was analyzed. A hexahedral mesh with 607200 elements for the fluid domain and 108120 elements for the solid domain was used. Most of the simulation conditions described in the earlier sections were considered here. All the surfaces of this fluid domain were defined as no-slip smooth walls.

Kennedy provided average deflection points of the plate at different axial locations, measured with two laser displacement sensors. Figure 3.12 depicts the deflection comparison between the experimental result and the numerical model. In the figure, the error bars indicate the 95% confidence interval. As can be observed, the leading and trailing edge deflections calculated with the fluid-solid model showed a good agreement with the experiment. However, for the inner points, the deflections differ. This discrepancy is a result of imperfections on the plate surfaces, which were discussed by Kennedy but not assumed in this FSI model. Nevertheless, the validation study allowed proof of the modeling approach and the capability of the computational tools to predict the plate deflections.

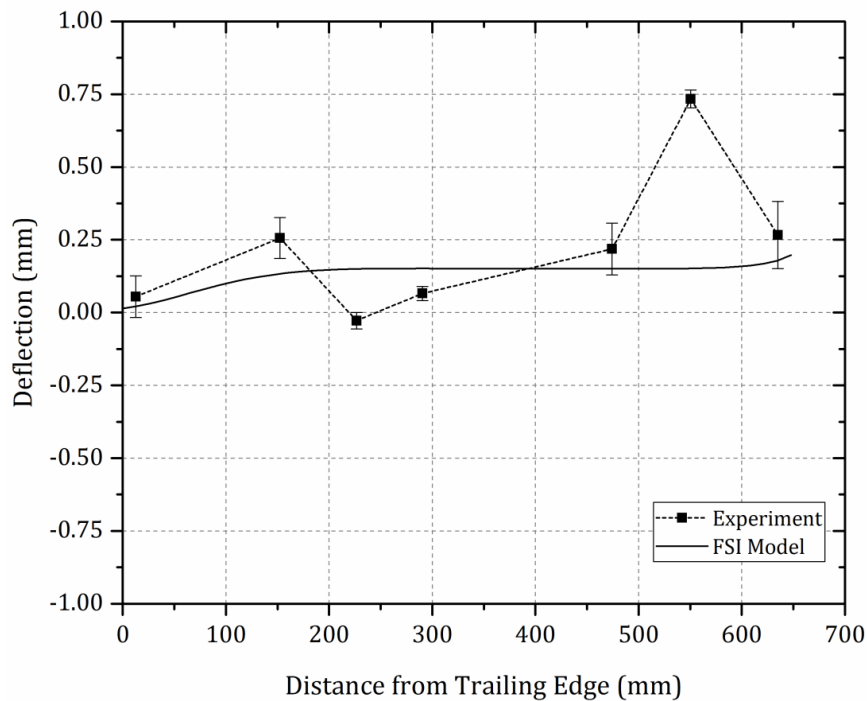


Figure 3.12. Comparison of the numerical result with the experimental data.

3.3. Multiphysics Models

As previously mentioned, the computational domain considered in the FSI model is composed of two fuel plates and each one of them is surrounded by two coolant channels. This configuration is here analyzed to include the cross-sectional coupling between neighboring plates and, simultaneously, to keep the computational cost of the multiphysics analysis limited. For these reasons, even though this system is a simplified

representation of a complete fuel element, it is an important case from the numerical perspective and provides conclusions applicable to a multiple-plate assembly.

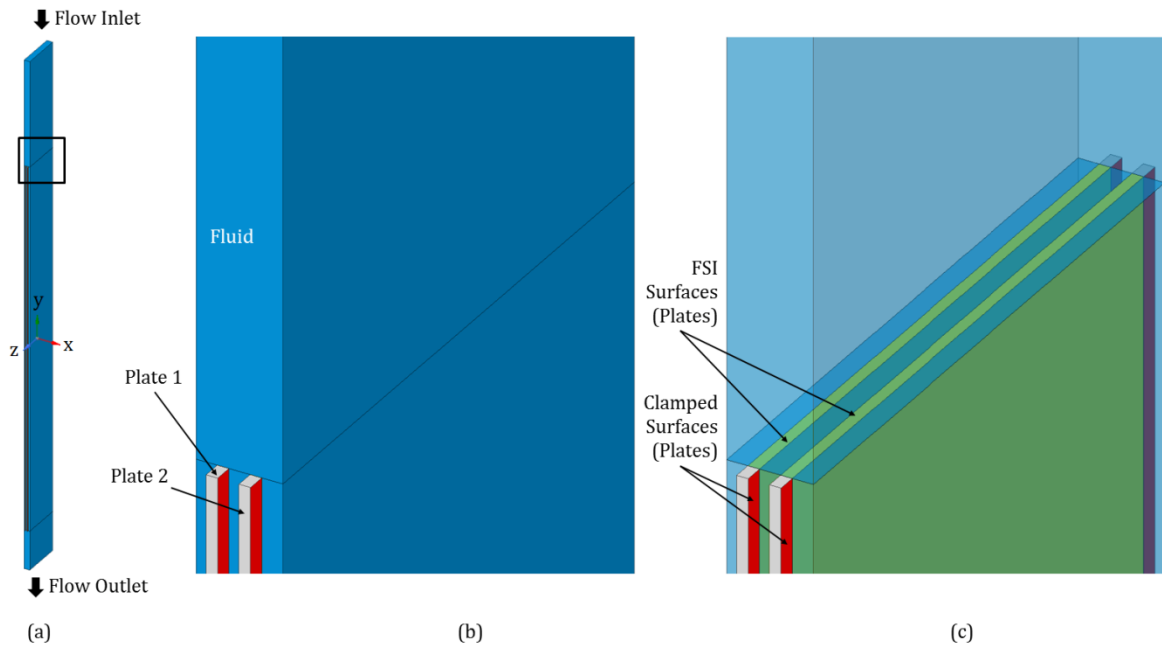


Figure 3.13. Fluid-solid model without the inlet comb (cases 1 to 4).

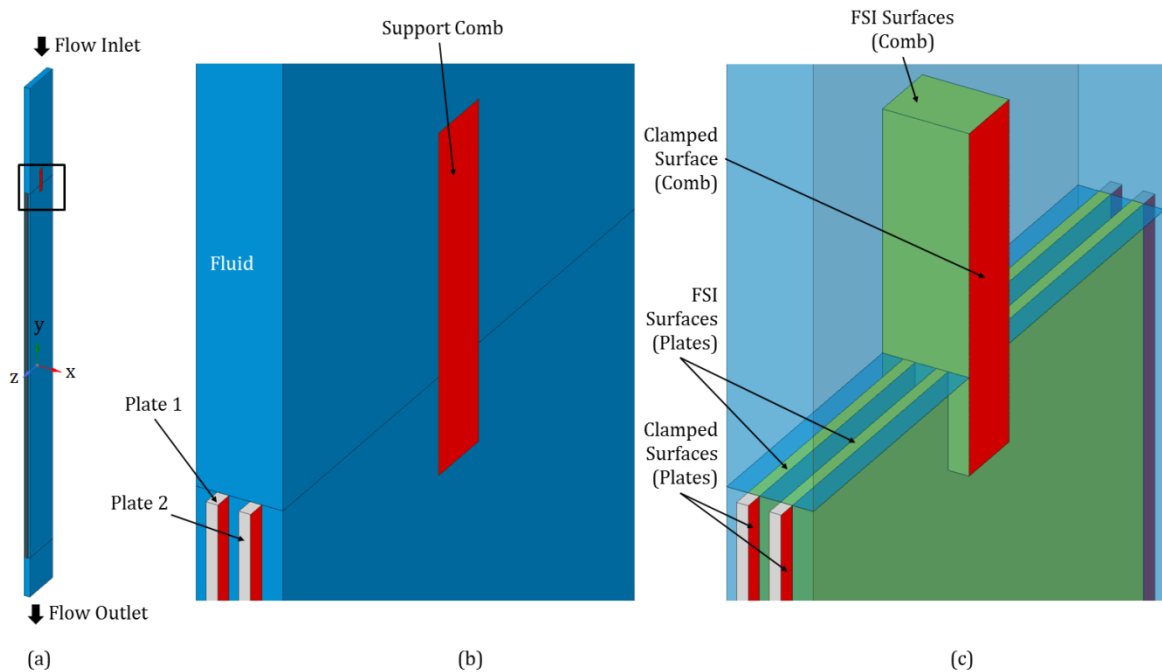


Figure 3.14. Fluid-solid model with the inlet comb (Case 5).

Earlier subsections detail the process for obtaining precise solutions of the fluid and solid domains individually. The next step was to couple these two models to

understand how the coolant flow interacts with the fuel plates. Figure 3.13 and Figure 3.14 illustrate the combined plate and fluid fields. In both figures, a transparent view of the domain has been included, where it is possible to observe the surfaces of the solid part in contact with the fluid flow. The red surfaces identify the regions used to fix the plates and the comb.

The mesh density and the turbulence model were designated based on the studies outlined in subsections 3.2.3 and 3.2.4. In Table 3.11, some adopted parameters in the settings of the FSI model are listed. More details on the FSI model configuration can be found in APPENDIX C. SETTINGS OF THE FSI ANALYSIS.

Table 3.11. Settings of the fluid-structure interaction analyses.

Number of elements	Case 1 – Fluid: 1040000, Solid: 299200 Case 2 – Fluid: 1040000, Solid: 299200 Case 3 – Fluid: 1057160, Solid: 299200 Case 4 – Fluid: 1040000, Solid: 299200 Case 5 – Fluid: 1035584, Solid: 299656
Analysis	CFX: ANSYS MultiField Coupling Mechanical: Transient Structural, large deformations were enabled
Turbulence model	k - ϵ with Scalable Wall Function
Convergence criteria	RMS residuals of all conservation equations $< 10^{-4}$ Imbalances of mass and momentum $< 1\%$ Global variables do not change over iterations Mesh displacement residual target $< 10^{-4}$
Transient scheme	Second Order Backward Euler
Coupling scheme	Explicit
Coupling data transfer	Under relaxation factor = 0.75 Convergence target = 0.01
Solution Sequence	Solve Mechanical fields before CFX fields

For the multiphysics models, fluid-solid interface boundary conditions were assumed on the surfaces of the plates and comb in contact with the fluid. These are the surfaces where forces from the CFD model are applied to the structure. In the fluid part,

mesh motion of all fluid surfaces in contact with the structure was allowed. Finally, in each case, the other conditions defined in past subsections were preserved.

3.3.1. Temporal Discretization

The time step size dictates how far the solution progresses before the codes update the boundary conditions. A larger Δt allows the solution to progress further in each step, thereby reducing the number of data exchanges and increasing the speed of the overall simulation. However, the solution could begin to diverge as the structure may move too far with a given pressure field. In contrast, for a small Δt , the simulation will take an extremely long time to be completed or the solvers may begin to detect higher frequencies in plate deflections, rather than the static deflections which are of primary interest. As a consequence, this can lead to the divergence of the solution, which is generally referred to as the added mass problem (Causin et al., 2005).

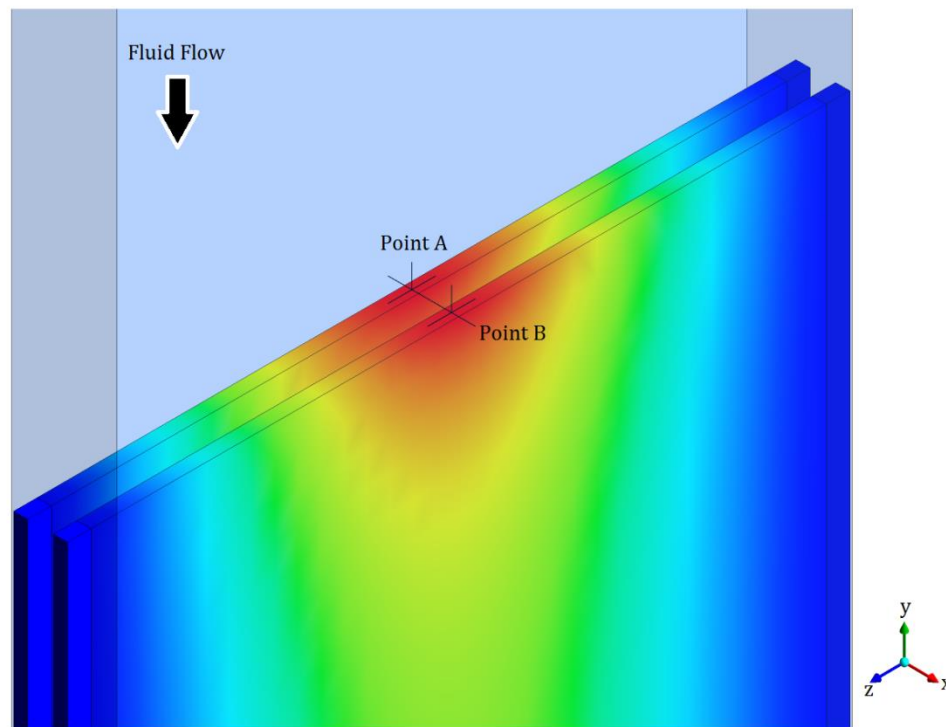


Figure 3.15. Location of Points A and B to observe the evolution of deflection of the plates.

The FSI effect requires both the fluid and the solid analysis to be transient. Hence, in order to balance computational efficiency and stability, it is important to determine a suitable time step size. A study on the impacts of the time step size in the FSI simulations was carried out in terms of displacement amplitudes. Using the FSI model of Case 1,

simulations were completed with an inflow velocity of 6 m/s and three different time step sizes 0.1, 0.05, and 0.025 s. In each case, the simulation time was completed with a total of 25 time steps. At the midpoint of the leading edges of the plates, monitor points (A and B) were located and the total mesh displacement was extracted. These points are shown in Figure 3.15. With Point A displacement (δ_A), the GCI method was applied for estimating the uncertainty of the finest temporal grid.

The curves in Figure 3.16 show the model convergence for three different time steps. It should be noted that, in each case, the model converged in about 13 time steps and steady-state deflection of the plates is attained from that moment.

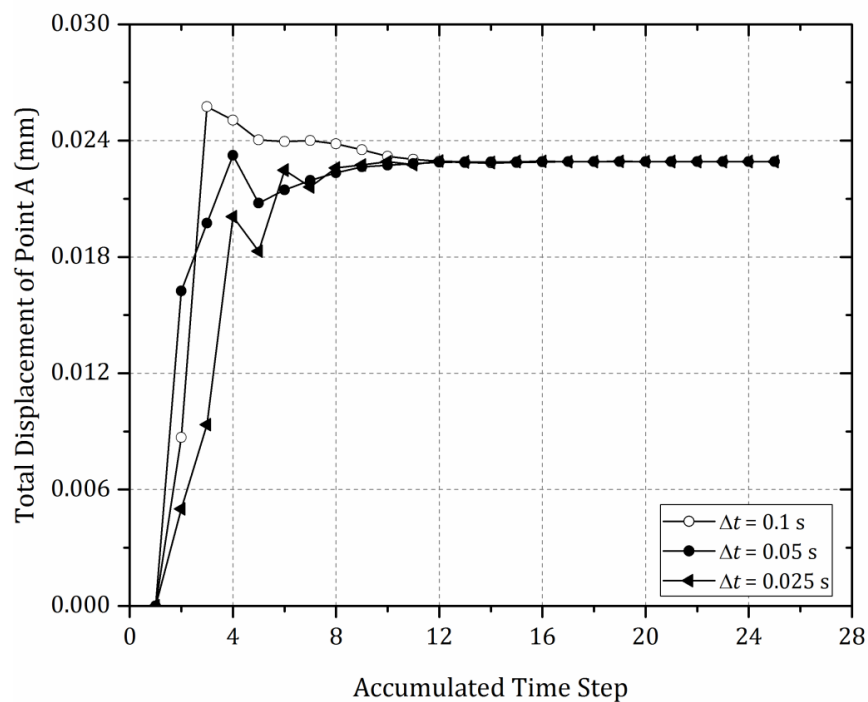


Figure 3.16. Convergence history of Point A displacement for a fluid velocity in the channels of 8.2 m/s and different time steps.

In transient FSI analysis, the time step of the fluid model must equal the FSI time step, while a smaller value can be used for the solid time step. This so-called sub-cycling is sometimes required to improve stability (Du, 2010), but the utilization of different time steps cause an increment of the calculation time. That is why in this study, the criterion for selecting an adequate time step was to consider a unique time step that ensures a good balance between computation time and solution accuracy.

Table 3.12 illustrates the GCI calculation for the three temporal grids. The numerical uncertainty of the key parameter was 0.003%. Thus, from this result, it was determined that a time step of 0.025 s is proper for all subsequent simulations.

Table 3.12. Uncertainty quantification of the temporal discretization.

Grid	Δt (s)	r	δ_A (mm)	$\varphi_{\text{ext}}^{21}$ (mm)	e_a^{21} (%)	GCI_{21} (%)
1	0.025	2	0.022924			
2	0.05	2	0.022923	0.022925	0.004	0.003
3	0.1	-	0.022926			

4. RESULTS AND DISCUSSION

In the current work, prior to conducting the FSI simulations, a set of target volumetric flow rates at the inlet was determined. Firstly, considering that 8.2 m/s is the minimum coolant velocity required in the channels of an RMB's fuel element, using its nominal dimensions and incompressible fluid, the smallest rate of fluid flow was estimated. Afterward, new volume flow rates were calculated at velocity ratios v_0/v_M from 0.6 to 1.2 with intervals of 0.05. Miller's velocity of the fuel assembly here analyzed is 16.84 m/s. It was determined taking into account nominal dimensions and materials properties at room temperature. Next, for each case, inlet velocities of the water were calculated and assumed at the inlet boundary condition. In all case, the Reynolds number was above 180000. Table 4.1 provides those targeted values.

Table 4.1. Volume flow rates and velocities used in the simulations.

Q_{in} (m ³ /h)	v_{in} (m/s)		
	<i>Cases 1, 4 & 5</i>	<i>Case 2</i>	<i>Case 3</i>
15.30	6.00	6.21	6.08
17.27	6.77	7.01	6.87
18.85	7.39	7.65	7.49
20.43	8.01	8.29	8.12
21.99	8.62	8.92	8.74
23.57	9.24	9.56	9.37
25.12	9.85	10.20	9.99
26.71	10.47	10.84	10.62
28.26	11.08	11.47	11.24
29.84	11.70	12.11	11.86
31.42	12.32	12.75	12.49
32.98	12.93	13.38	13.11
34.56	13.55	14.02	13.74
36.14	14.17	14.66	14.37
37.70	14.78	15.30	14.99

The first numerical experiment was performed and the structural response was obtained. Then, this solution was taken as an initial condition and the new analyses were carried out. Every calculation was run until the convergence criterion was reached and steady-state solutions of the fluid flow and structure variables were achieved, e.g. pressure drop, the fluid force acting on the plates, and the total displacement of the midpoint of the plates. In all simulations, the dimensionless normal distance from the wall was checked to verify if the wall distance requirements for the $k-\varepsilon$ model were satisfied. It was found that y^+ was between 30 and 100, which is in the appropriate range of using the wall function approach for the near wall treatment (ANSYS Inc., 2017a). It is important to mention that all runs were executed on an Intel Xeon dual processor E5-2640 family PC, 2.00 GHz, with 48 GB of RAM.

4.1. Results from Case 1

Line probes were created along the axial centerline of each plate and total mesh displacements were taken along these lines. With the displacements, a static deflection profile of each fuel plate was generated. Since similar profiles were observed for both plates, only the deflection profile of Plate 1 is shown in Figure 4.1. Besides that, the average fluid velocity in the coolant channels was determined.

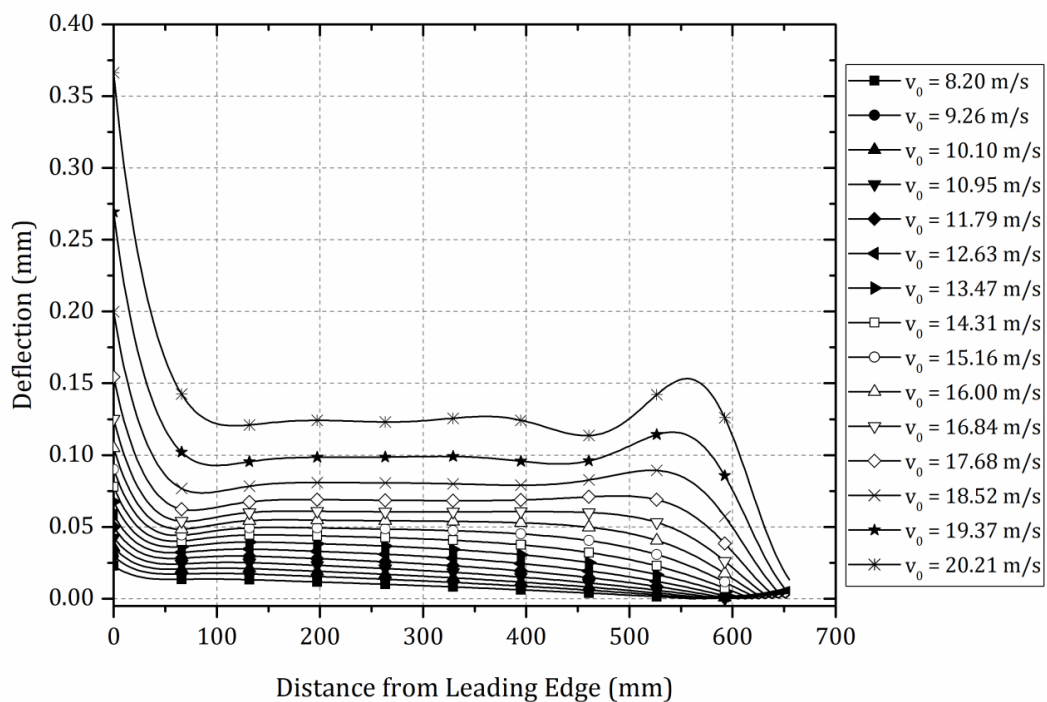


Figure 4.1. Deflection profile of Plate 1 for different fluid velocities in the channels.

As expected, with the flow rate increment, the resulting deflection of the plates also increased. As seen from Figure 4.1, the maximum deflection occurred at the leading edge of the plates. Furthermore, close to the trailing edge, a region of incremented deflection appeared with the rising of the fluid velocity. This downstream deflection is caused by fluid friction losses and redistribution of flow between channels.

From the equation of motion for a flat plate, it is known that the plate deflection is related to pressure forces acting on its surface (Weaver and Unny, 1970). In addition, the fluid-dynamic pressure over the plate is proportional to the fluid velocity squared. Thus, for evaluation purposes and to determine the critical velocity (v_c) of the subassembly, the maximum deflection of the plates and the square of the average coolant velocity in the channels were related, as it can be seen in Figure 4.2.

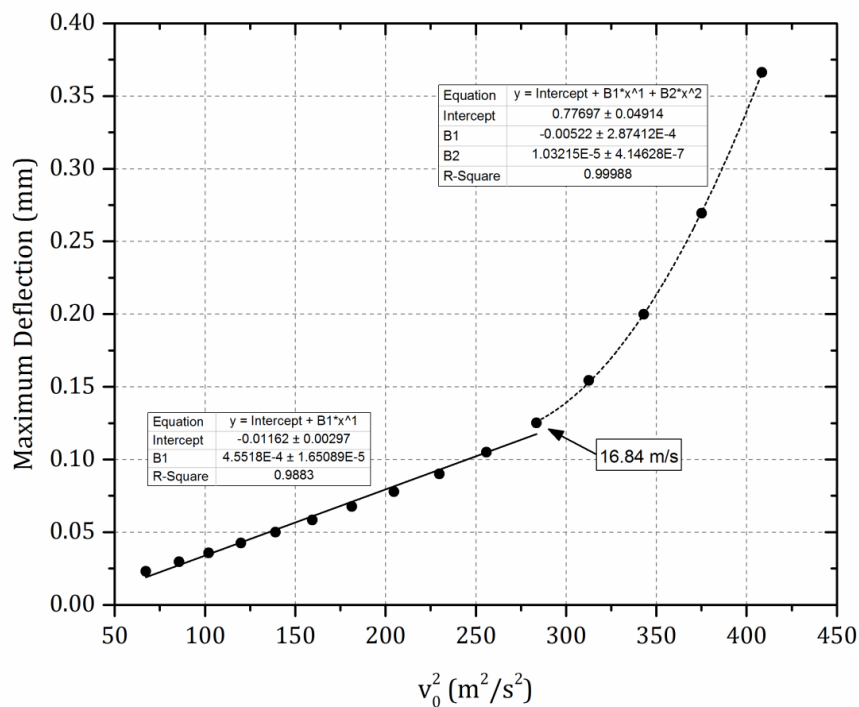


Figure 4.2. Maximum deflection of Plate 1 or 2 as a function of the square of the fluid velocity in the channels in Case 1. The arrow points out the critical fluid velocity.

In the figure above, we can note that the plotted points follow two trends. Then, two curves that fit these points were incorporated. The first curve fit was completed up to a specific velocity and it suggests that the maximum deflection of the plates is a linear function of the square of the fluid velocity in the channels. We viewed that for velocities up to that specific value, the coefficient of determination (R-square) was higher than

0.95. In contrast, for velocities above that value, it is possible to see that the deflection increases more rapidly and we fitted the deflection trend to a quadratic polynomial. So, in this case, we identified 16.84 m/s as the critical flow velocity because it is the velocity where the shape of the curve varied from a linear (R-square ≥ 0.95) to nonlinear behavior. This moment is also recognized as the beginning of the hydroelastic instability, a term defined in the INTRODUCTION. It is important to highlight the fact that, at the critical velocity, the deflections become bigger instead of an abrupt collapse of the plates.

Deflection contour plots of the plates for different fluid velocities are presented in Figure 4.3. As it was previously indicated, at $v_0 = 20.21$ m/s the model predicted an additional deflection peak near the trailing edges of the plates. This result shows that deflections also occur along the entire length of the fuel plates. In the figure, we can observe that the deflections of the adjacent plates are in opposite directions.

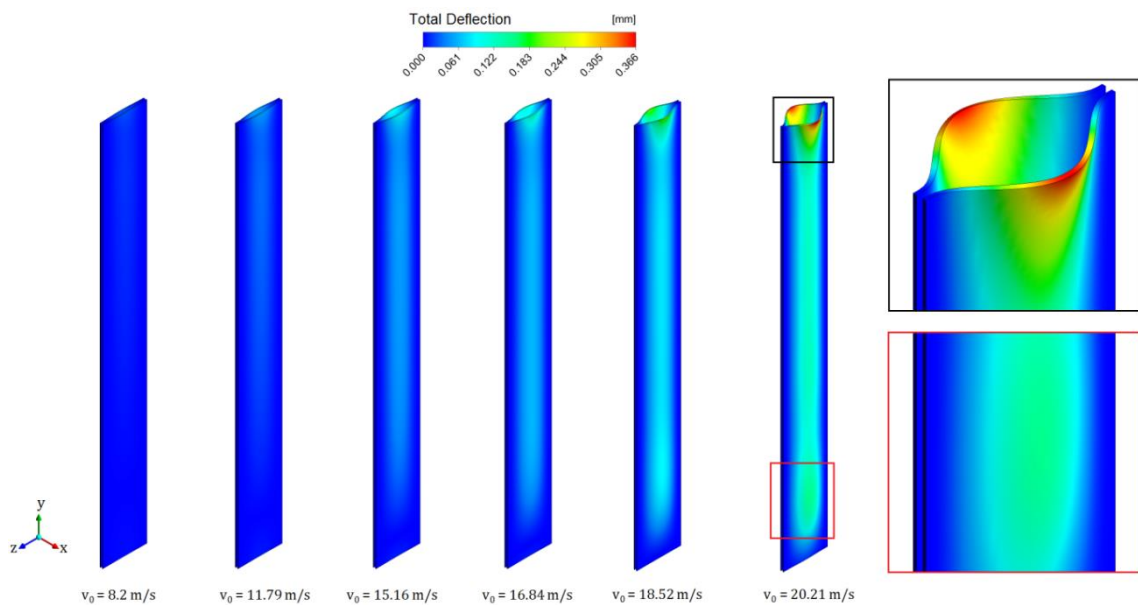


Figure 4.3. Deflection contours of the plates for different fluid velocities in the channels. Fluid flow is downward. The deflection scale factor is 0.5x.

In an actual assembly, where there are several fuel plates, some coolant channel would be constricted due to the deflections of the adjacent plates. Having this in mind, a calculation was performed to obtain the ratio by which the lateral-channel area at the upstream end was reduced due to the deflections of Plate 1 and another plate bounding that channel. Figure 4.4 presents the deformation of the leading edge; the area under the curve was computed and multiplied by two to estimate the total area change. Supposing that channel area change of 30% is too much (Johansson, 1959), it is possible to conclude

that, for fluid velocities in the channels up to 20.21 m/s (1.2 times the critical velocity), the flow-area change is below the acceptable limit (see Figure 4.5).

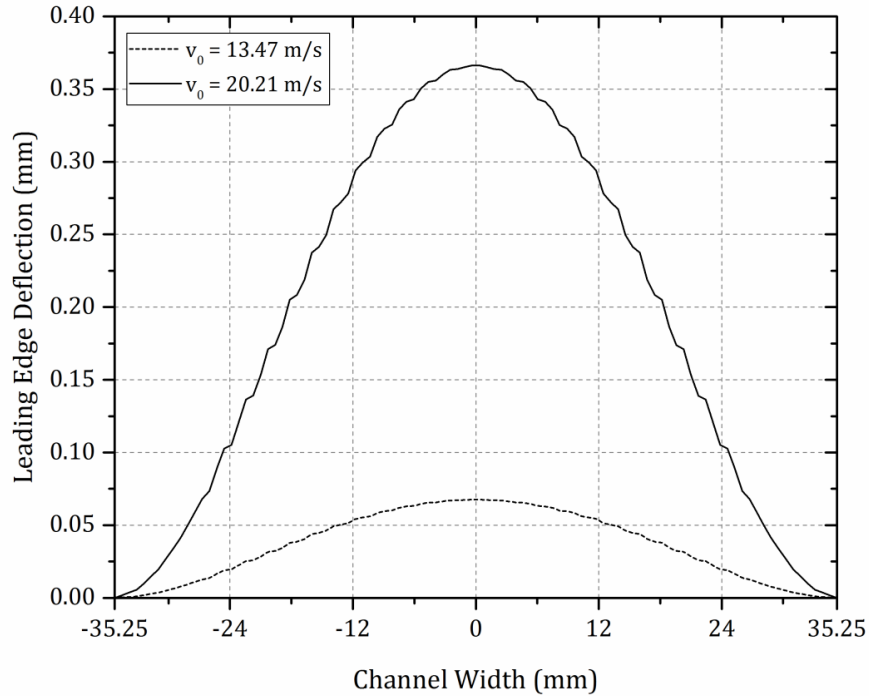


Figure 4.4. Leading edge deflection into the channel for two-different fluid velocities in the channels.

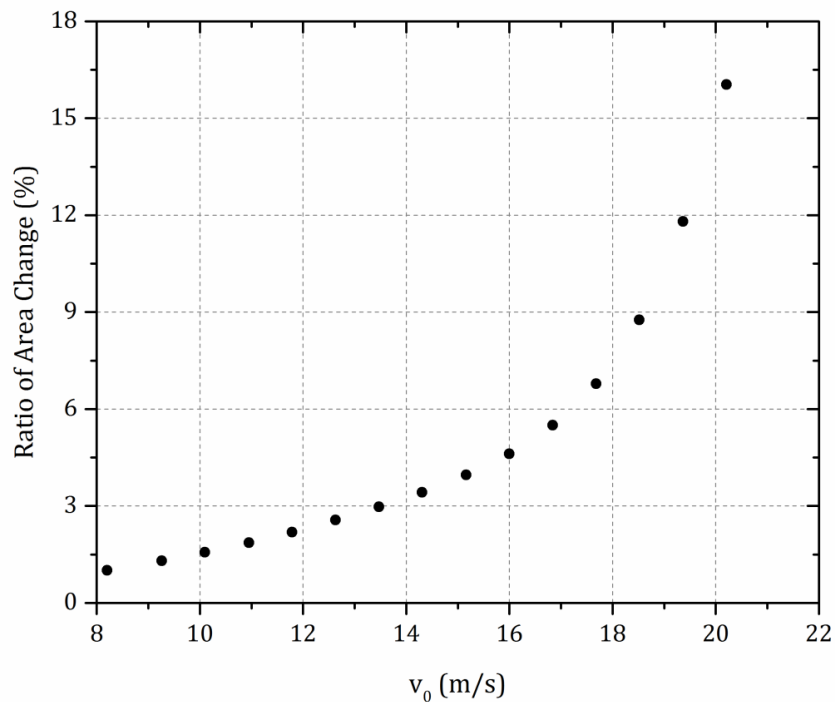


Figure 4.5. Ratio of area change at the leading edge for different fluid velocities in the channels.

4.2. Results from Case 2

In Case 2, flow channels and fuel plates with thicknesses smaller than the nominal conditions were modeled. In this case, the same criterion of Case 1 is used. It is important to recall that it establishes that the velocity where the maximum deflection of the plates varied from a linear (R-square ≥ 0.95) to nonlinear behavior is identified as the critical flow velocity. This principle is also contemplated in the following cases.

The maximum deflection of the plates versus the velocity squared is plotted in Figure 4.6. The fluid velocity where the curve shape altered is equal to 16.68 m/s, and then this is the critical flow velocity. It is about 1% lower than that found out in Case 1.

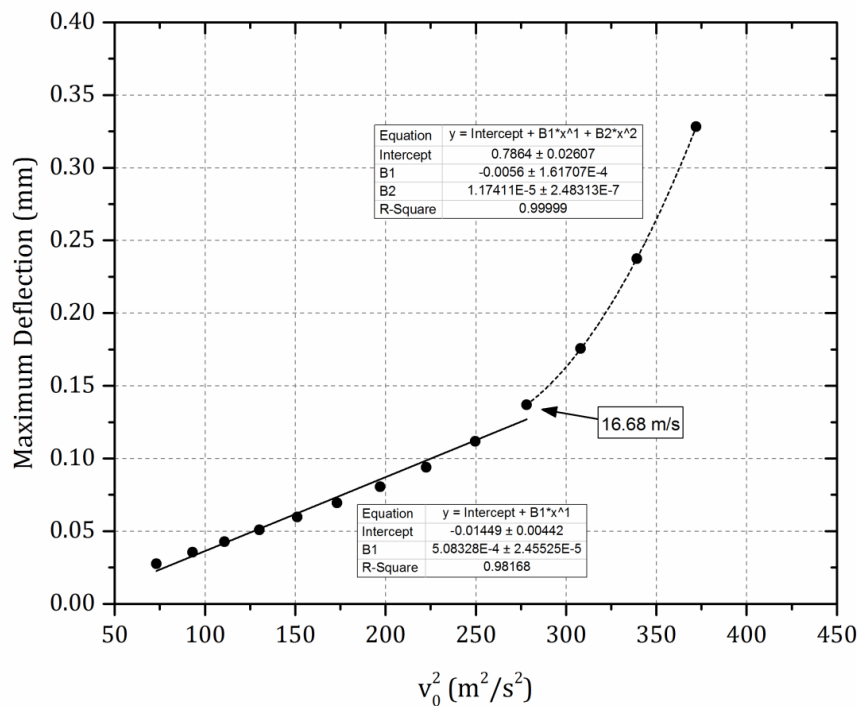


Figure 4.6. Maximum deflection of Plate 1 or 2 as a function of the square of the fluid velocity in the channels in Case 2. The arrow points out the critical fluid velocity

4.3. Results from Case 3

In the third subassembly, Plate 1 was located between the two-equal coolant channels and Plate 2 was surrounded by channels with different thicknesses. As can be seen in Figure 4.7, Plate 2 deflection is larger. This is a result of a higher pressure difference between the two adjacent channels with unequal dimensions. Additionally, during each flow test, Plate 2 was seen to deflect into the larger channel.

Figure 4.8 provides a visualization of the flow redistribution around the leading edge of the plates. Pressure contours along the midplane of the coolant channels are shown in Figure 4.9. The flow and pressure fields in these figures prove that there is a difference in pressure and flow velocity in the coolant channels.

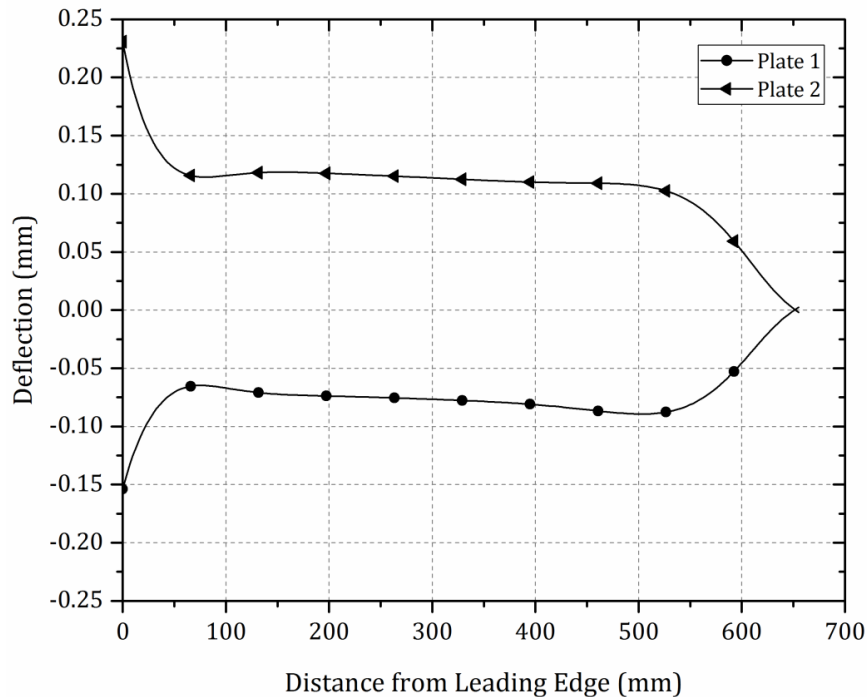


Figure 4.7. Deflection profile of each plate for a fluid velocity in the channels of 17.07 m/s.

In Figure 4.10, it should be noted that the total deflection of the plates is higher when different channels are considered. For this numerical experiment, the shape of the curve changed for an average fluid velocity in the channels of 16.21 m/s. This critical velocity is around 3.7% lesser than that indicated in Case 1. The results from the analysis show that, if initial channels deviations are present, greater deflections of the plates occur and the critical velocity may be expected at lower velocities.

4.4. Results from Case 4

In Case 4, where plates and coolant channels with nominal dimensions but materials properties at operating temperatures were considered, the critical velocity was detected at 16 m/s (see Figure 4.11). Relating to the value determined in Case 1, it was found that the critical velocity fell approximately 5%. This is a result of the reduction of the mechanical strength of the fuel plates with the increment of temperature.

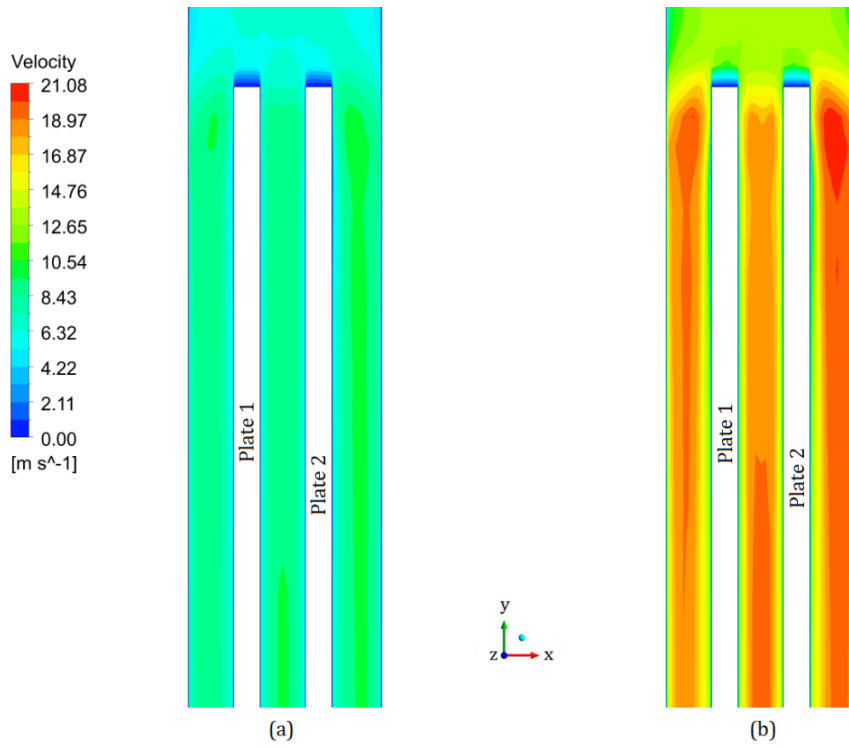


Figure 4.8. Velocity contours along the midplane of the channels and close to the leading edge of the plates for inlet fluid velocities of (a) 6.08 m/s and (b) 12.49 m/s. Fluid flow is downward and the plates are presented undeformed.

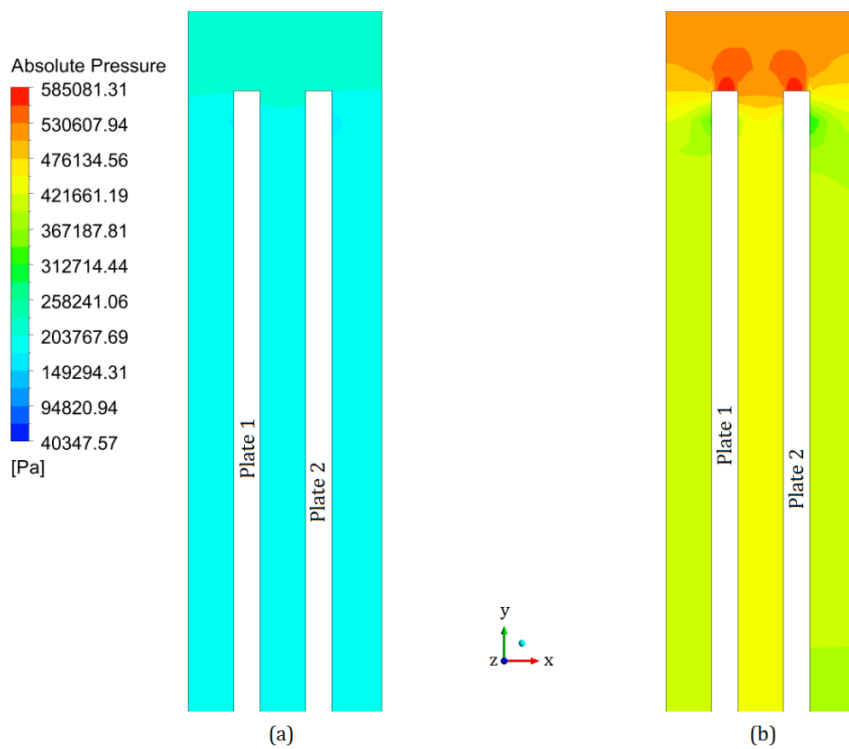


Figure 4.9. Pressure contours along the midplane of the channels and close to the leading edge of the plates for inlet fluid velocities of (a) 6.08 m/s and (b) 12.49 m/s. Fluid flow is downward and the plates are presented undeformed.

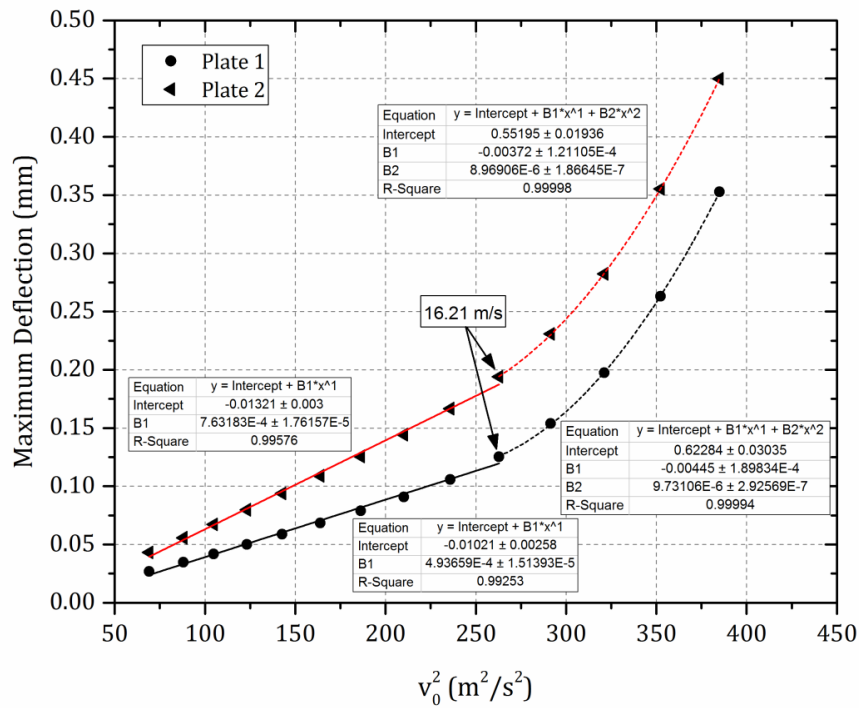


Figure 4.10. Maximum deflection of the plates as a function of the square of the fluid velocity in the channels in Case 3. The arrows point out the critical fluid velocity

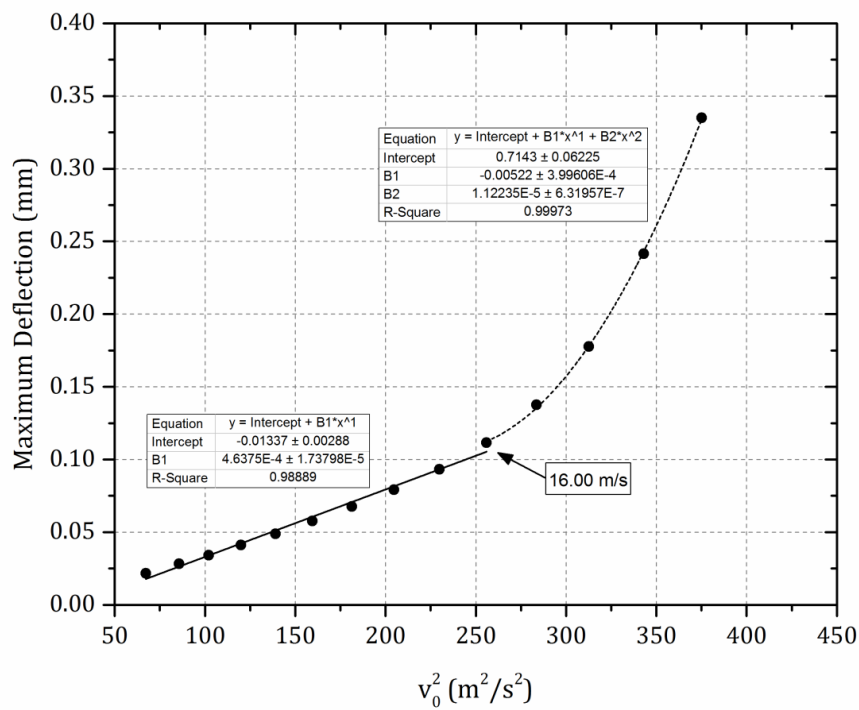


Figure 4.11. Maximum deflection of Plate 1 or 2 as a function of the square of the fluid velocity in the channels in Case 4. The arrow points out the critical fluid velocity

Figure 4.12 shows a comparison between the maximum deflection calculated in Cases 4 and that predicted in Case 1. The interesting points to note in the graph are the small differences in the maximum deflections from one analysis to the next up to a fluid velocity of approximately 16 m/s. However, above this value, the maximum deflections are larger in Case 4.

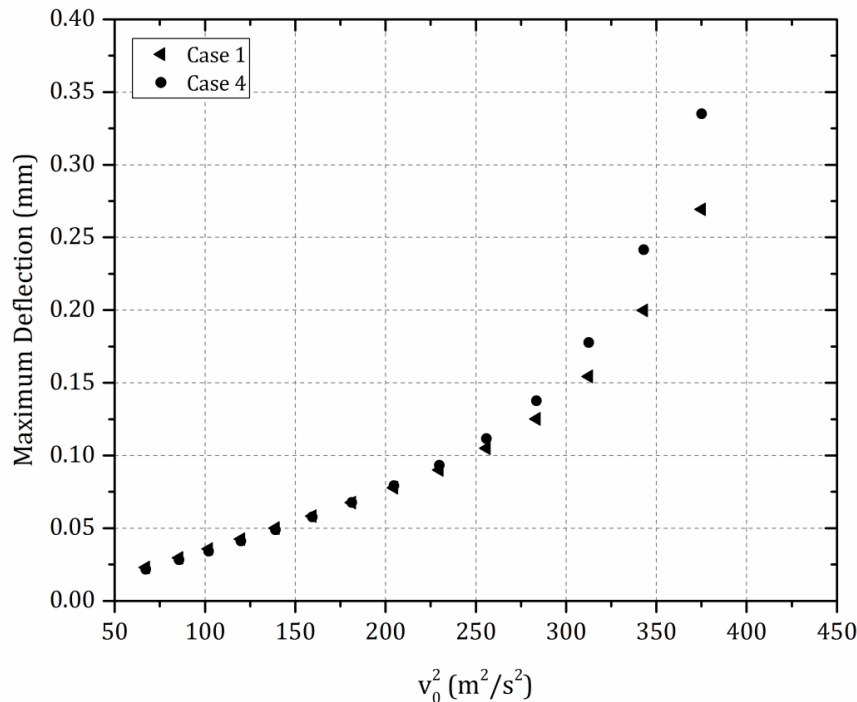


Figure 4.12. Maximum deflection of Plate 1 or 2 as a function of the square of the fluid velocity in the channels: comparison between cases 1 and 4.

4.5. Results from Case 5

In this case, a path was created along the axial centerline of the coolant channels. From these paths, the static pressure profiles were determined. The pressure differences between the central channel and the side channels were calculated. For both lateral channels, identical pressure profiles were identified. The resulting pressure differentials are shown in Figure 4.13. One more time, because similar deflection profiles were detected for both plates, only the profile of Plate 1 is depicted in Figure 4.14.

The results of this case with the support comb and Case 1 have been published in the scientific journal “Nuclear Engineering and Design” (González Mantecón and Mattar Neto, 2019, 2018).

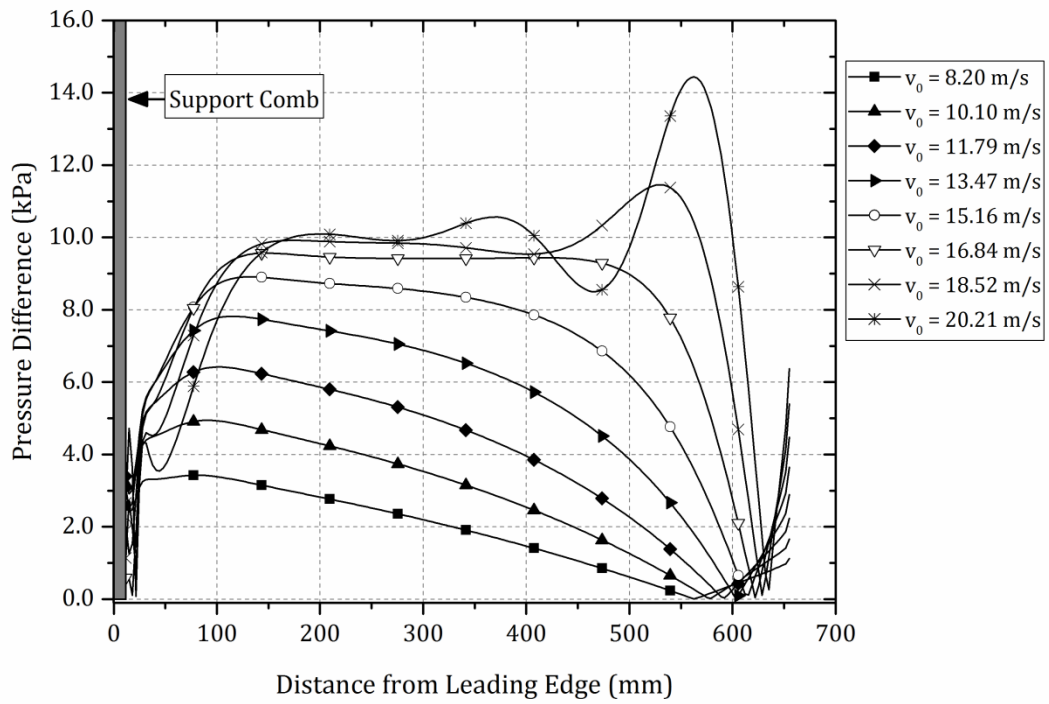


Figure 4.13. Pressure difference along the length of Plate 1 for different fluid velocities in the channels, with the support comb at the inlet end of the plates.

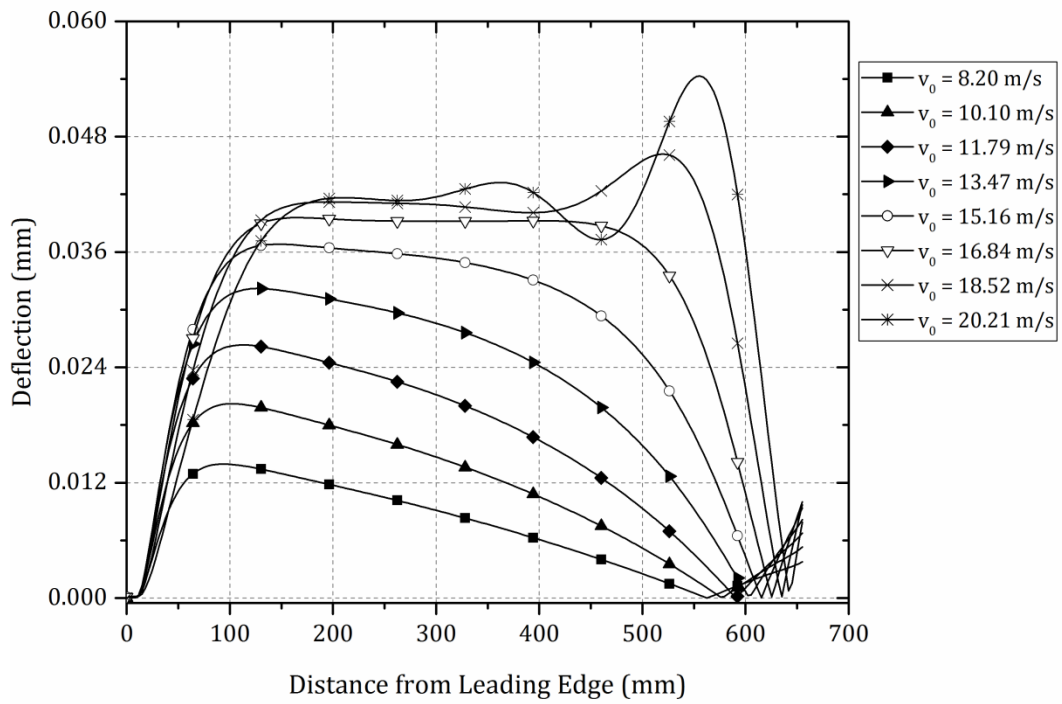


Figure 4.14. Deflection profile of Plate 1 for different fluid velocities in the channels, with the support comb at the inlet end of the plates.

Figure 4.15 shows a comparison between the deflection profiles when the inlet support comb is used and when it is not (Case 1). It is of interest to note from these figures that the static divergence at the leading edge of the plates was eliminated. However, even with the comb, the plates are prone to deflect over their full length with the rise of the fluid velocity. In addition, with this increment, the maximum deflection occurred in a different point of the plates. Nonetheless, it should be highlighted that the positioning of a support comb across the leading edges of the plates was found to significantly reduce the deflections along the entire length of the plates.

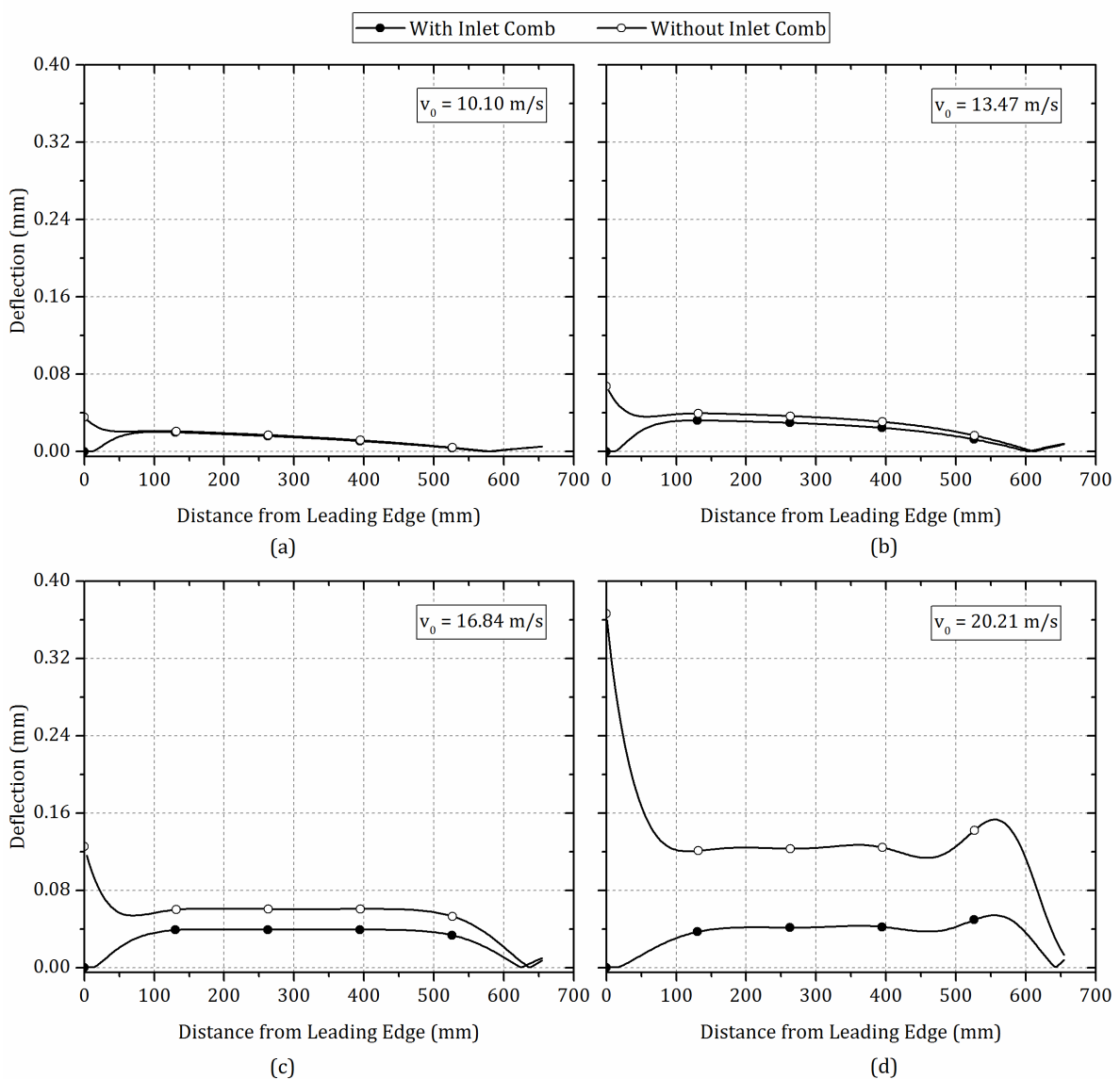


Figure 4.15. Deflection profile of Plate 1 for different fluid velocities in the channels, with and without the support comb at the inlet end of the plates.

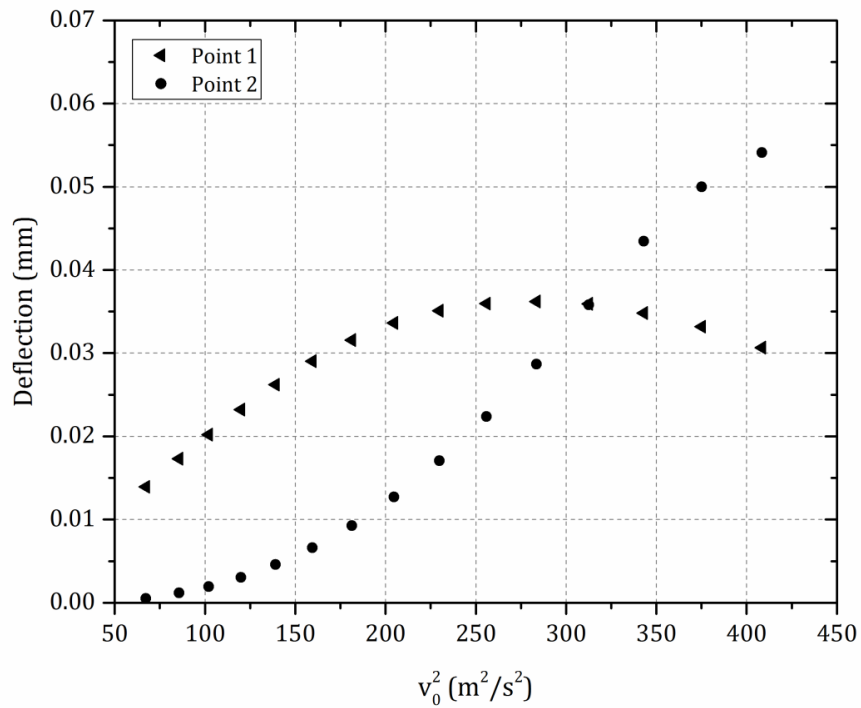


Figure 4.16. Deflection of the plate at two different points. Point 1 is located at 100 mm from the leading edge and Point 2 at 550 mm.

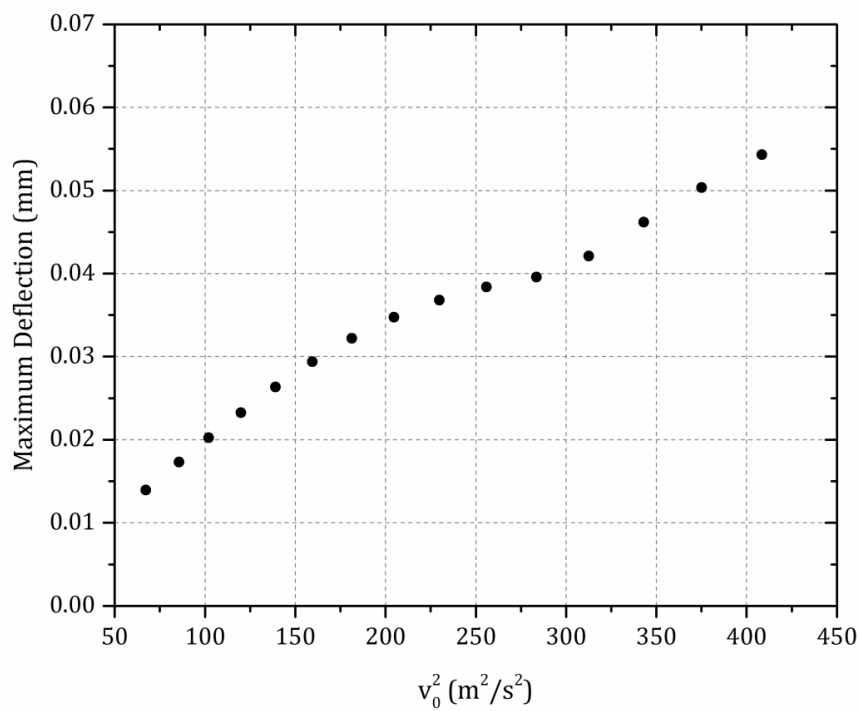


Figure 4.17. Maximum deflection of Plate 1 or 2 as a function of the square of the fluid velocity in the channels in Case 5.

Knowing that the maximum deflection of the plates changed its location when the fluid velocity was augmented, the deflection at two points was extracted. Point 1 was positioned at 100 mm and Point 2 at 550 mm from the leading edge (see Figure 4.16). In the figure, the nonlinear deflection increase is observed even for low flows.

The maximum deflection of the plates for Case 5 is illustrated in Figure 4.17. In this graph, the curve follows a trend different than that recognized in the previous four cases. Therefore, it was not possible to identify the critical velocity. So, for this case, this velocity should be expected at a fluid velocity beyond 1.2 times the Miller's velocity.

In Figure 4.18, the maximum deflection of Case 5 is compared with that obtained in Case 1. It can be seen how the magnitude of the maximum deflection has been considerably diminished with the addition of the comb.

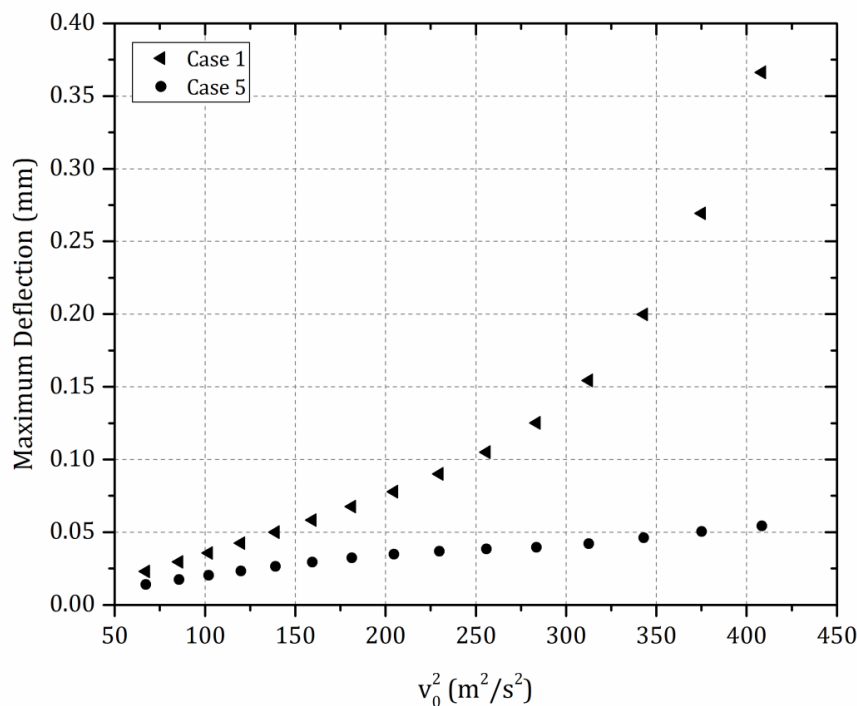


Figure 4.18. Maximum deflection of Plate 1 or 2 as a function of the square of the fluid velocity in the channels: comparison between cases 1 and 5.

4.6. Comparison with Miller's Velocity

A comparison can be made to relate this study to Miller's critical velocity. Table 4.2 summarizes the computed velocity for four different situations and the percent

difference of this velocity relative to Miller’s solution. Note that in Case 3, an average channel thickness of 2.417 mm was used to estimate the theoretical critical velocity.

Table 4.2. Comparison between the critical fluid velocity predicted with the multiphysics model and Miller’s velocity for cases 1 to 4.

Case	v_c (m/s)	v_M (m/s)	Difference (%)
1	16.84	16.84	0.0
2	16.68	16.13	3.4
3	16.21	16.36	0.9
4	16	16.43	2.6

It is noteworthy that, in Case 1, the critical velocity determined with the FSI model is coincident with Miller’s velocity of the assembly (see Table 4.2). However, for other geometrical configurations and materials properties, there is a difference between the predicted velocity and Miller’s velocity because Miller’s model is very simplified and the methodology proposed here is more detailed.

5. CONCLUSIONS AND FUTURE WORKS

5.1. Conclusions

In this work, a fluid-structure interaction analysis for evaluating the mechanical stability of nuclear fuel plates under axial flow conditions was presented. The adopted model is representative of the fuel plates and coolant channels projected for the Brazilian Multipurpose Reactor. The numerical strategy was based on the two-way fluid-structure interaction method, in which the fluid loads calculated by the fluid model are sent to structural model as boundary conditions and the displacements of the structure are transferred back to the CFD analysis. The important results of the current study can be summarized as follows:

- 1- The proposed methodology, within the limits of the conditions considered herein, allowed predicting the critical velocity of the fuel plates without a support comb. In cases 1 to 4 this comb was not considered and the maximum deflection was detected at the leading edge of the plates. The results from these cases also demonstrated that the estimated critical velocity is an indication of the flow rate at which the deflections become larger, rather than the sudden collapse of the fuel plates. Moreover, for flow rates above the critical velocity, an extra deflection peak downstream of the entrance was found. Plastic deformation of the plates was not noticed in the analyzed cases.
- 2- The results from cases 2 and 3 revealed that, if initial tolerances on fluid channel dimensions exist, deflections of the fuel plates will be amplified due to the imposed pressure difference, and the critical velocity may be expected at lower flow rates (see Figure 4.6 and Figure 4.10). Likewise, it was perceived that coolant channels with different thicknesses cause larger deflections than channels with smaller but equal thicknesses.
- 3- The influence of materials properties on flow-induced deflections of the plates was investigated in Case 4. It was verified the decrease of the critical velocity magnitude with the increment of the system temperature (see Figure 4.11).
- 4- The results from Case 5 corroborated that the static divergence at the inlet end of the plates was effectively removed with the addition of the comb (see Figure

4.15). In addition, this device substantially reduced the flow-induced deflections along the full length of the plates, thus stabilizing the plates to a very significant extent.

5- The methodology demonstrated to be an accurate tool to predict the critical velocity. In particular, in cases 1 to 4, it shows good agreement with the value given by Miller's formula, which is the method currently employed in the design of new fuel assemblies (see Table 4.2).

The main contribution of this dissertation is that it provides a methodology to predict the critical flow velocity of flat-plate-type fuel assemblies by using numerical simulations of fluid-structure interaction. The methodology developed herein could be applied to study configurations with several fuel plates. Thus, it represents an alternative tool that could be used during the project of new fuel assemblies, giving support to traditional methods and reducing the necessity for experimental apparatus to comprehend the flow-induced effects on the plates for different conditions. This study lastly objectively demonstrates that, from the design standpoint of fuel elements, the support comb is an appropriate solution to stabilize the fuel plates, provided that the changes in cross-sectional area of the flow channel are less than about 30%.

5.2. Recommendation for Future Works

The work detailed in this dissertation focuses on the analysis of fuel plates comprised of uranium-silicide in an aluminum matrix. However, a novel monolithic LEU fuel with a uranium-molybdenum (U-Mo) alloy foil is under consideration to replace the current U-Al dispersion HEU fuel. That configuration has been identified as a promising very-high density fuel type producing fuel loading up to 15.3 gU/cm^3 (Lemoine and Wachs, 2007). The fuel plate design uses U-Mo fuel meat and aluminum clad. Between them, a thin zirconium layer is deposited to prevent the development of fission gas bubbles at the fuel-clad interface. Besides that, the clad thickness has been reduced to allow for additional coolant flow between the fuel plates. This extra fluid volume in the reactor core offers greater neutron moderation, which results in lower cost and longer life of the fuel assemblies. With this layered structure, as well as the overall thinning of the fuel plates, the plates may be more vulnerable to flow-induced deflections. For this reason, future research works should include the laminate sandwich structure to the plate geometry to quantify hydro-mechanical effects in the fuel plates.

Flat plate fuel assemblies have been the motivation of this work. However, many reactors around the world use and are being planned with cylindrical plate-type geometry. Hence, we suggest employing the methodology for studying FSI phenomena of fuel elements composed of curved plates.

REFERENCES

- Adams, T., Grant, C., Watson, H., 2012. A Simple Algorithm to Relate Measured Surface Roughness to Equivalent Sand-grain Roughness. *Int. J. Mech. Eng. Mechatronics* 1. <https://doi.org/10.11159/ijmem.2012.008>
- Andrade, D.A. de, Angelo, G., Angelo, E., Di Giovanni Santos, P.H., Branco Vaz de Oliveira, F., Torres, W.M., Umbehaun, P.E., Batista De Souza, J.A., Belchior Junior, A., Sabundjian, G., Carvalho Prado, A. de, 2015. A CFD Numerical Model for the Flow Distribution in a MTR Fuel Element, in: *Proceedings of the 2015 International Nuclear Atlantic Conference - INAC*. Brazilian Nuclear Energy Association, São Paulo, Brazil.
- ANSYS Inc., 2017a. ANSYS CFX Documentation - Release 18.2. Canonsburg, USA.
- ANSYS Inc., 2017b. ANSYS Mechanical Documentation - Release 18.2. Canonsburg, USA.
- ASM International, 1990. *ASM Handbook, Volume 2 Properties and Selection: Nonferrous Alloys and Special-Purpose Materials*, 10th ed. ASM International.
- ASME, 2009. *Standard for Verification and Validation in Computational Fluid Dynamics and Heat Transfer*. ASME V&V 20-2009, New York, USA.
- Castro, A.J.A. de, 2017. *Análise experimental de velocidade crítica em elemento combustível tipo placa plana para reatores nucleares de pesquisa*. Tese de Doutorado, Universidade de São Paulo, São Paulo. <https://doi.org/10.11606/T.85.2017.tde-23052017-160724>
- Causin, P., Gerbeau, J.F., Nobile, F., 2005. Added-mass effect in the design of partitioned algorithms for fluid–structure problems. *Comput. Methods Appl. Mech. Eng.* 194, 4506–4527. <https://doi.org/10.1016/j.cma.2004.12.005>
- Cekirge, H.M., Ural, E., 1978. Critical coolant flow velocities in reactors having parallel fuel plates. *Comput. Math. with Appl.* 4, 153–156. [https://doi.org/10.1016/0898-1221\(78\)90025-1](https://doi.org/10.1016/0898-1221(78)90025-1)
- Chapra, S.C., Canale, R.P., 2015. *Numerical Methods for Engineers*, 7th ed. McGraw-Hill Education, New York.

- Curtis, F.G., Ekici, K., Freels, J.D., 2013. Fluid-Structure Interaction Modeling of High-Aspect Ratio Nuclear Fuel Plates Using COMSOL, in: Proceedings of the 2013 COMSOL Conference. Boston, USA.
- Davari, A., Mirvakili, S.M., Abedi, E., 2015. Three-dimensional analysis of flow blockage accident in Tehran MTR research reactor core using CFD. *Prog. Nucl. Energy* 85, 605–612. <https://doi.org/10.1016/j.pnucene.2015.08.008>
- Davis, D.C., Kim, G., 1991. Design against Hydrodynamic Instabilities in Flat-Plate Type Fuel Element Assemblies, in: Transactions of the 11th International Conference on Structural Mechanics in Reactor Technology - SMiRT11. Tokyo, Japan, pp. 105–109.
- Doan, R.L., 1958. The Engineering Test Reactor - A Status Report. *Nucleonics* 16.
- Du, Y., 2010. Numerical Simulation Of Mechanical and Thermal Fluid–Structure Interaction in Labyrinth Seals. PhD Dissertation, Technischen Universitat Darmstadt, Darmstadt.
- Fan, W., Peng, C., Guo, Y., 2015. CFD study on inlet flow blockage accidents in rectangular fuel assembly. *Nucl. Eng. Des.* 292, 177–186. <https://doi.org/10.1016/j.nucengdes.2015.06.016>
- Gong, D., Huang, S., Wang, G., Wang, K., 2015. Heat Transfer Calculation on Plate-Type Fuel Assembly of High Flux Research Reactor. *Sci. Technol. Nucl. Install.* 2015, 1–13. <https://doi.org/10.1155/2015/198654>
- González Mantecón, J., Mattar Neto, M., 2019. Numerical analysis on stability of nuclear fuel plates with inlet support comb. *Nucl. Eng. Des.* 342, 240–248. <https://doi.org/10.1016/j.nucengdes.2018.12.009>
- González Mantecón, J., Mattar Neto, M., 2018. Numerical methodology for fluid-structure interaction analysis of nuclear fuel plates under axial flow conditions. *Nucl. Eng. Des.* 333, 76–86. <https://doi.org/10.1016/j.nucengdes.2018.04.009>
- Groninger, R.D., Kane, J.J., 1963. Flow Induced Deflections of Parallel Flat Plates. *Nucl. Sci. Eng.* 16, 218–226. <https://doi.org/10.13182/NSE63-A26503>
- Guo, C.Q., Paidoussis, M.P., 2000. Stability of Rectangular Plates With Free Side-Edges in Two-Dimensional Inviscid Channel Flow. *J. Appl. Mech.* 67, 171–176. <https://doi.org/10.1115/1.321143>

- Ho, M., Hong, G., Mack, A.N.F., 2004. Experimental Investigation of Flow-Induced Vibration in a Parallel Plate Reactor Fuel Assembly, in: Proceedings of the 15th Australian Fluid Mechanics Conference. Sydney, Australia.
- Howard, T.K., Marcum, W.R., Jones, W.F., 2015. A novel approach to modeling plate deformations in fluid-structure interactions. *Nucl. Eng. Des.* 293, 1–15.
<https://doi.org/10.1016/j.nucengdes.2015.06.010>
- IAEA, 2019. Research Reactors Database [WWW Document]. URL
<https://nucleus.iaea.org/RRDB/Reports/Container.aspx?Id=A1> (accessed 1.15.19).
- IAEA, 1980. Research Reactor Core Conversion from the Use of Highly Enriched Uranium to the Use of Low Enriched Uranium Fuels: Guidebook. IAEA-TECDOC-233, Vienna, Austria.
- INVAP, 2013. Brazilian Multipurpose Reactor Project - Core Thermal-Hydraulic Design in Forced Convection. Report No. RMBP-0130-2IIN-005-A.
- Jensen, P., Marcum, W.R., 2014. Predicting critical flow velocity leading to laminate plate collapse - flat plates. *Nucl. Eng. Des.* 267, 71–87.
<https://doi.org/10.1016/j.nucengdes.2013.11.071>
- Jesse, C.J., 2015. Analysis of the potential for flow-induced deflection of Nuclear reactor fuel plates under high velocity flows. MSc Thesis, University of Missouri, Columbia.
- Johansson, E.B., 1959. Hydraulic Instability of Reactor Parallel-Plate Fuel Assemblies. Report No. KAPL-M-EJ-9, Knolls Atomic Power Laboratory, Schenectady, USA.
<https://doi.org/10.2172/4221444>
- Kane, J.J., 1963. The Effect of Inlet Spacing Deviations on the Flow-Induced Deflections of Flat Plates. *Nucl. Sci. Eng.* 15, 305–308. <https://doi.org/10.13182/NSE63-A26441>
- Kennedy, J.C., 2015. Development and Experimental Benchmarking of Numeric Fluid Structure Interaction Models for Research Reactor Fuel Analysis. PhD Dissertation, University of Missouri, Columbia.
- Kennedy, J.C., 2012. Hydro-Mechanical Analysis of Low Enriched Uranium Fuel Plates for University of Missouri Research Reactor. MSc Thesis, University of Missouri, Columbia.

- Kim, G., Davis, D.C., 1995. Hydrodynamic instabilities in flat-plate-type fuel assemblies. Nucl. Eng. Des. 158, 1–17. [https://doi.org/10.1016/0029-5493\(95\)01023-B](https://doi.org/10.1016/0029-5493(95)01023-B)
- Kim, Y.T., Scarton, H.A., 1977. Flow-Induced Bending of Rectangular Plates. J. Appl. Mech. 44, 207. <https://doi.org/10.1115/1.3424025>
- Kwaśniewski, L., 2013. Application of grid convergence index in FE computation. Bull. Polish Acad. Sci. Tech. Sci. 61, 123–128. <https://doi.org/10.2478/bpasts-2013-0010>
- Lauder, B.E., Spalding, D.B., 1974. The numerical computation of turbulent flows. Comput. Methods Appl. Mech. Eng. 3, 269–289. [https://doi.org/10.1016/0045-7825\(74\)90029-2](https://doi.org/10.1016/0045-7825(74)90029-2)
- Lemoine, P., Wachs, D., 2007. High density fuel development for Research Reactors, in: International Conference on Research Reactors. Sydney, Australia.
- Marcum, W.R., 2014. Predicting critical flow velocity leading to laminate plate collapse - Cylindrical plates. Nucl. Eng. Des. 278, 50–63. <https://doi.org/10.1016/j.nucengdes.2014.07.015>
- Menter, F.R., 1994. Two-equation eddy-viscosity turbulence models for engineering applications. AIAA J. 32, 1598–1605. <https://doi.org/10.2514/3.12149>
- Miller, D.R., 1958. Critical Flow Velocities for Collapse of Reactor Parallel-Plate Fuel Assemblies. Report No. KAPL-1954, Knolls Atomic Power Laboratory, Schenectady, USA. <https://doi.org/10.2172/4199355>
- NTI, 2010. Past and Current Civilian HEU Reduction Efforts [WWW Document]. URL <https://www.nti.org/analysis/articles/past-and-current-civilian-heu-reduction-efforts/> (accessed 1.15.19).
- Oberkampf, W.L., Roy, C.J., 2010. Verification and Validation in Scientific Computing. Cambridge University Press, Cambridge. <https://doi.org/10.1017/CBO9780511760396>
- Pavone, S.J., Scarton, H.A., 1983. Laminar flow induced deflections of stacked plates. Nucl. Eng. Des. 74, 79–89. [https://doi.org/10.1016/0029-5493\(83\)90141-3](https://doi.org/10.1016/0029-5493(83)90141-3)
- Perrotta, J.A., Soares, A.J., 2015. RMB: The New Brazilian Multipurpose Research Reactor. Int. J. Nucl. Power 60, 30–34.

- Rao, A., 2003. Fluid-solid interaction analysis using ANSYS/multiphysics, in: 2nd MIT Conference on Computational Fluid and Solid Mechanics 2003. Elsevier Science, Boston, USA, pp. 1492–1496.
- Rao, S.S., 2011. The Finite Element Method in Engineering, 5th ed. Elsevier.
- Richardson, L.F., 1911. The Approximate Arithmetical Solution by Finite Differences of Physical Problems Involving Differential Equations, with an Application to the Stresses in a Masonry Dam. *Philos. Trans. R. Soc. A Math. Phys. Eng. Sci.* 210, 307–357. <https://doi.org/10.1098/rsta.1911.0009>
- Roache, P.J., 1998. Verification and Validation in Computational Science and Engineering. Hermosa Publishers, Albuquerque.
- Salama, A., 2011. CFD investigation of flow inversion in typical MTR research reactor undergoing thermal–hydraulic transients. *Ann. Nucl. Energy* 38, 1578–1592. <https://doi.org/10.1016/j.anucene.2011.03.005>
- Salim, S.M., Cheah, S.C., 2009. Wall y^+ Strategy for Dealing with Wall-bounded Turbulent Flows, in: Proceedings of the International MultiConference of Engineers and Computer Scientists - IMECS. Hong Kong, Hong Kong.
- Scavuzzo, R.J., 1965. Hydraulic Instability of Flat Parallel-Plate Assemblies. *Nucl. Sci. Eng.* 21, 463–472. <https://doi.org/10.13182/NSE65-A18790>
- Schlichting, H., 1968. Boundary-Layer Theory, 6th ed. McGraw-Hill.
- Schwer, L.E., 2008. Is your mesh refined enough? Estimating Discretization Error using GCI, in: 7th LS-DYNA Anwenderforum. Bamberg, Germany, pp. 45–54.
- Smissaert, G.E., 1969. Static and dynamic hydroelastic instabilities in MTR-type fuel elements part II. Theoretical investigation and discussion. *Nucl. Eng. Des.* 9, 105–122. [https://doi.org/10.1016/0029-5493\(69\)90052-1](https://doi.org/10.1016/0029-5493(69)90052-1)
- Smissaert, G.E., 1968. Static and dynamic hydroelastic instabilities in MTR-type fuel elements Part I. Introduction and experimental investigation. *Nucl. Eng. Des.* 7, 535–546. [https://doi.org/10.1016/0029-5493\(68\)90103-9](https://doi.org/10.1016/0029-5493(68)90103-9)
- Smith, R.L., 1968. Dynamic Pressure Limits for Flat Plates as Related to Nuclear Fuel Elements. Report No. NASA TN D-4417, Lewis Research Center, Cleveland, USA.

- Stromquist, W.K., Sisman, O., 1948. High Flux Reactor Fuel Assemblies Vibration and Water Flow. Problem Assignment No. TX5-12. <https://doi.org/10.2172/4351600>
- Tentner, A., Bojanowski, C., Feldman, E., Wilson, E., Solbrekken, G., Jesse, C., Kennedy, J., Rivers, J., Schnieders, G., 2017. Evaluation of Thin Plate Hydrodynamic Stability through a Combined Numerical Modeling and Experimental Effort. Report No. ANL/RTR/TM-16/9, Argonne National Laboratory, Lemont, USA.
- Tu, J., Yeoh, G.-H., Liu, C., 2013. Computational Fluid Dynamics, 2nd ed. Elsevier. <https://doi.org/10.1016/C2010-0-67980-6>
- Versteeg, H.K., Malalasekera, W., 2007. An Introduction to Computational Fluid Dynamics: The Finite Volume Method, 2nd ed. Prentice Hall.
- Wambsganss, M.W., 1967. Second-Order Effects as Related to Critical Coolant Flow Velocities in Reactor Parallel Plate Fuel Assemblies. Nucl. Eng. Des. 5, 268–276.
- Weaver, D.S., Unny, T.E., 1970. The Hydroelastic Stability of a Flat Plate. J. Appl. Mech. 37, 823. <https://doi.org/10.1115/1.3408615>
- White, F.M., 2011. Fluid Mechanics, 7th ed. McGraw-Hill, New York.
- Zabriskie, W.L., 1959. An Experimental Evaluation of the Effect of Length-to-Width Ratio on the Critical Flow Velocity of Single Plate Assemblies. Schenectady, USA.
- Zabriskie, W.L., 1958. An Experimental Evaluation of Critical Flow Velocity Formulas for Parallel Plate Assemblies. Schenectady, USA.
- Zienkiewicz, O.C., Taylor, R.L., Zhu, J.Z., 2013. The Finite Element Method: its Basis and Fundamentals, 7th ed. Elsevier. <https://doi.org/10.1016/C2009-0-24909-9>


```

Error = abs(f1 - fin)
fin = f1

dPin = 0.5*fin*rho*Li*vin**2/Din    # Inlet pressure drop

# Pressure drop due to the friction in channels
Rech = rho*v0*Dch/miu              # Channel Reynolds number

fch = 0.001
Error = 1.0
while (Error > 1.0E-10):
    Y = 1/m.sqrt(fch) + 2*m.log(e/(3.7*Dch)+2.51/(Rech*m.sqrt(fch)), 10)
    dY1 = -1/(2*fin*m.sqrt(fch))
    dY2 = -(1/((e/(3.7*Dch)+2.51/(Rech*m.sqrt(fch)))*m.log(10)))
    dY3 = (2.51/(Rech*fch*m.sqrt(fch)))
    dY = dY1 + dY2*dY3
    f2 = fch - Y/dY
    Error = abs(f2 - fch)
    fch = f2

dPch = 0.5*(fch)*rho*Lp*v0**2/Dch    # Channel pressure drop

# Pressure drop from the sudden contraction into channel 1 and channel 2
dPsc = 0.5*Ksc1*rho*v0**2

# Pressure drop from the sudden expansion from channel 1 and channel 2
dPse = 0.5*Kse1*rho*v0**2

# Pressure drop through the outlet plenum
dPout = 0.5*fin*rho*Lo*vin**2/Din

# Overall channel pressure drop
dP = dPin + dPsc + dPch + dPse + dPout

# Wall Shear Stress Channel
tau = (1/8)*rho*fch*(v0)**2

"===== Printing & Plotting Results=====
print()
print("+=====+")
print("|          DATA          |")
print("+=====+")
print("|          |          |")
print("| Channel Velocity: %.2f m/s" % v0 , " |")
print("| Inlet Velocity: %.2f m/s" % vin, " |")
print("|          |          |")
print("+=====+")
print("|          RESULTS          |")
print("+=====+")
print("|          |          |")
print("| Pressure Drop: %.0f Pa " % (dP), " |")
print("| Wall Shear Stress: %.2f Pa " % tau," |")
print("|          |          |")
print("+-----+")

```

APPENDIX C. SETTINGS OF THE FSI ANALYSIS

This appendix shows excerpts of the output files of the FSI analysis where input parameters of the model can be seen. These examples were taken from Case 1.

C.1. Excerpts from the CFX Output File

```
. . .
FLOW: Flow Analysis 1
ANALYSIS TYPE:
  Option = Transient
EXTERNAL SOLVER COUPLING:
  ANSYS Input File = ds.dat
  Option = ANSYS MultiField
COUPLING TIME CONTROL:
  COUPLING INITIAL TIME:
    Option = Automatic
  END
  COUPLING TIME DURATION:
    Option = Total Time
    Total Time = 0.625 [s]
  END
  COUPLING TIME STEPS:
    Option = Timesteps
    Timesteps = 0.025 [s]
  END
END
END
. . .
DOMAIN: Coolant
. . .
BOUNDARY: External Walls
  Boundary Type = WALL
. . .
BOUNDARY CONDITIONS:
  MASS AND MOMENTUM:
    Option = No Slip Wall
    Wall Velocity Relative To = Mesh Motion
  END
  MESH MOTION:
    Option = Stationary
  END
. . .
END
. . .
BOUNDARY: Plate_Left
. . .
BOUNDARY CONDITIONS:
  MASS AND MOMENTUM:
    Option = No Slip Wall
    Wall Velocity Relative To = Mesh Motion
  END
  MESH MOTION:
```

```
        ANSYS Interface = FSIN_1
        Option = ANSYS MultiField
        Receive from ANSYS = Total Mesh Displacement
        Send to ANSYS = Total Force
    END
    . . .
END
BOUNDARY: Plate_Right
    Boundary Type = WALL
    . . .
    BOUNDARY CONDITIONS:
        MASS AND MOMENTUM:
            Option = No Slip Wall
            Wall Velocity Relative To = Mesh Motion
        END
        MESH MOTION:
            ANSYS Interface = FSIN_2
            Option = ANSYS MultiField
            Receive from ANSYS = Total Mesh Displacement
            Send to ANSYS = Total Force
        END
    . . .
END
    . . .
OUTPUT CONTROL:
    . . .
    MONITOR POINT: Point 2 Total
        Cartesian Coordinates = 3.125 [mm], 327.5 [mm], 0 [mm]
        Coord Frame = Coord 0
        Option = Cartesian Coordinates
        Output Variables List = Total Mesh Displacement
    MONITOR LOCATION CONTROL:
        Interpolation Type = Nearest Vertex
    END
    POSITION UPDATE FREQUENCY:
        Option = Initial Mesh Only
    END
END
    . . .
    MONITOR POINT: forcePlateLeft
        Coord Frame = Coord 0
        Expression Value = forceTotalPlateLeft
        Option = Expression
    END
    . . .
CONVERGENCE CONTROL:
    Maximum Number of Coefficient Loops = 5
    Minimum Number of Coefficient Loops = 2
    Timescale Control = Coefficient Loops
END
    . . .
MFX RUN CONTROL:
    MFX RUN DEFINITION:
        MFX Run Mode = Start ANSYS and CFX
        Process ANSYS Input File = On
        Restart ANSYS Run = Off
    END
    . . .
```

C.2. Excerpts from the ANSYS Mechanical Output File

```

. . .
***** SF,FSIN_2,FSIN,2
***** nsel,all
***** tblast
***** /gst,on,on
***** fini
***** *get,_numnode,node,0,count
***** *get,_numelem,elem,0,count
***** *get,_MAXELEMNUM, elem, 0, NUM, MAX
***** *get,_MAXNODENUM, node, 0, NUM, MAX
***** *get,_MAXELEMTYPE, etyp, 0, NUM, MAX
***** *get,_MAXREALCONST, real, 0, NUM, MAX
***** /go
***** /wb,load,end ! done creating loads
***** /com,--- Number of total nodes = %_numnode%
***** /com,--- Number of contact elements = 0
***** /com,--- Number of spring elements = 0
***** /com,--- Number of bearing elements = 0
***** /com,--- Number of solid elements = 299200
***** /com,--- Number of total elements = %_numelem%
***** *get,_wallbsol,active,,time,wall
*****
/com,*****
/com,***** SOLUTION *****
/com,*****
/solu
***** antype,4 ! transient analysis
***** nlgeom,on ! Turn on Large Deformation Effects
***** kbc,1 ! stepped BC's
***** eqsl,pcg,1e-8,,,,,1
***** msave,on
***** cntr,print,1 ! print out contact info and also make no
initial contact an error
***** rstssuppress,none ! don't suppress anything due to presense of
FSI loading
***** dmppoption,emat,no ! Don't combine emat file for DANSYS
***** dmppoption,esav,no ! Don't combine esav file for DANSYS
***** cmwrite ! Export components due to presence of FSI
loading
***** trnopt,full,,,,,hht ! HHT time integration method
***** tintp,0.1 ! Numerical Damping
***** nldiag,cont,iter ! print out contact info each equilibrium
iteration
***** rescontrol,define,last,last,,dele ! Program Controlled
***** /com,*****
***** /com,***** SOLVE FOR LS 1 OF 1 *****
***** /nopr
***** /gopr
***** autots,off ! User turned off automatic time stepping
***** nsub,1,1,1
***** time,1.
***** timint,on ! Turn on time integration effects
***** outres,erase
***** outres,all,none
***** outres,nsol,all
***** outres,rsol,all
***** outres, strs,all

```

```

***** outres,epel,all
***** outres,eppl,all
***** outres,v,all
***** outres,a,all
***** stabilize,off ! Stabilization turned OFF by user
***** ! ***** WB SOLVE COMMAND *****
***** ! check interactive state
***** *get,ANSINTER_,active,,int
***** *if,ANSINTER_,ne,0,then
***** *endif
***** MFAN,ON
***** MFTI,0.625
***** MFDT,0.025,0.025,0.025,OFF
***** MFLC,SURF,ANSYS,1,DISP,CFX,'Plate_Left','Total Mesh Displacement',NONC
***** MFLC,SURF,CFX,'Plate_Left','Total Force',ANSYS,1,FORC,CPP
***** MFLC,SURF,ANSYS,2,DISP,CFX,'Plate_Right','Total Mesh Displacement',NONC
***** MFLC,SURF,CFX,'Plate_Right','Total Force',ANSYS,2,FORC,CPP
***** MFIT,1,1,1
***** MFCO,ALL,1e-2
***** MFRE,ALL,0.75,RELX
***** MFPS,group1,ANSYS
***** MFPS,group2,CFX
***** MFSO,group1,group2
***** CMWRITE,ANSYS,cm
***** KBC,1
***** /GST,ON,ON
***** SOLVE
***** SAVE
***** CMWRITE,ANSYS,cm
***** FINISH
***** /EXIT

```

```

. . .
PROBLEM DIMENSIONALITY. . . . .3-D
DEGREES OF FREEDOM. . . . . UX  UY  UZ
ANALYSIS TYPE . . . . .TRANSIENT
  SOLUTION METHOD. . . . .FULL
OFFSET TEMPERATURE FROM ABSOLUTE ZERO . . . . 273.15
NONLINEAR GEOMETRIC EFFECTS . . . . .ON
EQUATION SOLVER OPTION. . . . .PCG
  MEMORY SAVING OPTION. . . . .ON
  TOLERANCE. . . . .1.00000E-08
PLASTIC MATERIAL PROPERTIES INCLUDED. . . . .YES
NEWTON-RAPHSON OPTION . . . . .PROGRAM CHOSEN
GLOBALLY ASSEMBLED MATRIX . . . . .SYMMETRIC

```

```

*** NOTE ***                      CP =    138.812   TIME= 10:19:27
This nonlinear analysis defaults to using the full Newton-Raphson
solution procedure. This can be modified using the NROPT command.

```

```

*** NOTE ***                      CP =    138.812   TIME= 10:19:27
The conditions for direct assembly have been met. No .emat or .erot
files will be produced.

```

...

APPENDIX D. EXAMPLES OF CONVERGENCE HISTORY

Convergence history of displacement of the leading edge midpoint (Point A) of Plate 1 is here presented. The examples were taken from cases 1 and 4.

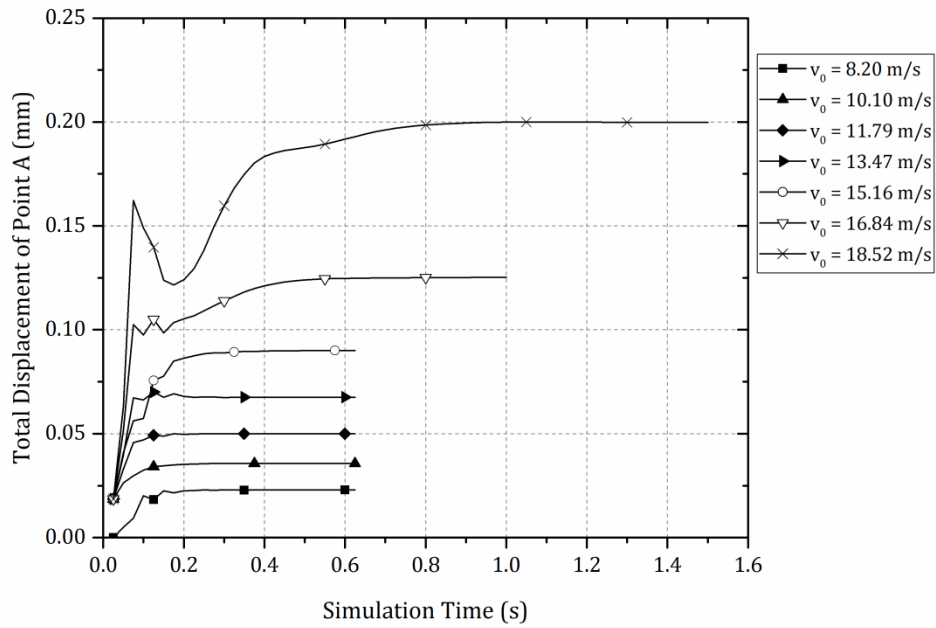


Figure D.1. Convergence history of Point A displacement for different fluid velocities in the channels in Case 1.

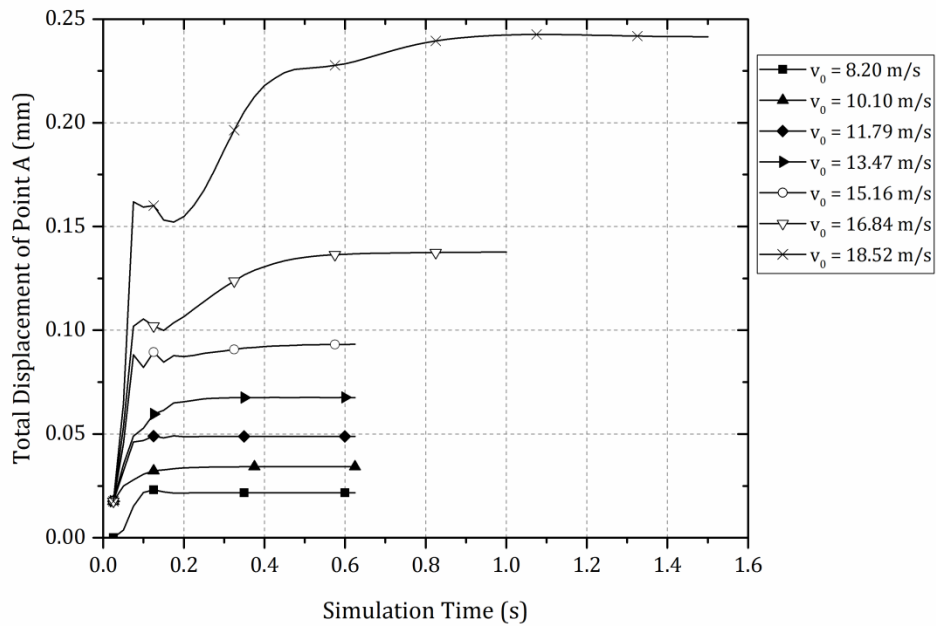


Figure D. 2. Convergence history of Point A displacement for different fluid velocities in the channels in Case 4.



INSTITUTO DE PESQUISAS ENERGÉTICAS E NUCLEARES
Diretoria de Pesquisa, Desenvolvimento e Ensino
Av. Prof. Lineu Prestes, 2242 – Cidade Universitária CEP: 05508-000
Fone/Fax(0XX11) 3133-8908
SÃO PAULO – São Paulo – Brasil
<http://www.ipen.br>

O IPEN é uma Autarquia vinculada à Secretaria de Desenvolvimento, associada à Universidade de São Paulo e gerida técnica e administrativamente pela Comissão Nacional de Energia Nuclear, órgão do Ministério da Ciência, Tecnologia e Inovação.